

Neuromorphic control of embodied central pattern generators

A bio-inspired approach to motion

Christian Fernandez Lorden



Supervisors :

Pr. Pierre Sacré

Pr. Guillaume Drion

Master's thesis completed in order to obtain the
Master of Science in Electrical engineering

University of Liege
School of Engineering and Computer Science
Academic Year 2022-2023

Neuromorphic control of embodied central pattern generators

A bio-inspired approach to motion

Christian Fernandez Lorden

Supervised by Pr. Pierre Sacré and Pr. Guillaume Drion

University of Liège - School of Engineering and Computer Science
Academic year 2022-2023

Abstract

The control of robotic locomotion poses important challenges. In particular, we are still very far from achieving robotic locomotion control with the same degree of robustness and adaptability to unexpected environmental perturbations exhibited by moving biological systems.

This master's thesis aims to create a robust and efficient controller for regulating a simple mechanical system. Biological neuron models are used to create artificial central pattern generators (CPGs) that form the core of the controller. Similar to Yu et al. [39], the inspiration of this thesis is the known electrophysiology, sensory response, and modulation of biological CPGs [28, 3, 23].

This study explores the control of a simple resonant mechanical system (a pendulum) to achieve high-amplitude periodic motion without fine-tuning the neuron parameters and with sensory feedback and weak actuation. The design follows multiple steps. It starts with the design and tuning of the controller using a single neuron. This uncovers that only the motor neurons exhibiting a robust type of bursting [10, 8] are able to robustly and easily adapt their excitable behavior to the unknown mechanical system's properties (damping, resonant frequency, mass, etc.). This is followed by the natural addition of another motor neuron to form a CPG and make the controller symmetric. This increases the achievable amplitude and improves the resilience to perturbations in the controller parameters. Then, neuromodulation is added to allow the dynamic change of the controller properties to control the amplitude of the oscillations. This leads to a trade-off between the speed of convergence to the desired amplitude and the stability of the controller. Finally, multiple controller-pendulum systems are interconnected at the controller level to achieve the desired spatiotemporal pattern between the pendulums.

The results indicate that the neuromorphic approach is well-suited for the design of robust controllers. The proposed controller demonstrates the ability to easily adapt to the mechanical system properties to achieve the amplitude goal, as well as the ability to interconnect in a network of controllers. Extensions of the model could be used to control locomotion in robotics or other domains.

Acknowledgements

I wish to express my gratitude to each and every person who helped me in some way or another to write this thesis.

First and foremost, I would like to thank my two supervisors, without whom I would not have managed to undertake this journey. Pierre Sacré, whose supervision, counsel, and insight during our meetings helped me build and structure my thesis. Guillaume Drion and his profound knowledge of systems and neurons, who helped me grasp many concepts that were foreign to me.

Similarly, I would like to express my appreciation to Alessio Franci. Despite not being my official supervisor, he attended nearly all of my meetings and took the time to guide me through the field of neuromorphic engineering. I would also like to thank him for his neuronal models, which form the basis of this thesis.

Finally, I want to thank my family and friends. Without their unwavering support, I would never have been able to find the strength to achieve this work.

Contents

1	Introduction	1
1.1	Problem Statement	2
1.2	Related literature	2
1.3	Structure and remarks	3
2	Neurons and CPGs	4
2.1	Excitability	4
2.2	Conductance-based neuron models	5
2.3	Neuronal Behavior Metrics	8
2.4	Central Pattern Generators and Rhythms	10
2.5	Embodied Intelligence and CPGs	11
3	Modeling and analysis of neuronal circuits.	12
3.1	ODEs of the Neuronal Model	12
3.2	Behavior of neuron in function of its parameters	15
3.3	Bursting neuron characteristics	18
3.3.1	Spike number modulation with g_{s-}	20
3.3.2	Inter-burst frequency modulation with g_{p+}	22
3.4	Tonic spiking type-I neuron characteristics	23
3.5	ODEs of the synaptic connections	24
3.6	Half center oscillator analysis	25
4	A neuromorphic sensorimotor loop for pendulum swing	29
4.1	The mechanical system	29
4.2	Sensory feedback types	30
4.2.1	Angle based feedback	30
4.2.2	Angle and angular velocity based feedback	31
4.2.3	Spike based feedback	32
4.3	Controller with single motor neuron	33
4.3.1	Performance of the sensorimotor loop	33
4.3.2	Robustness of the sensorimotor loop	40
4.4	Two neuron "push-pull" controller	45
4.4.1	Performance of the sensorimotor loop	45
4.4.2	Robustness of the sensorimotor loop	52

5 Neuromodulation for adaptive amplitude control	57
5.1 Design of the controller	57
5.2 Controller performance	60
5.2.1 Static	66
5.2.2 Dynamic	67
5.2.3 Static-Dynamic performance Trade-off	67
5.3 Robustness analysis	68
6 Simple interconnection of controller-pendulum systems	72
6.1 Nature of the interconnection	72
6.2 Non-neuromodulated system	73
6.3 Independently neuromodulated system	75
6.4 Globally neuromodulated system	75
7 Conclusion	80
A Signal Analysis Algorithms	86
A.1 Neuronal signal analysis	86
A.2 Oscillation analysis	86
A.3 Modulation analysis	88

Chapter 1

Introduction

In robotics, the control of locomotion still presents significant difficulties. On one hand, we are currently distant from attaining the level of robustness and adaptability to unforeseen changes in the environment that is demonstrated by living organisms. On the other hand, the mobile nature of most robots forces them to resort to batteries or other embedded energy sources to power themselves. However, an embedded energy source often means that energy becomes a valuable resource for the robot. This limits the power that can be allocated to onboard computing, leading to a trade-off between power allocated to computing and autonomy, increasing the difficulty of creating robust controllers.

To solve this energy and robustness problem, new approaches are emerging. One of them is neuromorphic engineering, which aims to extract the useful properties of biological neuronal systems to create highly efficient artificial neuronal controllers or processing units.

While not directly related to robotics, a relatively classic and old but still striking example is the game of Go between Lee Sedol and AlphaGo [31, 32, 33]. This match marked the first time a top-tier Go player was beaten by an AI. While this appears to contradict the first sentences of this paragraph, an aspect that should not be overlooked is the power consumed by both player. Miranda and Suñé [25] cite that AlphaGo needed around 1 MW of power to play Go, while Lee Sedol brain only sipped around 20 W, while also performing other tasks such as processing visual information. This shows that the current machine learning approach achieves impressive performance but, even with current improvements [19], fails to even approach the power efficiency and versatility of neuronal structures. In comparison, the human brain is an extremely energy-efficient processor. It is capable of simultaneously processing audio, visual, and other sensory feedback while making decisions based on incomplete knowledge. Neuromorphic engineering tries to reproduce the efficiency that was seen in the brain or other biological systems.

For motion, multiple researches [28, 3, 23] show that simple neuronal systems called central pattern generators (CPGs) are the basis of motion in nature. Schneider and Smarandache-Wellmann [28] shows that this system is the basis of the movement of the crayfish while Bässler and Büschges [3] proves a similar thing for the stick

insect. It is thought that these basic systems exhibit very important properties that are the reason for their success.

1.1 Problem Statement

This thesis investigates the control of a simple resonant mechanical system (a pendulum). Traditionally, the control of such a system is achieved through a PID using trajectory tracking or other continuous controllers.

This thesis aims to create and analyze an artificial neuronal controller capable of generating sustained oscillations of a simple pendulum. The generated oscillation must be regular, and the amplitude of this motion should be dynamically controlled using an external parameter. To achieve this goal, this thesis explores the concepts of excitability and CPGs to create a more robust controller.

To be clearer, the controller should fulfill the following properties.

- Be an end-to-end neuromorphic controller
- Act by generating torque at the attachment point.
- Use only the angular position and velocity as observed variables
- Maintain stable symmetric oscillations
- Regulate oscillations to achieve the desired amplitude
- Be resilient to inaccuracies in the controller parameters
- Respect the natural frequency of the system

1.2 Related literature

For this thesis, two fields of study are relevant because the thesis sits at their intersection. These are the fields of neuromorphic control and pendulum control.

Strangely enough, very little literature exists on the control of a simple pendulum. The best match is the work of Chung and Hauser [6] which is based on Isidori and Byrnes [17] and develops a controller for regulating the energy of a pendulum attached to a cart. This is similar to regulating the amplitude because a given amount of energy can be linked to a certain amplitude.

Others are more distant from the classical pendulum. Cheng et al. [5] explore to control of a pendulum with propellers attached on its side using an adaptive Kalman filtering PID. While Ali et al. [2] are interested in controlling the swing of a leg system using a H₂ full state feedback with a PID controller.

Conversely, extensive literature exists on neuromorphic control. Like Santos et al. [26] who designed a biomimetic controller for biped motion control. Or Lu et al. [21] which proposed a new CPG structure for motion control. Many articles could be cited, but suffice it to say that the field is gaining traction. No article was

found that directly solved the problem of pendulum swing, but the closest subject would probably be bipedal locomotion on which many people have done research [35, 1, 26, 9].

From this research, it seems that the problem presented in this thesis has not yet been considered. However, perhaps it was a sub-problem of some other research that was not found.

1.3 Structure and remarks

This thesis is divided into multiple chapters with distinguishing themes.

Chapter 2: Neurons and CPGs This chapter serves as an introduction to the field of neuromorphic engineering. This section explains and defines the terms specific to this domain that are used throughout the thesis.

Chapter 3: Modeling and analysis of neuronal circuits In this chapter, the models of neurons and synapses that are used to create the controller are defined. It also explores the behavior of the neuron model as a function of its parameters.

Chapter 4: A neuromorphic sensorimotor loop for pendulum swing In this chapter, the main problem of the thesis is addressed. Two models of controllers are defined and analyzed. The goal is to determine which subspace of parameters leads to a strong connection between the controller and the mechanical system.

Chapter 5: Neuromodulation for adaptive amplitude control This chapter expands the model found in the previous chapter to include a system capable of modifying the controller parameters to achieve a desired amplitude.

Chapter 6: Simple interconnection of controller-pendulum systems The last chapter briefly explores the idea of generating specific spatiotemporal patterns between pendulums by interconnecting their controllers.

Note that throughout the thesis, multiple parameters are assigned units. These units distinguish the role that the parameters play in the models. They do not represent actual physical quantities.

Also, the thesis rely on multiple metrics to make decision or compare sets of parameters. Appendix A contains the explanation of the metrics as well as the algorithms used to compute them.

Chapter 2

Neurons and CPGs

In this thesis, concepts specific to neuromorphic engineering will be used extensively. Before diving into the design and results of the proposed controllers, a clear understanding of these and other related concepts must be achieved. Otherwise, comprehension of the choices or design decisions will be difficult.

2.1 Excitability

The first step in understanding neuronal systems is the concept of excitability. In the words of Sepulchre et al. [29], “Excitability is the property of a system to exhibit all-or-none response to pulse inputs”. In other words, the system does not react to pulses until the pulse amplitude and/or length crosses a certain threshold after which the system responds completely.

In figure 2.1, an example of an excitable behavior is displayed. As can be seen, a very small difference in the pulse amplitude resulted in a very different neuronal behavior. The lower pulse resulted in the output faithfully following the input while the output of the higher one exhibited a very different behavior with oscillation and peaks far above the input. The second behavior is known as “bursting” and will be discussed later. Also, this example highlights that the “none” response does not need to be a complete silence but can be a simple linear response to the input. This is the behavior exhibited by the neuronal model of this thesis.

Most neuronal systems contain some excitable blocks such as neurons. Indeed, on a conceptual level, the all-or-none response is important for transforming continuous input into discrete events. This discretization makes a system more resilient to noise and capable of reacting only when necessary.

This kind of response is desired in our controller because effective control of the oscillation of a pendulum requires a very all-or-nothing control input. Indeed, actuation should only occur at specific times. In addition, the moment of actuation is crucial when controlling a pendulum, and actuating at a bad time can lead to very poor results. In the words of Sepulchre et al. [29], “[Excitability] is instrumental in converting sensory signals into motor actions”.

More theoretically, to create an excitable system, a localized positive feedback

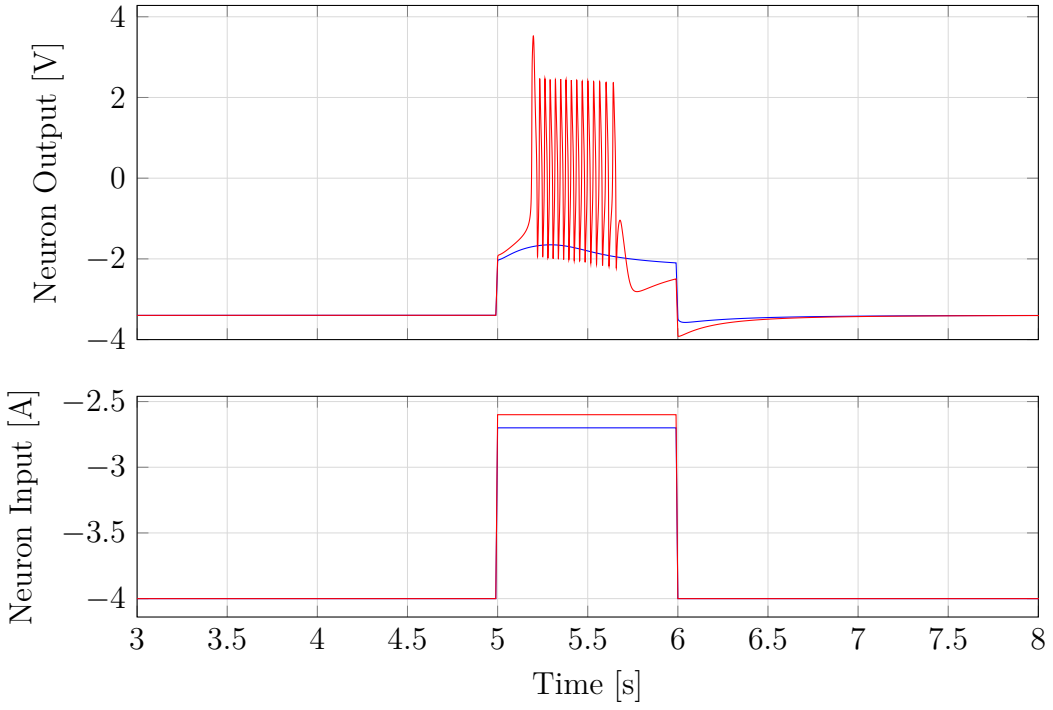


Figure 2.1: Example of an excitable behavior. Generated using neuron model of chapter 3.

loop is necessary. Indeed, the switch between two different responses after crossing a threshold requires the activation of a positive feedback near the threshold. This feedback pushes the output of the system to generate the excitable event. The locality of this positive feedback also prevents the output from growing to infinity.

2.2 Conductance-based neuron models

With excitability defined, neuronal models can be understood more clearly. Indeed, neurons are a prime example of an excitable system.

In the words of De Couck [7], “Neurons are the basic building blocks of the nervous system, which includes the brain, the spinal cord, and the peripheral nervous system. These specialized cells are the information-processing units responsible for receiving, processing, and transmitting information by electrical and chemical signaling.”.

In other words, neurons are cells that can receive input from the external world, send messages to one another, and send motor commands to muscles. The relationship between the input received and the commands or messages sent is the processing performed by the neuron. Because neurons can be relatively large compared with the scale of electrical or chemical signaling, it is evident that their behavior may be different in different parts of the cell. However, a common way to observe a neuron is to measure and model its activity in only one location. This leads to the neuron

being seen as a block with a single input and output and a certain hidden state.

As shown by Hodgkin et al. [14], the state of a neuron at its axon membrane can be described by the flow of ionic currents. The magnitude of these currents is determined by the potential across the interior and exterior of the cell, which opens or closes channels at different speeds depending on the channel type. In turn, these currents flowing into or out of the cell influence the potential across the interior and exterior of the cell.

This model is illustrated on figure 2.2, where ionic currents flow through channels in the neuron membrane. Some of these channels activate and deactivate based on the membrane potential. Other are influenced by other factors such as the activity of other neurons or changes in biochemistry.

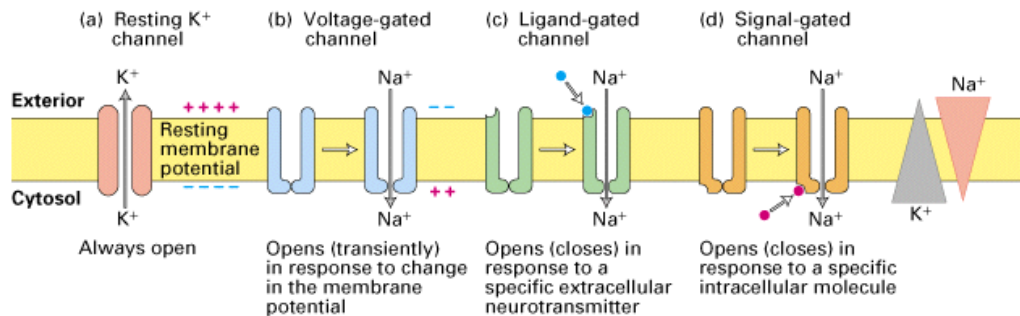


Figure 2.2: Simplified diagram of a biological neuron membrane. (Diagram taken from Lodish et al. [20])

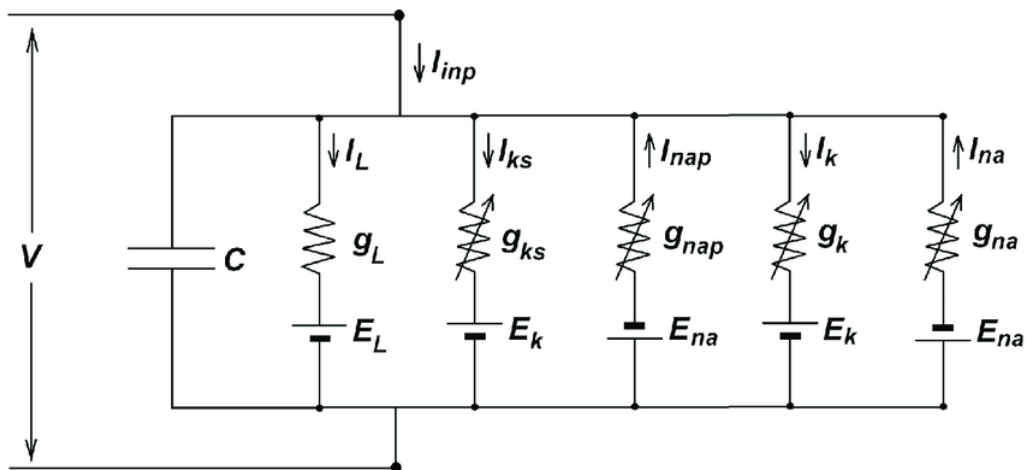


Figure 2.3: Simplified circuit of the neuron model. (Circuit taken from Vazifehkhah Ghaffari et al. [36])

This language of currents and potentials seems to designate classical circuit theory as the most useful tool to model the behavior of a neuron. Hodgkin and Huxley [15] were the first to formulate a model of neuronal behavior using a parallel network of dynamic conductances. These conductances change based on the membrane

voltage of the neuron at different rates, mimicking the opening and closing of the channels. A good representation of this model is seen in figure 2.3. On this diagram, it can be seen that some ionic current discharge the capacity that represents the membrane while others charge it. Those charging currents effectively act as positive feedback loops. As seen in the previous section, these are necessary for the excitable behavior of a neuron.

Using circuit theory, this model can be written more formally using ordinary differential equation. Equations (2.1) to (2.5) are a very general representation of this model. In this representation the i subscripts denote the different ionic currents that can be found in figure 2.3.

$$C \frac{\partial V}{\partial t} = I_{\text{inp}} - g_L (V - E_L) - \sum_i I_i \quad (2.1)$$

$$I_i(t, V) = g_i(t, V)(V - E_i) \quad (2.2)$$

$$g_i(t, V) = \bar{g}_i m_i(t, V)^{p_i} h_i(t, V)^{q_i} \quad (2.3)$$

$$\frac{\partial m_i(t, V)}{\partial t} = \frac{m_{i\infty}(V) - m_i(t, V)}{\tau_{mi}(V)} \quad (2.4)$$

$$\frac{\partial h_i(t, V)}{\partial t} = \frac{h_{i\infty}(V) - h_i(t, V)}{\tau_{hi}(V)} \quad (2.5)$$

The m_∞ , h_∞ , τ_m and τ_h functions are saturation functions. The saturation of the ∞ terms show that the ionic current feedbacks are localized in a certain range of membrane voltage.

The m_∞ are increasing positive saturation functions, while the h_∞ are decreasing positive saturation functions.

In this case, what is important for feedback is the local feedback, which is characterized by the differential conductance. Studying the global feedback would be useless since a conductance is a passive element and it always acts as a global negative feedback. The range of the saturation of m_∞ , h_∞ and the power assigned to them will determine where the term acts as positive feedback and when it acts as a negative feedback.

This model is very general, and when parameters are chosen properly, it can generate a whole range of neuronal behaviors seen in biological neurons. However, it is very hard to tune, and small changes in parameters can completely change the behavior of the system, whereas large changes may leave the output looking identical. This is important in a biological system to improve robustness to variations while providing efficient switching between modes. But, in this thesis, all these advantages are of very little use. Therefore, a simplified model will be used to make tuning easier.

In this thesis, only spiking and bursting, the two most common behaviors, will be used; therefore, only these behaviors will be studied. These two behaviors can be seen in figure 2.4. A spike is a sudden, short, and steep increase in the membrane voltage followed by a sharp decrease and return to a resting voltage. A burst is

the apparition of a packet of spikes. A spike is a prime example of the importance of fast local positive feedback. Indeed, a spike is formed by the positive feedback pushing the voltage of the neuron upward before deactivating and letting the slower negative feedback drag down the voltage before the positive feedback reactivating in the other way to push the voltage downward.

Classically, both behaviors can be classified as tonic or phasic. A tonic response means that the response persists as long as the stimulus is maintained. This is observed in figure 2.4 where the spike and burst repeat. A phasic response means that the response is localized at the apparition of the stimulus and will fade as the stimulus is maintained. This is observed in figure 2.1, the burst does not continue after the initial response. Often, for a set of parameters, as the input current increases, a neuron will first have a phasic response before starting to become tonic.

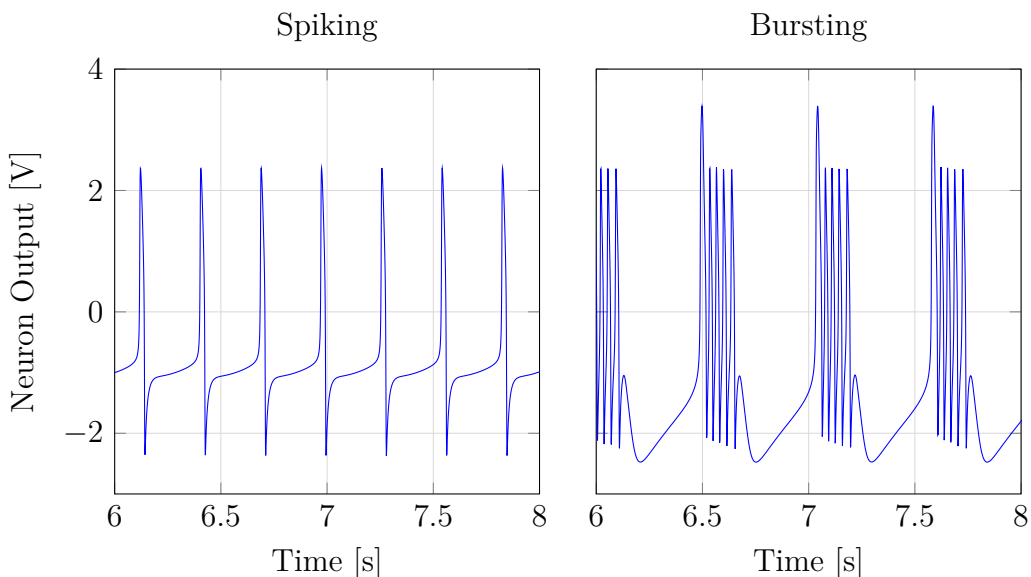


Figure 2.4: Example of spiking and bursting behaviors. Generated using the neuron model of chapter 3.

2.3 Neuronal Behavior Metrics

The previous section introduced the spiking and bursting behaviors. These behaviors are highly complex and therefore, to be able to compare different bursting or spiking realizations, multiple specific metrics must be defined. Here, only the metrics to evaluate the tonic spiking and the tonic bursting will be discussed. It is easy to derive similar metrics for the phasic case.

To compare different bursting realizations, it is important to consider the shape of a burst and the link between two bursts. Figure 2.5 represents values that can be directly inferred from the trace of a tonic bursting neuron that are enough to characterize a specific bursting trace. These values can be defined as

Burst length Average time of a burst event.

Rest length Average time of inactivity between two burst events.

Burst period Average time between the start of two burst events.

Spike period Inside a burst, the average time between the start of two spike events.

Number of spikes Average number of spikes inside a burst event.

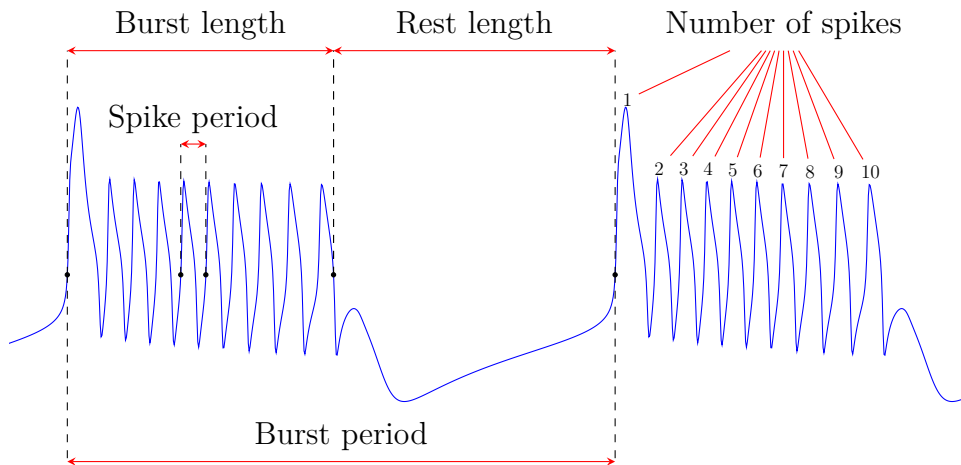


Figure 2.5: Illustration of the different metrics used to describe bursting. Generated using the neuron model of chapter 3.

Aside from the number of spikes, these raw metrics are not the most telling. Instead, the following set of metrics derived from the aforementioned values is used.

Inter-burst frequency $\frac{1}{\text{Burst period}}$, the frequency at which burst events occur.

Intra-burst frequency $\frac{1}{\text{Spike period}}$, frequency at which spikes occur inside a burst event.

Duty cycle $\frac{\text{Burst length}}{\text{Burst period}}$, the portion of a period during which the neuron is inside a burst event.

Number of spikes Average number of spikes inside a burst event.

Even though the inter-burst and intra-burst frequencies are just the inverses of direct metrics, the realm of frequencies is often better suited for comparison between realizations.

On the other hand, spiking is simpler and does not require as many metrics. The only direct metric is measuring the **Spike period**. It is sufficient to compute the **Spiking frequency**, which is the most useful metric for describing spiking behavior. For the same reason as the bursting transformation to the frequency realm is better for comparison.

2.4 Central Pattern Generators and Rhythms

From Straub [34], “A central pattern generator (CPG) is an assembly of neurons that can produce a rhythmic activity pattern without [] sensory feedback information”. This construction thus uses multiple neurons to generate a certain rhythm.

It is widely accepted that central pattern generators (CPGs) are frequently found in biological motion systems. Marder and Bucher [24], Grillner [11] highlight that CPGs are abundant in animals for motion control. The natural periodic oscillations of CPGs makes them easier to pair them with systems that are already periodic.

Therefore, the concept of central pattern generators (CPGs) is very useful for developing controllers. Indeed, CPGs being closely linked to rhythmic movements pair well with the naturally rhythmic movement of the oscillation of a pendulum.

Here, to keep it simple, the connections between neurons inside a CPG result in the activity of the presynaptic neuron generating currents in the postsynaptic neuron. These connections can have two types, inhibitory and excitatory. Inhibitory connection results in a negative current being injected, whereas excitatory connection results in a positive current.

As an example, one of the most simple and well-studied CPGs is the half-center oscillator [30]. This specific circuit is composed of two neurons that inhibit each other. The system along with a simulation can be seen in 2.6. The dents in the activity of one neuron appearing when the other is active highlight that currents flow from one neuron to the other only if the presynaptic neuron is activated.

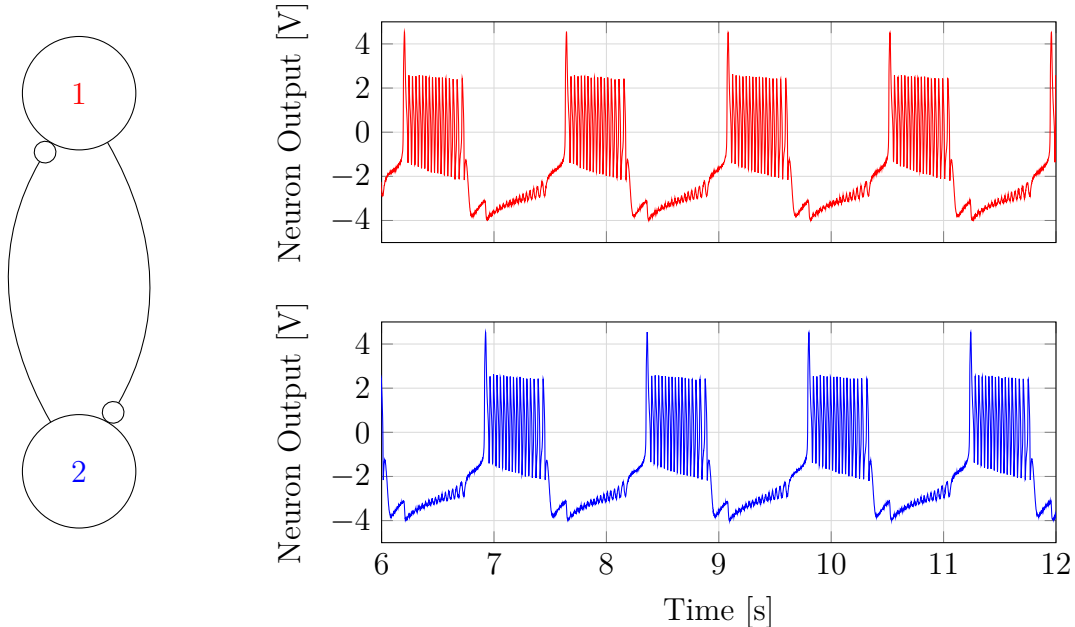


Figure 2.6: Example of an half center oscillator. Traces were generated using neuron model of chapter 3.

The generation of rhythmic patterns is clear when looking at the traces of the

activation of both neurons. Indeed, the activation of neurons 1 and 2 always follow each other.

The interesting aspect of CPGs is that the network may be able to generate a rhythm while an individual neuron may be silent. This shows that the structure of the CPG is instrumental and is the key factor in the qualitative rhythm produced. Very different models of neurons will still generate the same rhythm when used in a fixed CPG structure.

2.5 Embodied Intelligence and CPGs

From Cangelosi et al. [4] “Embodied intelligence is the computational approach to the design and understanding of intelligent behavior in embodied and situated agents through the consideration of the strict coupling between the agent and its environment (situatedness), mediated by the constraints of the agent’s own body, perceptual and motor system, and brain (embodiment).”.

This concept describes the goal of this thesis. Indeed, the model developed later is a prime example of embodied intelligence. The controller processes the direct sensory input to generate coherent control signals for the motor. Using neuromodulation, the strength of the push is changed according to the desired amplitude. This amounts to intelligent behavior generated by components directly interacting with sensors and motors.

More broadly, the concept of embodied intelligence is closely related to CPGs. Indeed, CPGs are circuits that are rhythmic without sensory feedback, but using sensory feedback to tune the frequency of the CPG to the external is thought to be the inner working of most biological motion controllers [13, 12, 16]. This coupling is precisely a low-level embodied intelligence.

To simplify embodied intelligence, it can be seen as the coupling of sensing computing and actuating. The agent in embodied learning has sensors, computing, and actuation in the same body.

Chapter 3

Modeling and analysis of neuronal circuits.

Building upon the concepts defined previously, this chapter aims to show and study the different possible behaviors that the neuronal model can exhibit. In more detail, a quick explanation of the model is provided, followed by a general analysis of the active regions of the model. Then, a more detailed analysis of specific parameter values is conducted for some bursting and some spiking. The discussion will also include the definition of synapses and their use to create a half-center oscillator.

3.1 ODEs of the Neuronal Model

The backbone of the model used is based on a model developed by Pr. A. Franci. A diagram representing this model can be seen in figure 3.1. The diagram shows that the model is composed of four different internal variables. The membrane potential V , the fast voltage v_f , the slow voltage v_s and the ultra-slow voltage v_u . The system also has a single input I_{app} the applied current. This block diagram can be easily translated into ODEs because it is composed only of functions and first-order low-pass filters. Equations (3.1) to (3.8) are a more formal description of the neuron model.

$$\tau_o \frac{\partial V}{\partial t} = V_0 + I_{\text{app}} - i_{f-} - i_{s+} - i_{s-} - i_{u+} - V \quad (3.1)$$

$$i_{f-} = g_{f-} (\tanh(v_f - d_{f-}) - \tanh(V_0 - d_{f-})) \quad (3.2)$$

$$i_{s+} = g_{s+} (\tanh(v_s - d_{s+}) - \tanh(V_0 - d_{s+})) \quad (3.3)$$

$$i_{s-} = g_{s-} (\tanh(v_s - d_{s-}) - \tanh(V_0 - d_{s-})) \quad (3.4)$$

$$i_{u+} = g_{u+} (\tanh(v_u - d_{u+}) - \tanh(V_0 - d_{u+})) \quad (3.5)$$

$$\tau_f \frac{\partial v_f}{\partial t} = V - v_f \quad (3.6)$$

$$\tau_s \frac{\partial v_s}{\partial t} = V - v_s \quad (3.7)$$

$$\tau_u \frac{\partial v_u}{\partial t} = V - v_u \quad (3.8)$$

with $g_{f-}, g_{s-} < 0$, $g_{s+}, g_{u+} > 0$ and $d_{f-}, d_{s+}, d_{s-}, d_{u+} \in \mathbb{R}$.

Here i_{f-} is the fast positive feedback to the neuron, i_{s+} and i_{s-} are the slow negative and positive feedback and i_{u+} is the ultra-slow negative feedback. + represents negative feedback and - represents positive feedback because, in electrical notation, the current is oriented to discharge the neuron. Therefore, an increase in the current tends to decrease the membrane voltage, whereas a decrease in the current tends to increase the membrane voltage.

i_{s+} and i_{s-} could be written as a single current because they are on the same timescale v_s . However, since they play a different role in the behavior of the neuron and to maintain the symmetry between the currents, they are written separately.

This model displays local positive feedback both with i_{f-} and i_{s-} . As seen in the

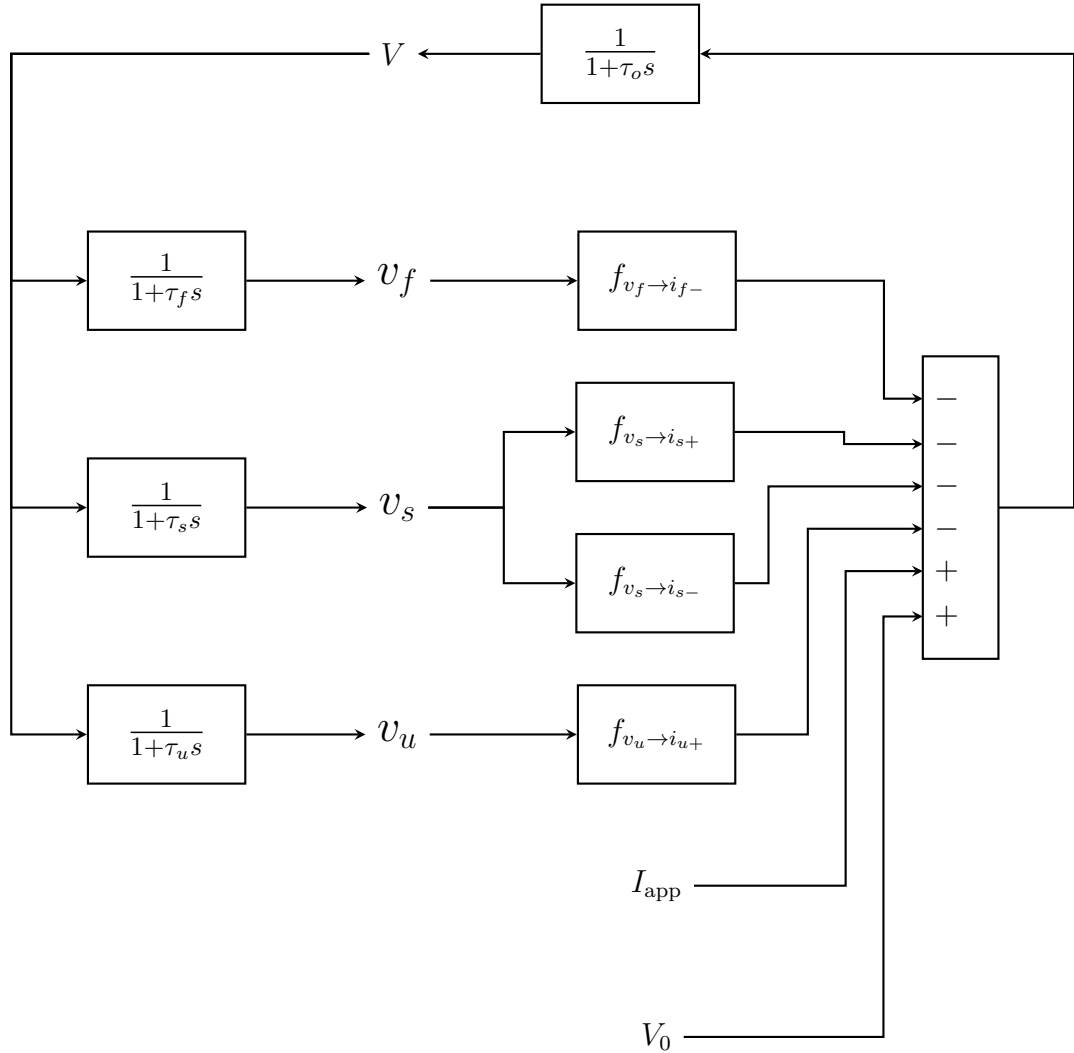


Figure 3.1: Diagram of the Neuron Model. The output of the neuron is V and the input is I_{app} .

previous chapter, this positive feedback is necessary for excitable behaviors. More precisely, this model follows the findings of Franci et al. [10]. They stated that tunable and robust neuronal behavior must include slow positive feedback. Slow in this context means in a timescale between the fast positive feedback that creates the spike and the ultra-slow feedback that slowly brings the neuron back to a resting voltage. In this model, the i_{s-} currents fill this role. Designing a system with this slow feedback should make its bursting more resilient to changes in other parameters.

This model is a simplification of a conductance-based model with four currents on three fixed timescales and variable conductances replaced by a low-pass filter followed by explicit voltage-to-current relationships. The model being written in the language of currents and voltages is reminiscent of the origin of this model.

For this thesis, some parameters of the model will remain fixed at the following values. Exploring these parameters does not lead to interesting results that are not reachable without tuning them.

V_0	-0.85 V	τ_o	0.0004 s
d_{f-}	0.0 V	τ_f	0.001 s
d_{s+}	0.5 V	τ_s	0.04 s
d_{s-}	-0.5 V	τ_u	0.8 s
d_{u+}	-0.5 V		

To ensure the stability of the models, it is always a good idea to apply some noise to simulate real-world conditions. In the case of the neuron, the best way to add noise easily is to add it to the input current. In this way, noise affects the entire neuron. This is also a good way to represent real use because in an integrated chip, most of the noise should come from the outside world.

To better understand the inner workings of the neuron, figure 3.2 shows a representation of the currents and voltages of the model during a simulation.

The low-pass filter effect is very clear when looking at the different voltages. v_f is nearly indistinguishable from V due to the very high cutoff frequency of the filter. v_s , on the other hand, follows the general pattern of the bursting but has a cutoff frequency low enough to filter the spikes inside the burst. v_u filters the bursting and follows a smooth sawtooth pattern, rising during the burst and falling down during the inactivity between bursts.

The saturation of the current is very visible when looking at the flat regions of some currents, especially i_{s+} , which is nearly a flat line between the bursts. This indicates the inactivation of the slow negative feedback because changes in voltages do not result in changes in i_{s+} . Furthermore, the "launching" effect of the slow positive feedback is visible. i_{s-} , is the first current to activate with a slow slope before the burst and seems to start the burst by activating i_{f-} . Then, the increase in voltage seems to launch i_{f-} which starts the first spike of the burst. This indicates a i_{f-}, i_{s+} pair that is more closely linked with the spikes inside the burst and a i_{s-}, i_{u+} pair that is more associated with the burst itself.

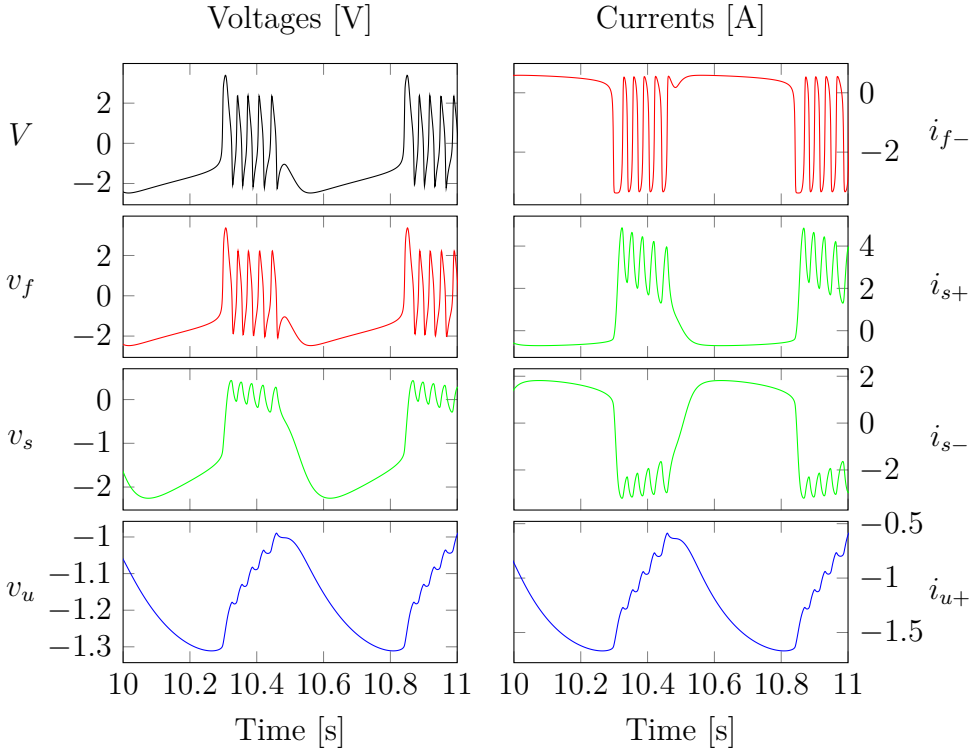


Figure 3.2: Currents and voltages inside the neuron model. Currents share the color of their generating voltages.

3.2 Behavior of neuron in function of its parameters

Before designing a controller, the behavior of the neuron under different parameters must be studied to determine the best parameters for the controller. For this analysis, only an exploration of the parameters g_{s-} , g_{u-} and I_{app} is done since they are the parameters most relevant to bursting. g_{f-} and g_{s+} are fixed to $g_{f-} = -2 \text{ S}$ and $g_{f-} = 6 \text{ S}$ since those parameters gave good bursting behavior.

Firstly, figure 3.3 displays an overview of the different regions where the neuron is active. More precisely, it distinguishes between different activation types. Here 3 different activation types are considered. Spiking and bursting, which were defined in the previous chapter, and plateau, which is short for plateau bursting. Plateau bursting is a degenerate form of bursting that sees the apparition of a plateau voltage between the first spike and the rest of the spikes of the burst. In extreme cases, plateau bursting stops containing any spike other than the first spike, and the behavior becomes analogous to periodic pulses.

For this thesis purpose, the bursting region is the most interesting because it allows tunability by playing with intra- and inter-burst characteristics.

In this configuration, the bursting region seems to advance with an increase in the applied current until $I_{app} = 0 \text{ A}$ then in recedes, seemingly pushed by the spiking

region. The border between normal bursting and plateau behavior seems to follow a line that does not really depend on I_{app} . This border indicates that the plateau behavior is mostly dependent on the value of g_{s-} and nearly independent of the value of g_{u+} . The shape of this boundary is probably controlled by g_{f-} and/or g_{s+} . The parameters at the center of the chart are capable of sustaining bursting for various applied currents. Indeed, a neuron with $g_{s-} \approx -4$ S and $g_{u+} \approx 5$ S seems to be in a very stable bursting zone for the controller. It can sustain bursting from $I_{app} = -1.8$ A to $I_{app} = 2$ A and seems far enough from plateau bursting to never show unwanted behaviors.

Now that the good region has been highlighted, a closer look at the inter-burst frequency will be useful to categorize bursting. Indeed, it is better to have neurons attuned to the frequency of the pendulum to obtain good results. However, let us keep in mind that for large swings, the frequency of the pendulum depends on the amplitude of the swing; therefore, a perfect match for changing amplitudes will probably not be found. In figure 3.4, it can be seen that the inter-burst frequency is mostly determined by the value of the conductances and not the applied current. Changing the applied current mostly only changes the zone where bursting occurs. The applied current still has an effect on the frequency, higher currents leads to a slightly higher frequency. However, changing the values g_{s-} and g_{u+} has a far greater effect on the inter-burst frequency. Note that the inter-burst frequency is also computed on the plateau behavior. The continuity between both behaviors shows that the plateau behavior is actually just degenerate bursting.

However, by performing a finer analysis on I_{app} , another zone of bursting can be discovered. In figure 3.5, this zone is highlighted. This bursting occurs in a zone with nearly no slow positive feedback. Yet, Franci et al. [10] indicated that the slow positive feedback is integral to a reliable bursting. The lack of robustness of this bursting can already be inferred from the extent to which the zone of bursting shifts when subject to a small change in the input current. In addition, the boundary of bursting seems more diffuse and the inter-burst frequency inside the zone does not seem to not follow a continuous pattern. All these signs point toward this zone being an unreliable bursting behavior. Still, a more detailed analysis to show the fragility of this bursting is necessary to eliminate it completely as a possibility.

Figure 3.6 shows a comparison of the simulations of the stable bursting found earlier and the "fragile" bursting discovered here with and without noise. This reveals that "fragile" bursting is totally destabilized by the addition of a small noise. The regular two-spike pattern that appears without noise ceases to exist, and the number of spikes per burst and the inter-burst frequency seem to be very random. The spikes probably correlate with the noise inside the neuron. On the other hand, the "stable" burst seems unaffected by the noise. The only visual indicator of the added noise is the shape of the voltage during the resting period, where small oscillations caused by the noise can be observed. The number of spikes and the inter-burst frequency of stable bursting remain unchanged by noise. This proves that the region of "stable" bursting is a far better burst than the region of "fragile" bursting since the first is resistant to noise and the latter is not.

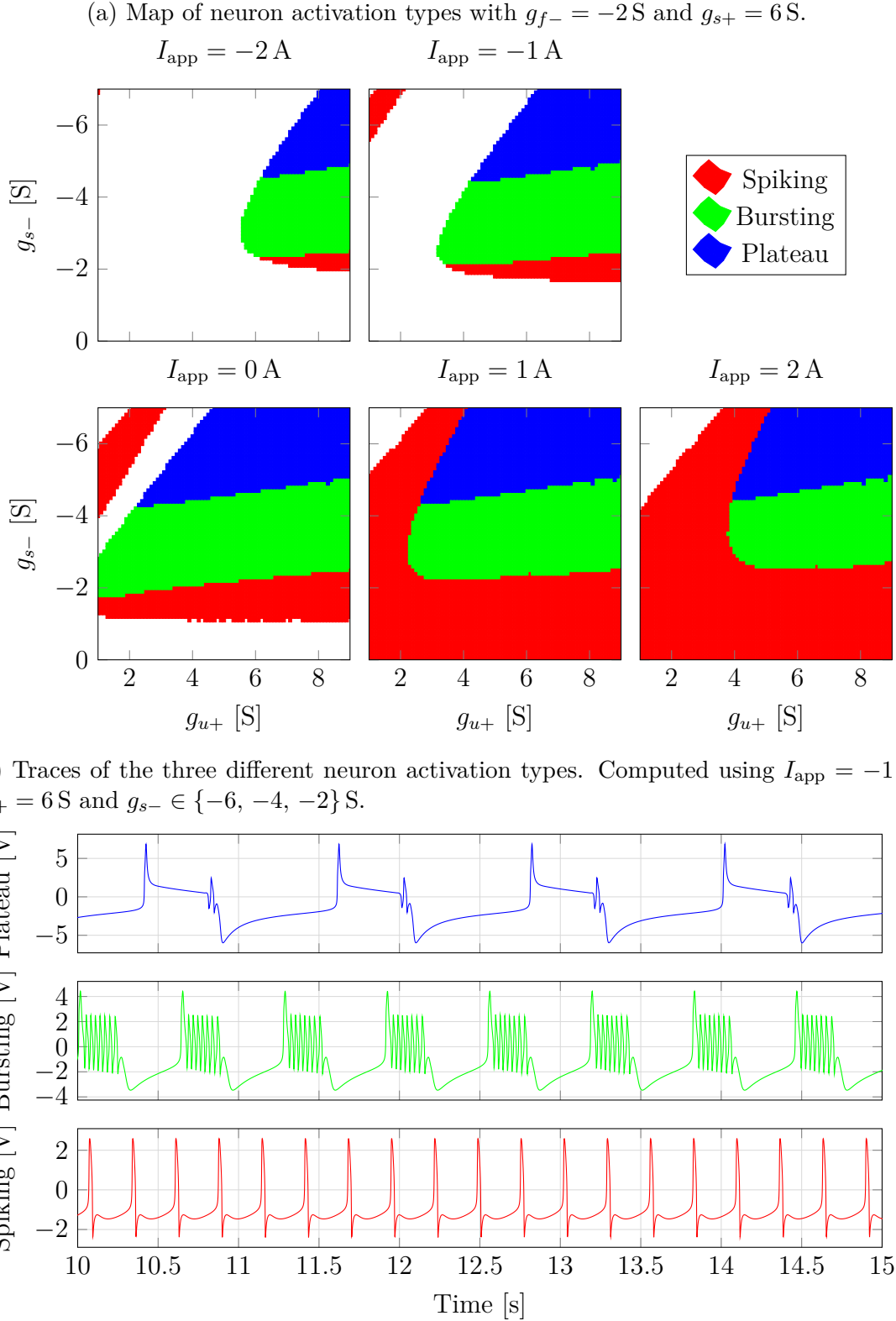


Figure 3.3: Different types of neuron activation. The plateau region corresponds to the bursting region, where a voltage plateau exists between the first spike and the rest of the spikes.

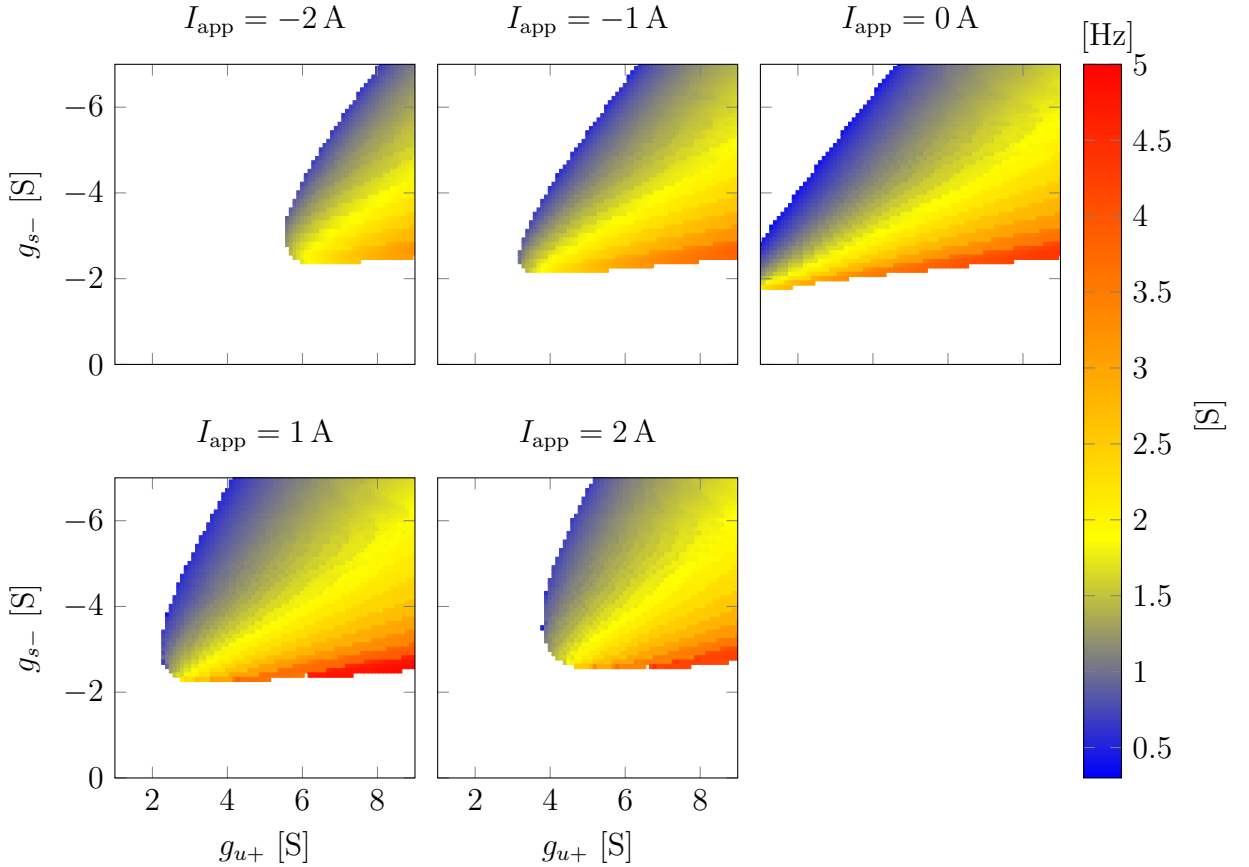


Figure 3.4: Map of neuron bursting frequency with $g_{f-} = -2 \text{ S}$ and $g_{s+} = 6 \text{ S}$.

This behavior is probably due to "stable" bursts being launched by i_{s-} and the "fragile" burst being launched by i_{f-} since i_{s-} is nearly zero. The filtering of noise is far better for v_s than for v_f because of the lower cut-off frequency of v_s . Thus, the variable v_f that launch the "fragile" burst is greatly affected by the noise, leading to the noise being able to launch a burst. On the other hand, what launches the "stable" bursting nearly unaffected by the noise, leading to almost no change in the behavior of the neuron.

3.3 Bursting neuron characteristics

In this section the changes in bursting behavior through the modification of certain parameters are studied. Some analyses or graphs will only be performed with one set of parameters for bursting. Nonetheless, the conclusions drawn will hold for most of the normal bursting region and especially for the bursting region of interest in this thesis.

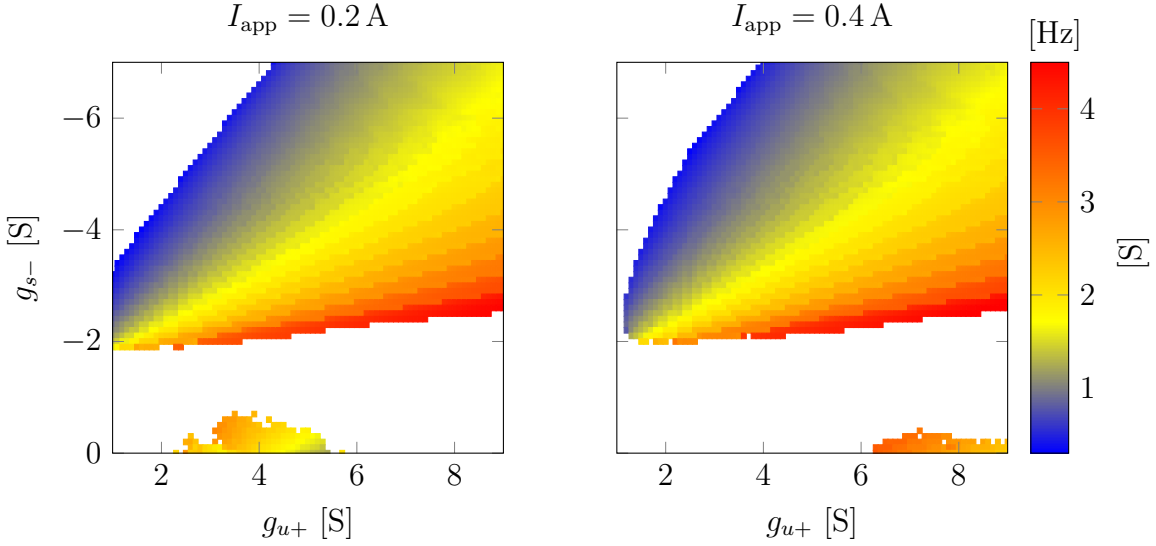


Figure 3.5: Map of neuron bursting frequency with $g_{f-} = -2 \text{ S}$ and $g_{s+} = 6 \text{ S}$. Zoom on specific I_{app} with apparitions of another bursting region.

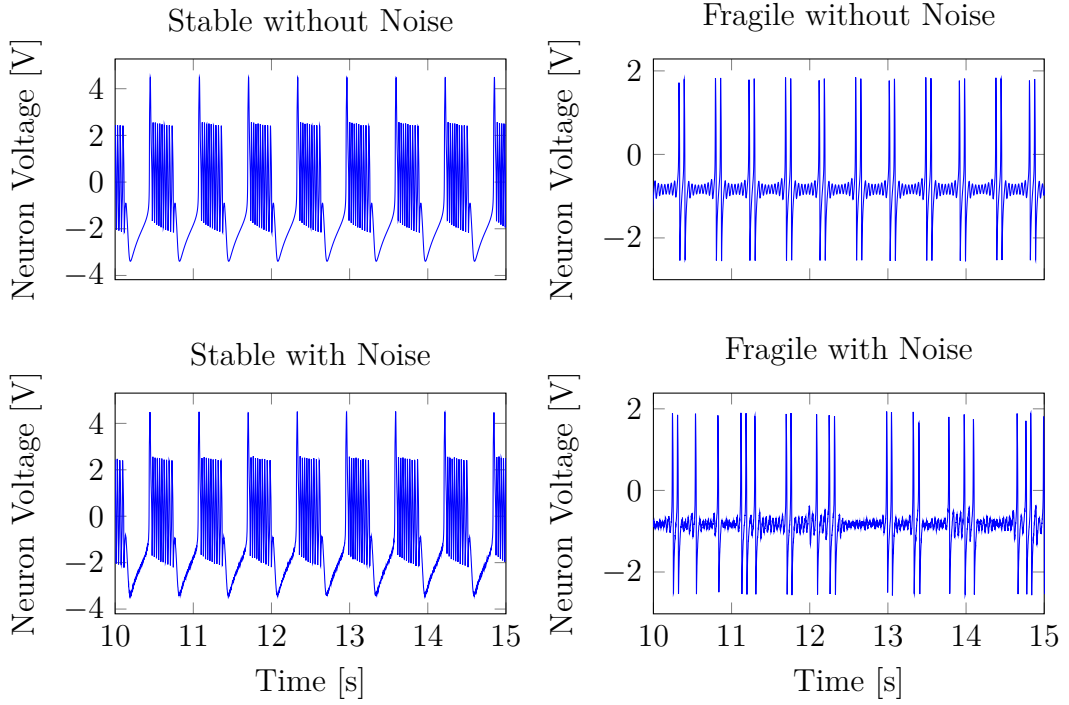


Figure 3.6: Comparison of both times of bursting at $I_{\text{app}} = 0.2 \text{ A}$. The stable model used $g_{s-} = -4 \text{ S}$ and $g_{u+} = 5 \text{ S}$ and fragile model used $g_{s-} = -0.2 \text{ S}$ and $g_{u+} = 4 \text{ S}$. The applied noise had a spectral power density of $n_{I_{\text{app}}} = 3 \times 10^{-7} \text{ V}^2 \text{ Hz}^{-1}$.

3.3.1 Spike number modulation with g_{s-}

A simple way to change the amount of power transmitted by a burst is to change the number of spikes in the burst. Indeed, if g_{f-} and g_{s+} are fixed, the spike uptime will remain nearly the same regardless of the values of g_{s-} and g_{u+} . This leads to the number of spikes being the most important metric for characterizing the power transmitted by the spikes. Indeed, the integral of the positive value of the membrane voltage can be seen as very strongly correlated with the number of spikes in the burst.

Both g_{s-} and g_{u+} could be used to modulate the number of spikes.

But, figure 3.4 shows that the value of g_{u+} is more important to guarantee the existence of bursting at a specific I_{app} . Indeed, the range of g_{s-} where bursting exists is almost constant at $[-4; -2]$ S for all I_{app} . On the other hand, the range of where bursting exists for g_{u+} varies from $[6; 9]$ S to $[1; 9]$ S as I_{app} goes from -2 A to 0 A. Thus, g_{s-} will be used as the parameter to modulate the number of spikes because it is less likely to annihilate bursting.

The effect of this modulation can be seen in figure 3.7 where the value of g_{s-} is varied while counting the number of spikes. The graph shows a clear link between the number of spikes in the burst and the value of g_{s-} parameter. The number of spikes decreased "linearly" as the amplitude of the feedback decreased. Since the number of spikes must obviously be an integer, "linearly" means that the width of a region with a certain number of spikes is nearly constant. Thus, the shape can be regarded as rounding the value of a linear function. This trend holds until the number of spikes hits one and the neuron starts spiking instead of bursting.

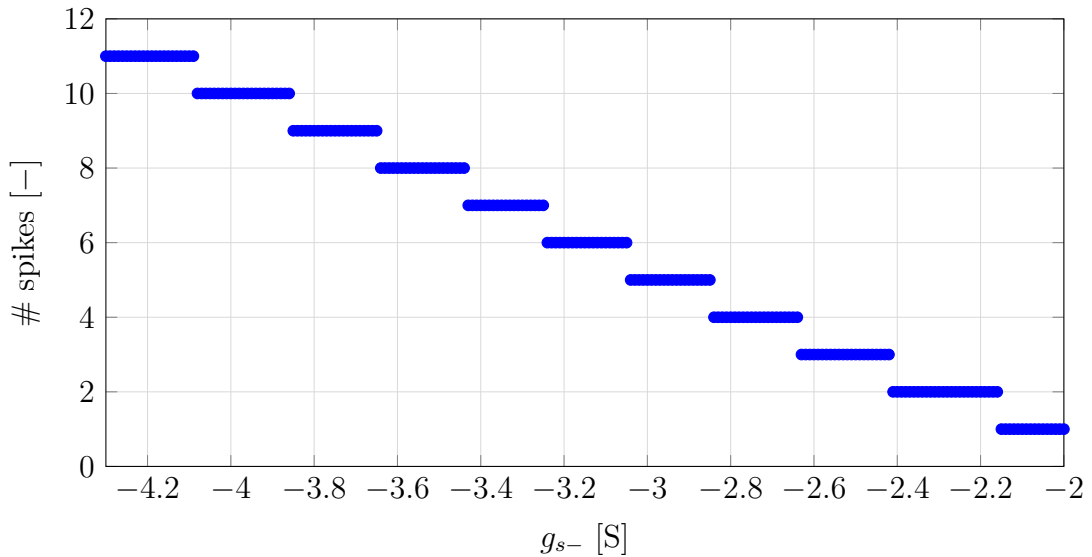


Figure 3.7: Curve of the number of spikes as a function of the g_{s-} parameter. With $I_{app} = -1$ A, $g_{f-} = -2$ S, $g_{s+} = 6$ S and $g_{u+} = 5$ S.

The explanation of why the number of spikes is strongly linked to the power transmitted was slightly ad hoc. To confirm that this metric correlates well with

the amount of power transmitted by the burst, a comparison with other metrics is necessary. The metrics proposed for comparison with the number of spikes are the duty cycle of the burst and the mean positive value of the bursting. The mean positive value is a value defined as

$$\text{mean positive value} = \frac{1}{T} \int_{t_0}^{t_0+T} \max(0, V(t)) dt \quad (3.9)$$

The mean positive value is interesting because, in this thesis, when the membrane voltage is negative, the neuron is always considered inactive. Of these two metrics, the mean positive value is obviously the most reliable; however, it is also interesting to see how well the duty cycle correlates with this value.

Figure 3.8 displays the plot of these two metrics as a function of g_{s-} values like in figure 3.7. Analyzing this figure reveals that the number of spikes is indeed correlated with the power transmitted because the mean positive value is nearly constant with the number of spikes.

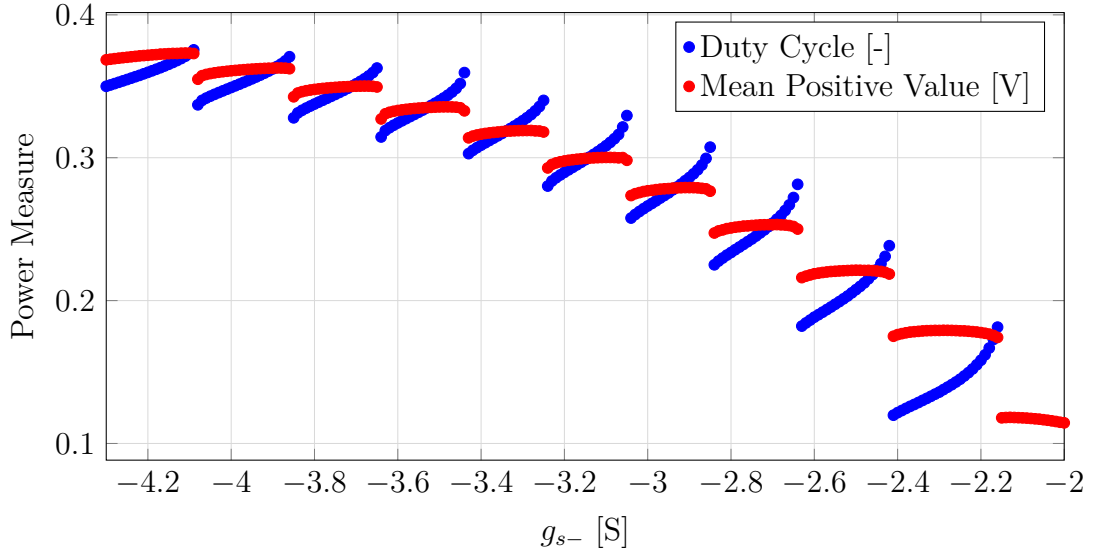


Figure 3.8: Curve of the burst power as a function of the g_{s-} parameter. With $I_{app} = -1\text{ A}$, $g_{f-} = -2\text{ S}$, $g_{s+} = 6\text{ S}$ and $g_{u+} = 5\text{ S}$.

In addition, these figures show that the duty cycle is a poorer indicator of power because it can have the same value at two very different values of g_{s-} . Moreover, at two g_{s-} where the duty cycles are equal, the number of spikes and the mean positive value are very different, indicating poor performance of the metric. In fact, the duty cycle follows a sawtooth pattern in which it grows with g_{s-} but then has a large discontinuity when the number of spikes changes. It appears that increasing g_{s-} (thus reducing its effect) decreases the intra-burst frequency until a spike drops and the frequency returns to a higher level. The observation of the intra-burst frequency is linked to the fact that a lower frequency leads to a larger burst, which means a larger duty cycle.

To confirm this explanation, figure 3.9 plots the intra-burst frequency as a function of g_{s-} and shows that this is indeed the case. The intra-burst frequency has a strange relationship with g_{s-} as increasing g_{s-} can locally increase the intra-burst frequency but globally decrease it.

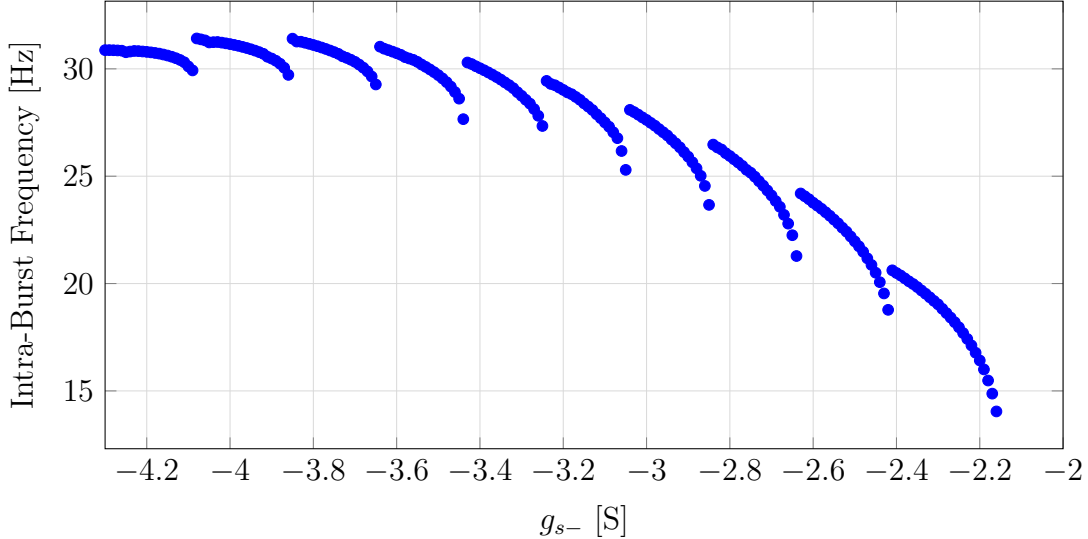


Figure 3.9: Curve of the intra-burst frequency as a function of the g_{s-} parameter. With $I_{app} = -1 \text{ A}$, $g_{f-} = -2 \text{ S}$, $g_{s+} = 6 \text{ S}$ and $g_{u+} = 5 \text{ S}$.

This entire analysis was performed because changing the power transmitted by the burst is integral to the control of the pendulum. This power is linked to the torque applied to the pendulum, and controlling this torque is necessary to control the oscillation amplitude. Having a good understanding of the modulation of g_{s-} is thus crucial to the creation of a robust controller.

3.3.2 Inter-burst frequency modulation with g_{p+}

To obtain a reliable control, it is necessary for the natural frequency of the neuron to be close to that of the pendulum. Otherwise a good coupling between both systems will not be possible.

Since g_{s-} will be modulated to change the power of a burst, g_{u+} must be used for the modulation of the inter-burst frequency. g_{s-} cannot be used because it will not be fixed in the final controller, rendering any analysis worthless.

Figure 3.10 shows the influence of the parameter and the applied current on the inter-burst frequency. Interestingly, the limit between bursting and silence seems to follow a linear relationship between I_{app} and g_{u+} in this model. This is probably an artifact of the specific values of other parameters and is not a general behavior of this neuronal model. The inter-burst frequency seems to be mostly dependent on g_{u+} when far away from the bursting boundary. When approaching the boundary, the frequency quickly decreases compared with that further inside the boundary. Therefore, in that region, the applied current starts to have a larger impact on the

frequency. A higher g_{u+} leads to a higher oscillation frequency but also to an earlier activation of bursting. A link can be made with figure 3.3 where the higher the value of g_{u+} the longer the neuron stays in the bursting region.

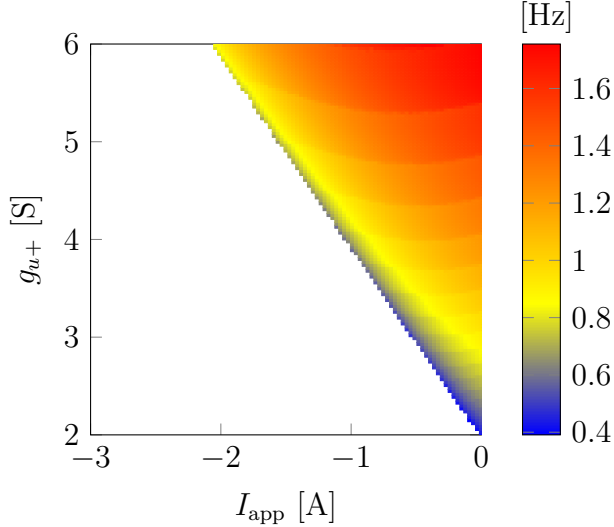


Figure 3.10: Map of the inter-burst frequency as a function of the g_{u+} parameter. With $g_{f-} = -2 \text{ S}$, $g_{s+} = 6 \text{ S}$ and $g_{s-} = -4 \text{ S}$.

This analysis does not have the same goal as the previous one because no neuromodulation of g_{u+} is done in this thesis. Rather, it allows us to better understand later why some parameter values will lead to better control of the pendulum. It was also used to slightly guide the design of the controller by restricting the parameter space for the bursting neurons

3.4 Tonic spiking type-I neuron characteristics

For sensory feedback, a tonic type-I spiking neuron will be useful because it will be able to transform continuous signals into discrete events. A neuron of that type can sustain spiking because it is tonic and has a spiking frequency that is closely correlated with the input because it is type-I. These are the definitions of both terms. This type of neuron is useful for sensory inputs because it is event based but keeps a trace of the strength of the input through the spiking frequency.

The following neuron will deviate from the standard values of g_{f-} and g_{s+} defined previously. These values were chosen for bursting, and here spiking is of interest. A detailed exploration of the parameter space was not performed either because only a single set of parameters is needed. Indeed, modulation is not necessary for the sensory neurons in this thesis.

Now, in figure 3.11, the firing frequency of the neuron is plotted in function of the input current. This figure clearly shows that for low values of applied current the spiking frequency is very strongly related with the input current. For higher

currents the frequency saturates and even decreases before the spiking disappears. But, this behavior happens at very high input current and the neuron frequency is very close to a linear function of the input for $I_{\text{app}} \in [0; 1] \text{ A}$. In normal use the neuron will never be subject to current high enough to make it exit the region of linearity. Thus, the poor performances at high input current are not problematic.

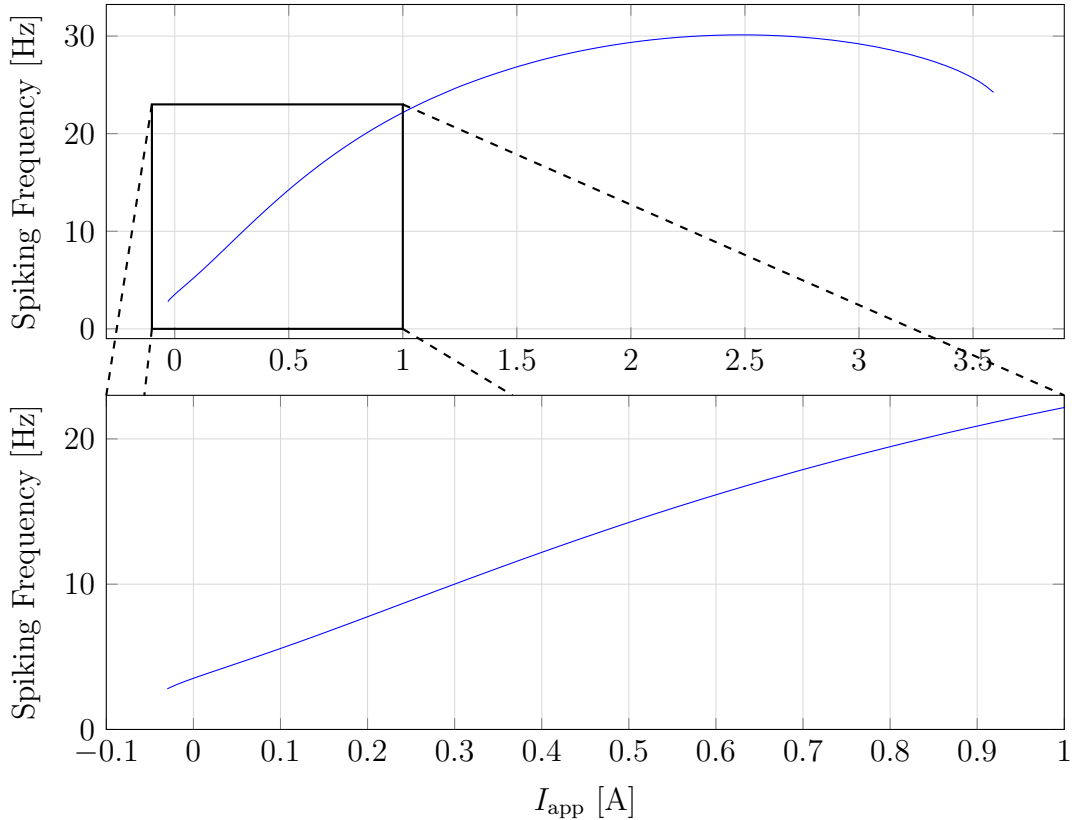


Figure 3.11: F-I curve of a type I neuron. With $g_{f-} = -2 \text{ S}$, $g_{s+} = 4 \text{ S}$, $g_{s-} = -1 \text{ S}$ and $g_{u+} = 1 \text{ S}$. The curve starts and ends at the beginning and end of spiking.

The correlation of the applied current with the spiking frequency is necessary to obtain a good representation of the input at the output of the neuron. Indeed, the neuron is supposed to convert the amplitude of the input into a frequency.

3.5 ODEs of the synaptic connections

After studying a single neuron, networks of neurons must be considered to generate more complex spatiotemporal patterns. Biologically, a classical way in which two neurons are connected is through a synapse. A synapse is a connection between two neurons that allows the membrane voltage of the presynaptic neuron to generate a current in the postsynaptic neuron. Figure 3.12 show the diagram of the synapse model that will be used in this thesis.

Similar to the neuron model, the synapse model comprises a low-pass filter followed by a nonlinear voltage-to-current function. The synapse takes the voltage of a neuron as input and produces a current that can be fed as input to another neuron. It is similar to the feedback system inside the neuron model with the difference that the current generated is not drained from the membrane potential of the presynaptic neuron but fed to the postsynaptic neuron. The difference thus lies in the receiver and the sign of the current.

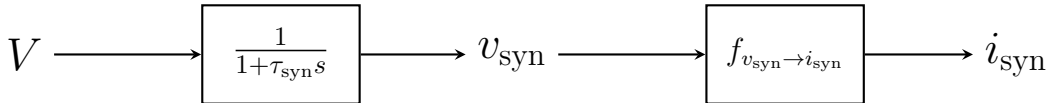


Figure 3.12: Diagram of the synapses model. The output of the synapse is I_{out} and the input is V_{in} .

More formally, this model can be written as a simple ODE.

$$\tau_{\text{syn}} \frac{\partial v_{\text{syn}}}{\partial t} = V - v_{\text{syn}} \quad (3.10)$$

$$i_{\text{out}} = g_{\text{syn}} \sigma(4(v_{\text{syn}} - d_{\text{syn}})) \quad (3.11)$$

with $g_{\text{syn}}, d_{\text{syn}} \in \mathbb{R}$ and $\sigma()$ the sigmoid function.

The factor 4 inside the sigmoid increases its slope to obtain a faster transition and makes the slope at d_{syn} equal to 1, similar to the tanh function inside the neuron.

When the input neuron is inactive, its voltage is negative; thus, the sigmoid function is nearly zero and no current is sent to the post-synaptic neuron. When the neuron is active, the sigmoid is non-zero and may even saturate to 1 and a current is sent to the post-synaptic neuron. The sign of g_{syn} will decide if the synapse is excitatory or inhibitory. A negative conductance creates an inhibitory connection that drains current, and a positive conductance creates an excitatory connection that injects current.

For this thesis, some parameters of the synapses will be fixed because changing them is not necessary to achieve the various objectives.

$$d_{\text{syn}} \quad 0.0 \text{ V} \quad | \quad \tau_{\text{syn}} \quad 0.04 \text{ s}$$

3.6 Half center oscillator analysis

Formed by the interconnection of two neurons linked by two inhibitory synapses, the half-center oscillator (HCO) is a central component of the controller. A representation of an HCO was already presented in chapter 2 by figure 2.6. A more detailed representation using specific parameters can be seen in figure 3.13.

Being the assembly of two bursting neurons, the most interesting thing to study and control in the HCO is its frequency. This frequency can be evaluated by the inter-burst frequency of one of its neurons because this frequency is the frequency of one cycle, and an HCO is defined as the alternating activation of two neurons.

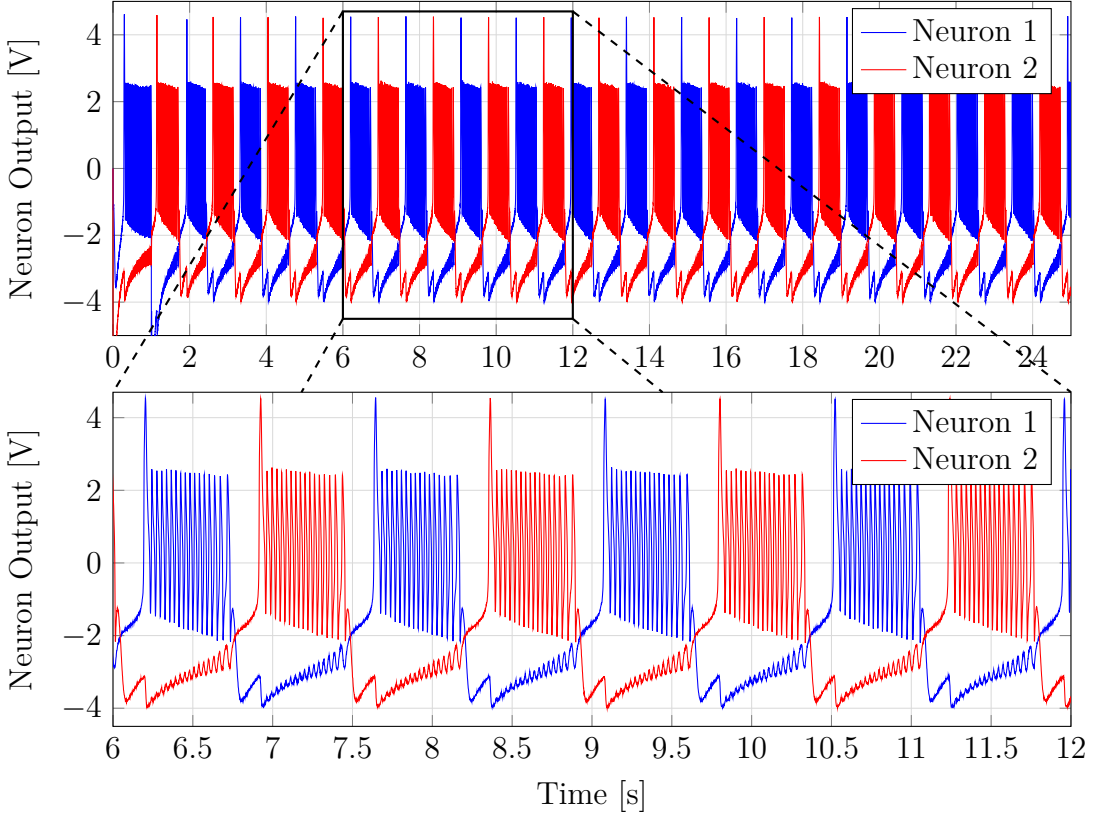


Figure 3.13: Plot of the neuronal output of a CPG. With $g_{f-} = -2 \text{ S}$, $g_{s+} = 6 \text{ S}$, $g_{s-} = -4 \text{ S}$, $g_{u+} = 3.7 \text{ S}$, $I_{\text{app}} = -1 \text{ A}$, $g_{\text{syn}} = -1 \text{ S}$.

Figure 3.14 depicts this frequency as a function of I_{app} and g_{u+} for a selection of g_{syn} . These maps are similar to figure 3.10 where the inter-burst frequency was studied for a single neuron over the same parameters. Low values of g_{syn} lead to behaviors very similar to those of uncoupled neurons, whereas higher values lead to lower frequencies. Similarity is expected since $g_{\text{syn}} = 0$ results in two uncoupled neurons. The strength of the connection has a large impact on the behavior of the system. The frequency is probably lowered by the larger values because a higher current lowers the membrane voltage of the neuron and the neurons take more time to correct this lower voltage.

A nice thing to note is that by comparing the HCO with the uncoupled case, it appears that the zone of bursting becomes larger as the strength of the connection increases. This leads to the apparition of zones where bursting emerges from the network of neurons as the neurons alone are silent. To further demonstrate this, figure 3.15 represents only the zones where bursting is caused by the network and not the intrinsic properties of the neurons. The higher the connection between the neurons is the larger the zone of bursting is.

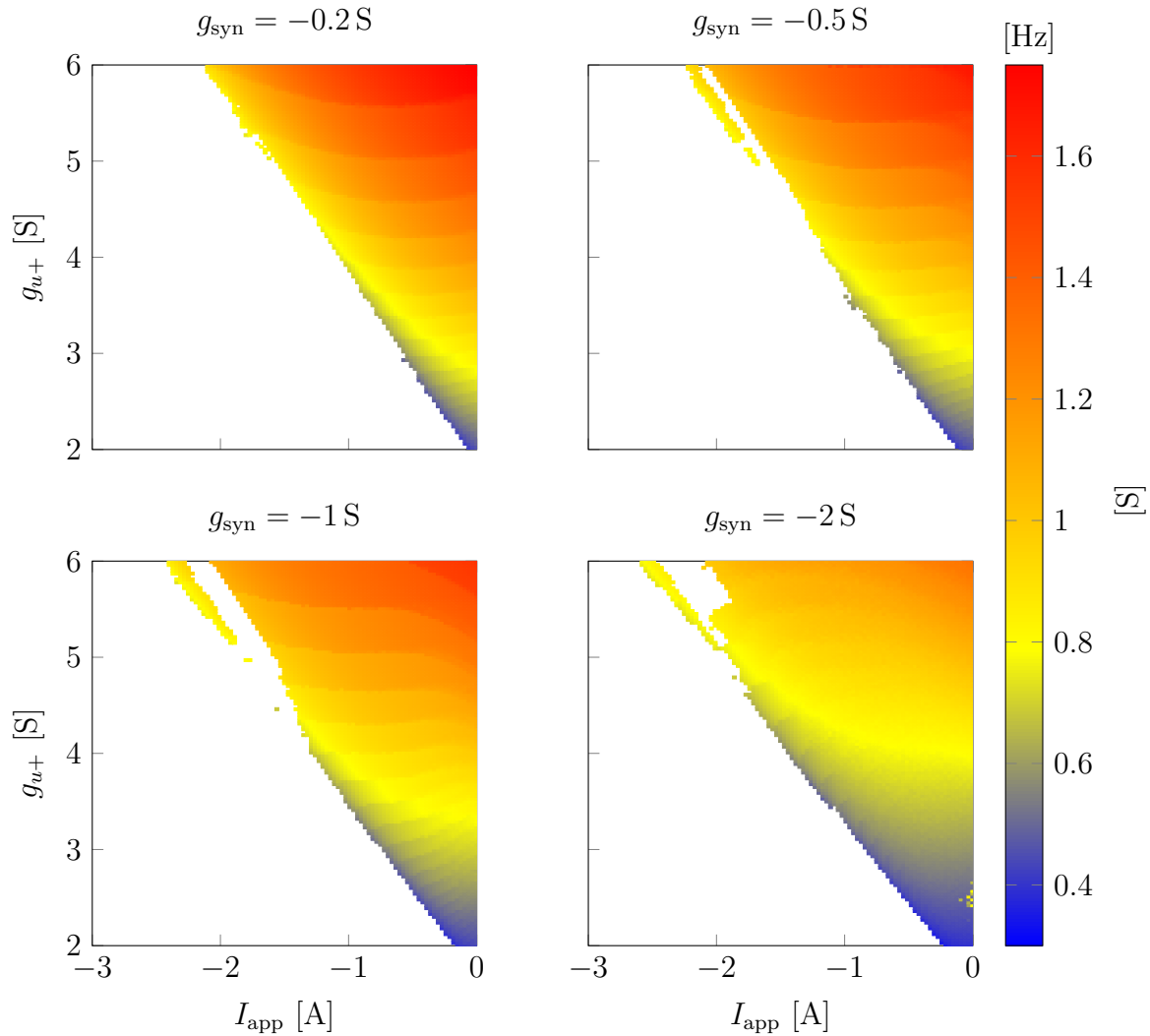


Figure 3.14: Activation of the cpg network as a function of ultraslow negative feedback and applied current. With $g_{f-} = -2 \text{ S}$, $g_{s+} = 6 \text{ S}$, $g_{s-} = -4 \text{ S}$.

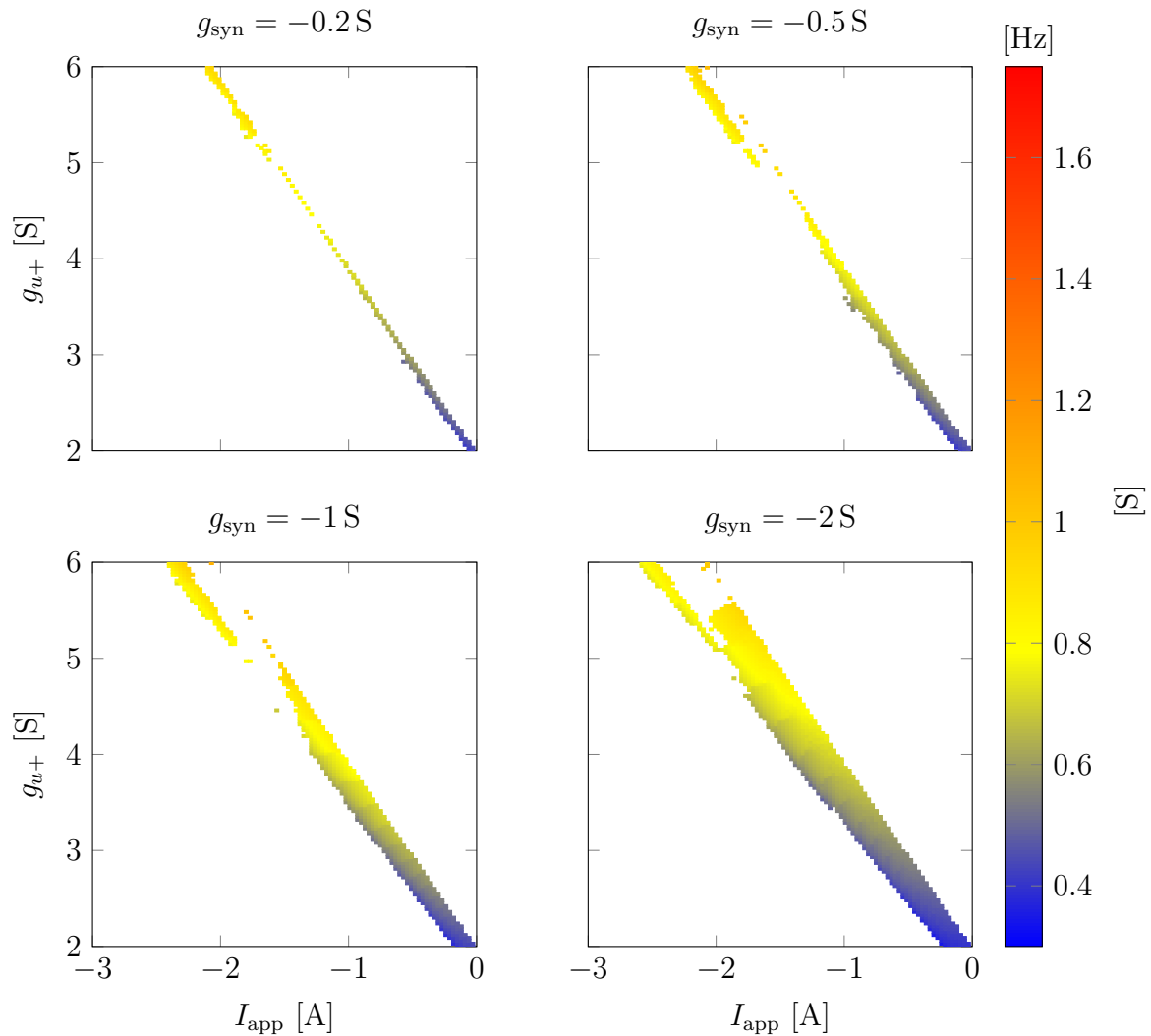


Figure 3.15: Activation of the cpg network as a function of ultraslow negative feedback and applied current. Only the region where the bursting arises from the network is shown. With $g_{f-} = -2 \text{ S}$, $g_{s+} = 6 \text{ S}$, $g_{s-} = -4 \text{ S}$.

Chapter 4

A neuromorphic sensorimotor loop for pendulum swing

The previous chapter explored the different behaviors exhibited by the neuron model. This chapter focuses on the control of a cylindrical pendulum with a neuromorphic controller built using artificial neurons. The primary goal is to find and extract a control scheme that is intrinsically linked to the mechanical system. To reach this goal, the different useful behaviors of the neuron model will be paired with multiple feedback models. The models will be evaluated on the basis of their performance and robustness.

4.1 The mechanical system

Before diving into controller design, understanding the mechanical system is important. Figure 4.1 shows a graphical representation of the system. This diagram shows that there is only a single control input to this system, the applied torque τ . The system also provides two meaningful state outputs, the angle θ with the vertical line and the angular velocity $\dot{\theta}$. Finally, the dynamics of the pendulum are influenced by five parameters: radius r of the cylinder, height h of the cylinder, density ρ of the cylinder, damping coefficient B_f , which generates the friction torque τ_f at the rotation point, and gravity \mathbf{g} .

In the figure, the gray arrow shows and defines the down direction, which is the reference of the angle θ . It can be used to separate the rotation plane into two halves. The half with negative $\sin(\theta)$ and the half with positive $\sin(\theta)$.

For simplicity, the parameters of the pendulum are kept constant. The values used for all simulations are as follows.

$$\begin{array}{ll} r & 0.05 \text{ m} \\ h & 0.5 \text{ m} \\ \rho & 1000 \text{ kg m}^{-3} \end{array} \left| \begin{array}{l} B_f \quad 0.01 \text{ N m s}^{\circ -1} = 0.57 \text{ N m s rad}^{-1} \\ \mathbf{g} \qquad \qquad \qquad 9.81 \text{ m s}^{-2} \end{array} \right.$$

The value of friction τ_f can be computed from the following equation.

$$\tau_f = \dot{\theta} B_f \tag{4.1}$$

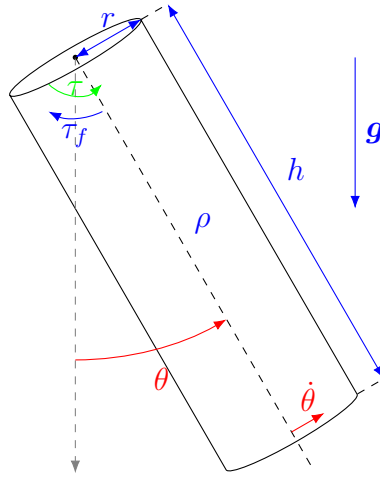


Figure 4.1: Diagram of the pendulum system. The parameters of the pendulum are shown in blue, the outputs that are fed to the controller are shown in red, and the actuation of the controller is shown in green.

It is thus dependent on the angular velocity of the pendulum $\dot{\theta}$.

4.2 Sensory feedback types

The feedback sent to the bursting neuron is at the heart of the stability of the neuronal system. Bad feedback can only lead to bad performances. Thus, three different feedback mechanisms are proposed. This ranges from the most simplistic feedback that relies only on the angle of the pendulum to complex spiking neuron-based feedback. The goal of proposing multiple feedback is to find a middle ground between feedback complexity and performance.

4.2.1 Angle based feedback

The first feedback described in figure 4.2 is the most simplistic. The direct angle feedback sends to the bursting neuron the sinus of the angle. When in the lower half of the rotational range, this value becomes increasingly negative as the pendulum angle θ decreases and vice versa when increasing.

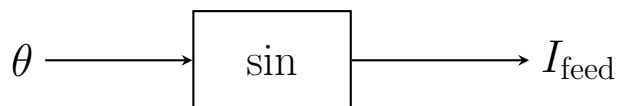


Figure 4.2: Diagram of the direct angle feedback.

$$I_{\text{feed}} = K_{\text{feed}} \alpha_{\text{dir}} \sin(\theta) \quad (4.2)$$

with $\alpha_{\text{dir}} \in \{-1, 1\}$ and $K_{\text{feed}} > 0$.

α_{dir} is a parameter relative to the part of the half plane where the feedback should be active, 1 signifies an activation in the half where $\sin(\theta) > 0$ and -1 the other half. K_{feed} is the output gain of the feedback.

4.2.2 Angle and angular velocity based feedback

This more complicated feedback described in figure 4.3 aims to send a positive value to the controller only when it is close to the optimal control timing, i.e., when the angular velocity $\dot{\theta}$ is close to 0. In addition, the feedback should only send a pulse when the pendulum is in the correct half of the rotation plane.

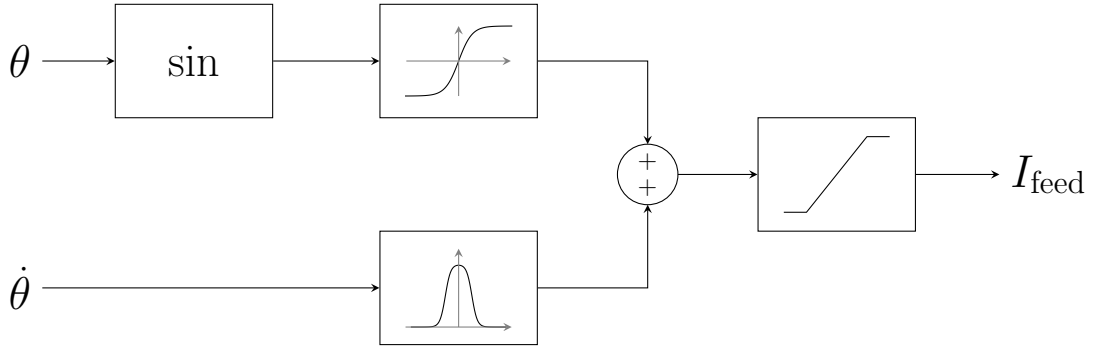


Figure 4.3: Diagram of the mixed angle and speed feedback.

$$I_\theta = \frac{\alpha_{\text{dir}} \tanh(g_\theta (\sin(\theta) - d_{\text{off}})) + 1}{2} - 1 \quad (4.3)$$

$$I_{\dot{\theta}} = \frac{\tanh(g_{\dot{\theta}} (\dot{\theta} + d_{\text{bump}})) - \tanh(g_{\dot{\theta}} (\dot{\theta} - d_{\text{bump}}))}{2} \quad (4.4)$$

$$I_{\text{feed}} = K_{\text{feed}} \min(\max(0, I_\theta + I_{\dot{\theta}}), 1) \quad (4.5)$$

with $\alpha_{\text{dir}} \in \{-1, 1\}$, $g_\theta, g_{\dot{\theta}}, d_{\text{bump}}, K_{\text{feed}} > 0$ and $d_{\text{off}} \in \leftarrow$.

α_{dir} is a parameter relative to the part of the half plane where the feedback should be active, 1 signifies an activation in the half where $\sin(\theta) > 0$ and -1 the other half. g_θ and $g_{\dot{\theta}}$ are parameters that define the sharpness of the transition of their respective tanh. d_{off} is a term that offsets I_θ to create an activation when $\theta = 0$. Since $\theta = 0$ is the resting state of the system, adding the offset avoids the system being blocked in that position. d_{bump} defines the width of the bump around $\dot{\theta} = 0$. K_{feed} is the output gain of the feedback.

For all simulations, the feedback will use the following parameter values.

g_θ	15 A rad^{-1}	$g_{\dot{\theta}}$	5 A s rad^{-1}
d_{off}	0.05 rad	d_{bump}	0.5 rad s^{-1}

4.2.3 Spike based feedback

The last feedback defined in figure 4.4 reuses principles from the previous feedback but seeks complete neuronal control using a spiking neuron coupled with a synapse to activate the controller. This approach has the advantage that the width of the pulse sent to the controller remains nearly constant and not largely influenced by the maximum rotational speed. It also guarantees the event-based nature of the feedback.

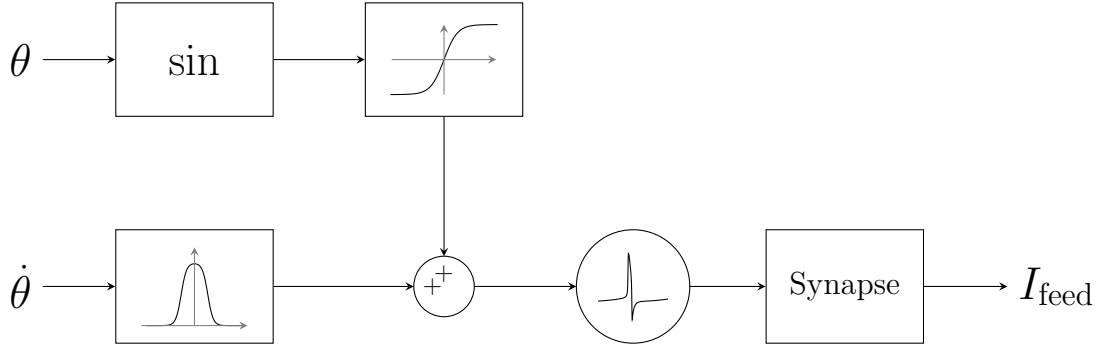


Figure 4.4: Diagram of the spike feedback.

$$I_\theta = \frac{\alpha_{\text{dir}} \tanh(g_\theta (\sin(\theta) - d_{\text{off}})) + 1}{2} - 1 \quad (4.6)$$

$$I_{\dot{\theta}} = \frac{\tanh(g_{\dot{\theta}} (\dot{\theta} + d_{\text{bump}})) - \tanh(g_{\dot{\theta}} (\dot{\theta} - d_{\text{bump}}))}{2} - 1 \quad (4.7)$$

$$V_{\text{neur}} = \text{spiking_neuron}(I_\theta + I_{\dot{\theta}}) \quad (4.8)$$

$$I_{\text{feed}} = \text{synapse}(V_{\text{neur}}) \quad (4.9)$$

with $\alpha_{\text{dir}} \in \{-1, 1\}$, $g_\theta, g_{\dot{\theta}}, d_{\text{bump}}, K_{\text{feed}} > 0$, $d_{\text{off}} \in \wedge$, spiking_neuron is an instance of the neuron defined in figure 3.1 and synapse is an instance of the synapse defined in figure 3.12.

α_{dir} is a parameter relative to the part of the half plane where the feedback should be active, 1 signifies an activation in the half where $\sin(\theta) > 0$ and -1 the other half. g_θ and $g_{\dot{\theta}}$ are parameters that define the sharpness of the transition of their respective tanh. d_{off} is a term that offsets I_θ to create an activation when $\theta = 0$. Since $\theta = 0$ is the resting state of the system, adding the offset avoids the system being blocked in that position. d_{bump} defines the width of the bump around $\dot{\theta} = 0$. The parameter g_{syn} will be used as the output gain of the feedback instead of a K_{feed} parameter.

For all simulations, the feedback will use the following parameter values.

g_θ	15 A rad^{-1}	$g_{\dot{\theta}}$	5 A s rad^{-1}	d_{off}	0.05 rad
d_{bump}	0.5 rad s^{-1}	g_{f-}	-2 S	g_{u+}	1 S
g_{s+}	4 S	I_{app}	0.1 A	g_{s-}	-1 S
d_{syn}	-0.5 V				

While this controller should generate output similar to the simple mixed feedback, the advantage of using a neuron spike is the stability of the pulse width. Indeed, the width of the mixed feedback is determined in part by the acceleration of the pendulum, which is linked to the angle at which the speed crosses 0. The spike of a neuron does not suffer from this problem. In addition, a spiking neuron has a refractory period that prevents it from recreating a pulse too quickly. However, because of the inertia of the pendulum, this problem should not be encountered by the mixed feedback most of the time.

4.3 Controller with single motor neuron

The first use of the various feedback defined previously is to simply connect the feedback to a bursting neuron that will only be able to apply torque in a single direction. Figure 4.5 represents the proposed controller architecture. The output of the bursting neuron is passed through a saturation function that limits the output of the neuron between 0 and 1. This leads the neuron to generate torque only during bursting. The gain at the saturation output defines the strength of the actuation. This controller architecture is naturally imbalanced since the actuation is not symmetric and thus the damping inside the pendulum will always lead to a lower amplitude on the side of actuation.

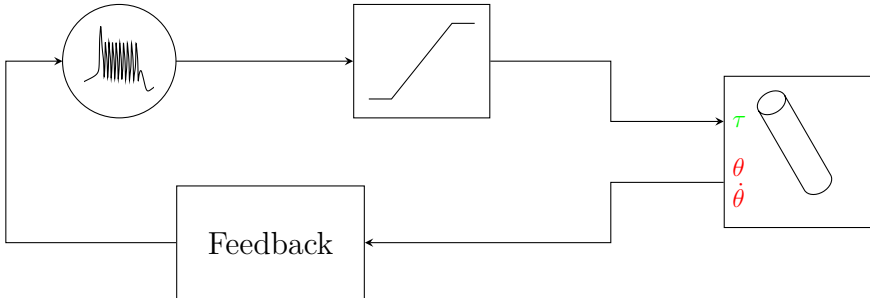


Figure 4.5: Diagram of the sensorimotor loop for the single-neuron controller. The saturation block limits are 0 V to 1 V. The saturation block also contains an internal output gain τ_{\max} .

Figure 4.6 displays a realization of this controller. This clearly shows the imbalanced nature of the controller when the angle oscillates from -0.5 rad to 1 rad. It is interesting to observe the regularity of the oscillation, which indicates that the controller is well attuned to the mechanical system.

4.3.1 Performance of the sensorimotor loop

The performance of a controller can be accessed by its ability to generate stable oscillations of large amplitude. To study the oscillation resulting from the proposed controller, an analysis of the parameters of the bursting neuron g_{s-} , g_{u+} and I_{app} and the parameters of the strength of the feedback K_{feed} or g_{syn} on the oscillation

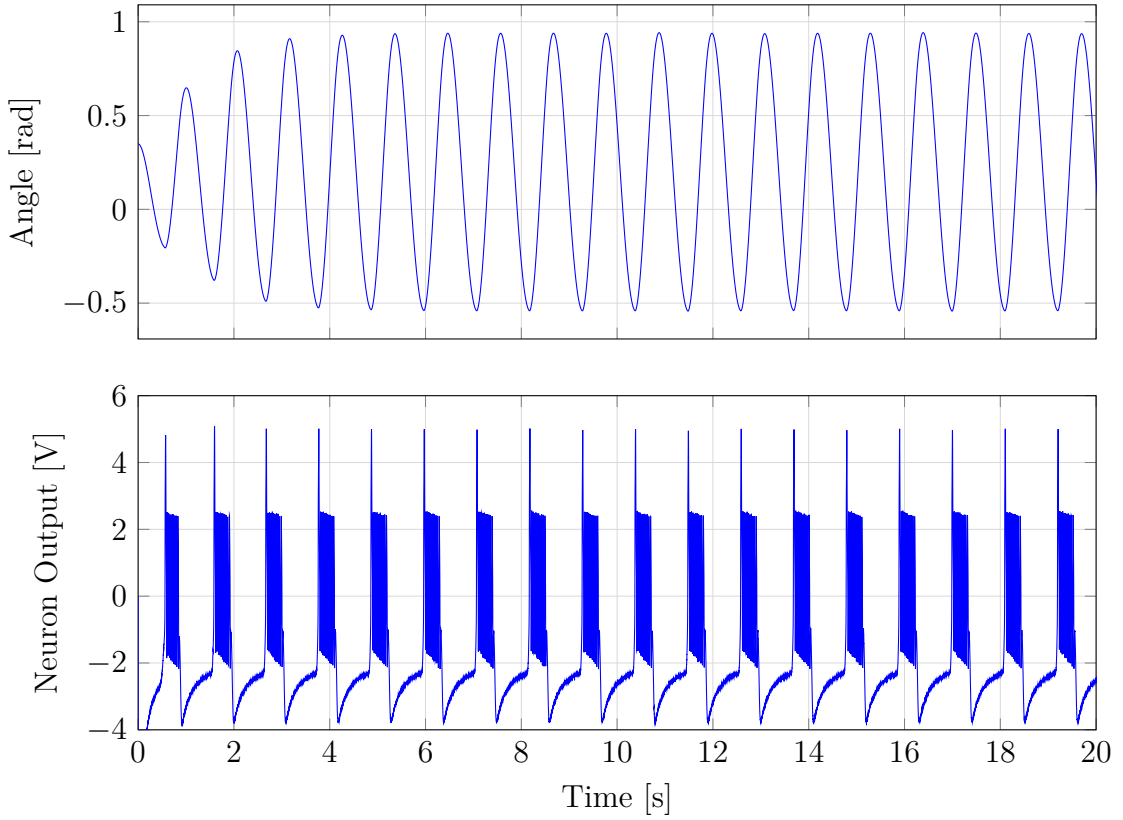


Figure 4.6: Simulation of a well parameterized single-neuron controller-pendulum system. Using mixed feedback with $\tau_{\max} = 10 \text{ N m V}^{-1}$ and $K_{\text{feed}} = 1$.

was performed. In addition, two different output gain $\tau_{\max} = 1 \text{ N m V}^{-1}$ and $\tau_{\max} = 10 \text{ N m V}^{-1}$ were used to determine the appropriate force to effectively control the system.

Figures 4.7 and 4.8 show the responses with a low output gain on the torque while figures 4.9 and 4.10 show a high output gain. The first thing that is clear when looking at these figures is that $\tau_{\max} = 1 \text{ N m V}^{-1}$ is not high enough for this system to sustain large oscillation and, by extension, exercise good control over the oscillation. Indeed, the maximum range of oscillation is lower than 0.3 rad while for $\tau_{\max} = 10 \text{ N m V}^{-1}$ the oscillations reach nearly 3.14 rad. Thus, maps using $\tau_{\max} = 10 \text{ N m V}^{-1}$ are more useful because they display what will be used later. However, the other maps can still be useful for identifying behaviors in specific situations.

Figures 4.7a, 4.8a, 4.9a and 4.10a shows that mixed and spiking feedback can generate oscillations with lower I_{app} compared to the sinusoidal feedback. Now looking at Figures 4.9b and 4.10b shows that the mixed and spiking feedback can reach the oscillations with the greatest amplitudes.

Now looking at $I_{\text{app}} = -1 \text{ A}$ and especially $I_{\text{app}} = 0 \text{ A}$, the maps of the controller with feedback become closer to the map of the controller without feedback. This indicates that those higher I_{app} are not as relevant because they lead to behavior

close to no feedback, which can only lead to poor control. The range of oscillation maps confirms this because they show that higher I_{app} lead to far lower oscillation amplitudes. This shows the poorness of the control because efficient control should be able to generate high-amplitude oscillations.

In figure 4.10b the map of the mixed or spiking feedback when $I_{app} = -2\text{ A}$ seems to validate figures 3.7 and 3.8 as lowering g_{s-} is well correlated with the amplitude of the oscillations. This shows the link between the value of g_{s-} and the power contained in a burst.

Now, comparing the different feedback, it seems that the sinusoidal feedback has a behavior different from the mixed and spiked feedback. Meanwhile, the mixed and spiked feedbacks have very similar behaviors. This can be explained by the mixed feedback having a spike-like behavior near $\dot{\theta} = 0$ and the spike feedback neuron is excited when near to $\dot{\theta} = 0$. Thus, both types of feedback generate a spike when the angular velocity is low. However, note that in figure 4.8 the spiking feedback generates relatively more oscillation than the mixed feedback model.

The analysis of the maps seems to point toward low I_{app} , high τ_{max} , high strength of feedback, and mixed or spiking feedback as the best controller.

However, the analysis highlighted some zones of interest. Figure 4.11 shows the oscillation generated in three zones of interest.

The first four rows of traces show the behavior of all feedback types at the specific point seen in figure 4.10 where the uncoupled bursting neuron can generate large oscillations. The idea is to investigate why a system receiving no information about the state of the pendulum can generate "good" oscillation and what adding feedback can do in the same situation. Looking at the traces of the angle θ for the case without feedback, it appears that the frequency of bursting coincides with the frequency of the pendulum. The match is not perfect because the amplitude of oscillation varies slightly but it still remains within a small range. Considering the effect of the feedback when using the same parameter for bursting and choosing the highest sensory feedback strength, the oscillation pattern does not change. Some phase is introduced between feedback types because the bursting patterns are not in sync, but the shape of a burst and the inter-burst frequency are nearly the same in all cases. This highlights a critical behavior, if the neuron has a high base excitatory current, which is the case here since figure 3.3 indicates that bursting with these parameters starts slightly above $I_{app} = -2\text{ A}$, then the feedback becomes less effective and thus the connection between the neuron and the mechanical system is diminished. This is the opposite of the desired behavior.

Next, the fifth and sixth rows in figure 4.11 show a more desirable behavior.

Here, the mixed and neuron feedback are shown with a better set of parameters as seen in figure 4.10. Here, the lower base current allows the feedback to dominate the activation of the neuron. This results in a strong connection between the neuron and the mechanical system. The oscillation traces confirm this because they have a greater amplitude than the parameter discussed before and are extremely regular. The regularity of these oscillations completely demonstrates the link between the neuron and the pendulum because a perfect match between the inter-burst fre-

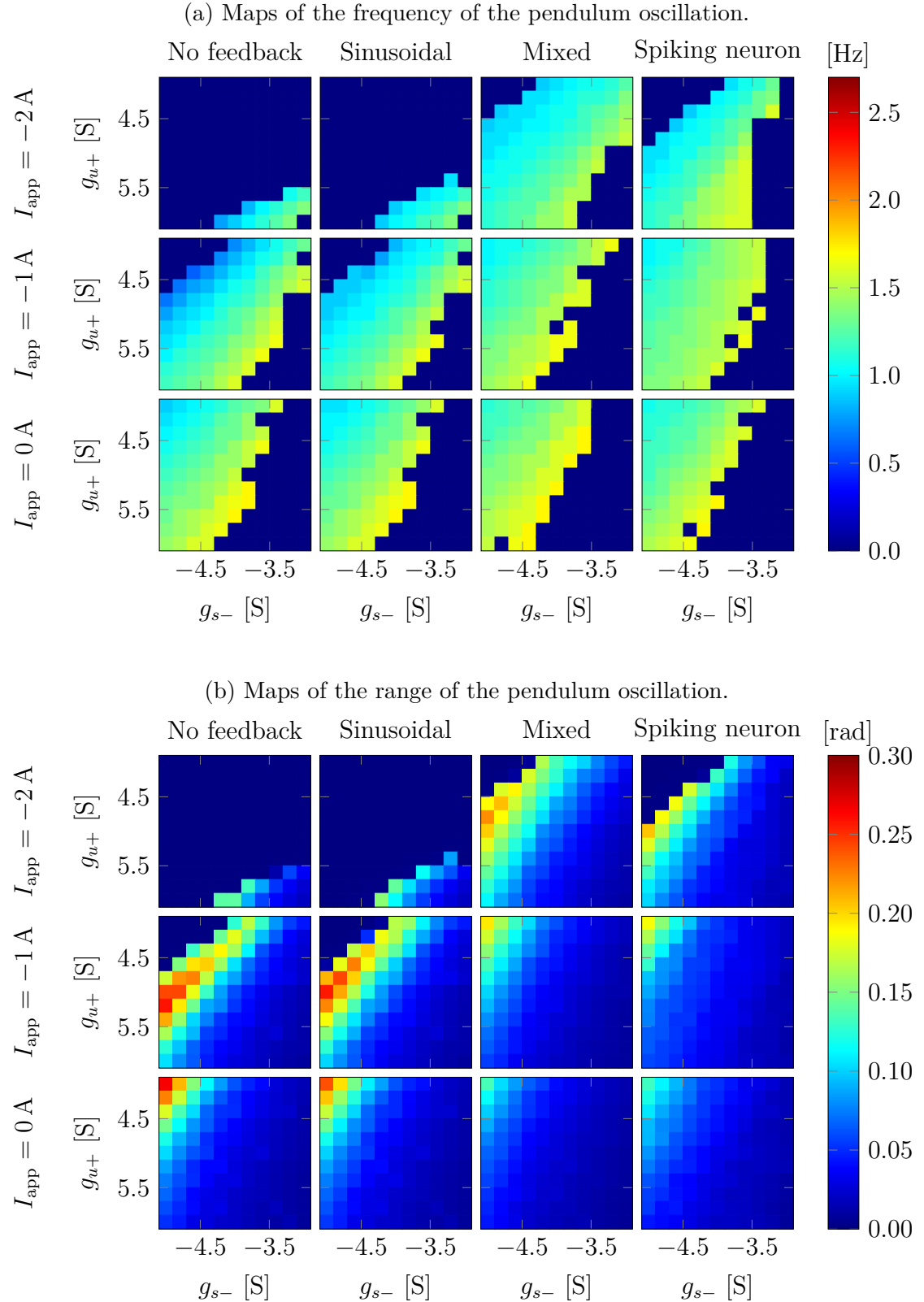


Figure 4.7: Single-neuron controller-pendulum system behavior with $\tau_{\max} = 1 \text{ N m V}^{-1}$ and $K_{\text{feed}} = 1$ or $g_{\text{syn}} = 1 \text{ S}$.

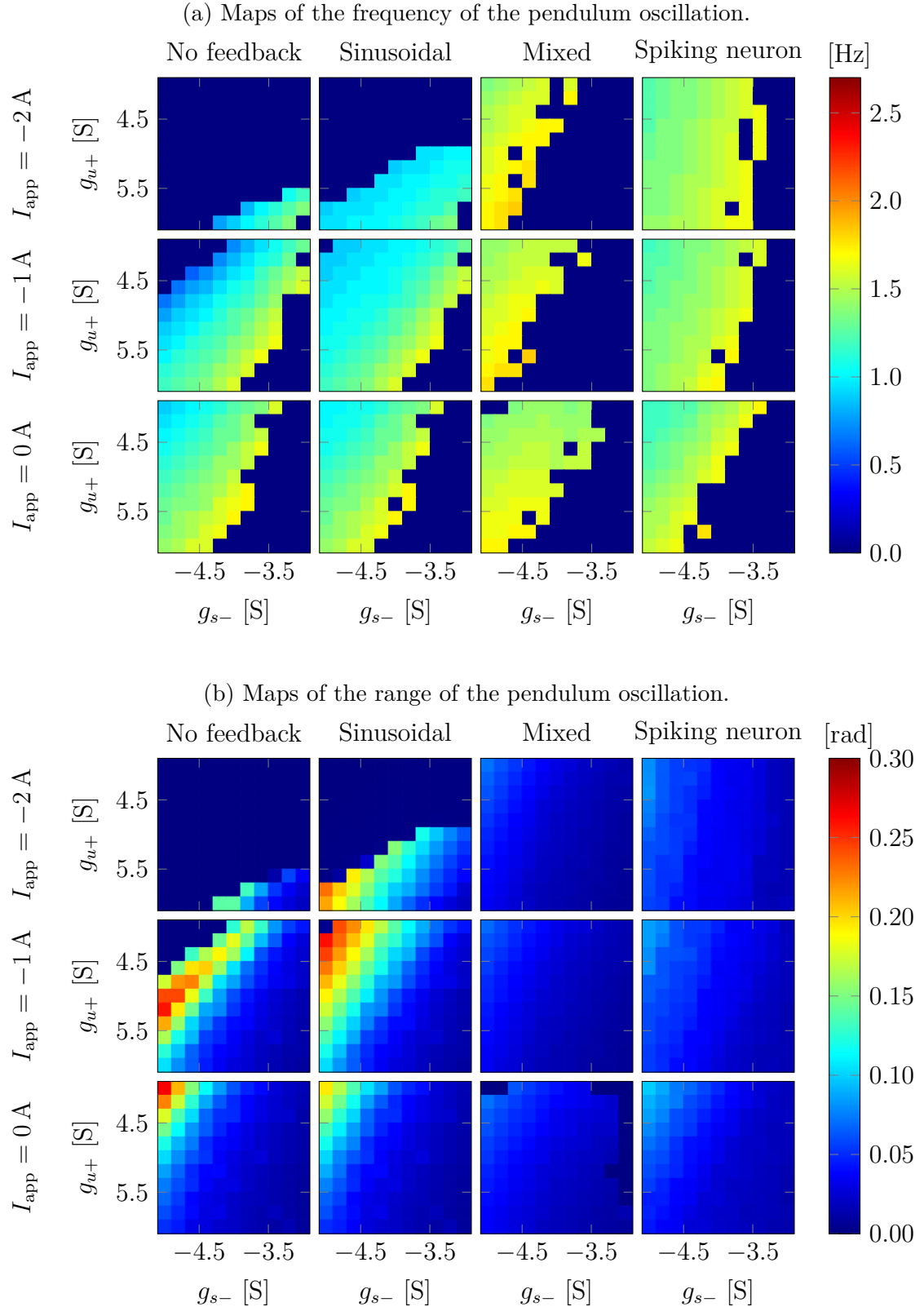


Figure 4.8: Single-neuron controller-pendulum system behavior with $\tau_{\max} = 1 \text{ N m V}^{-1}$ and $K_{\text{feed}} = 5$ or $g_{\text{syn}} = 3 \text{ S}$.

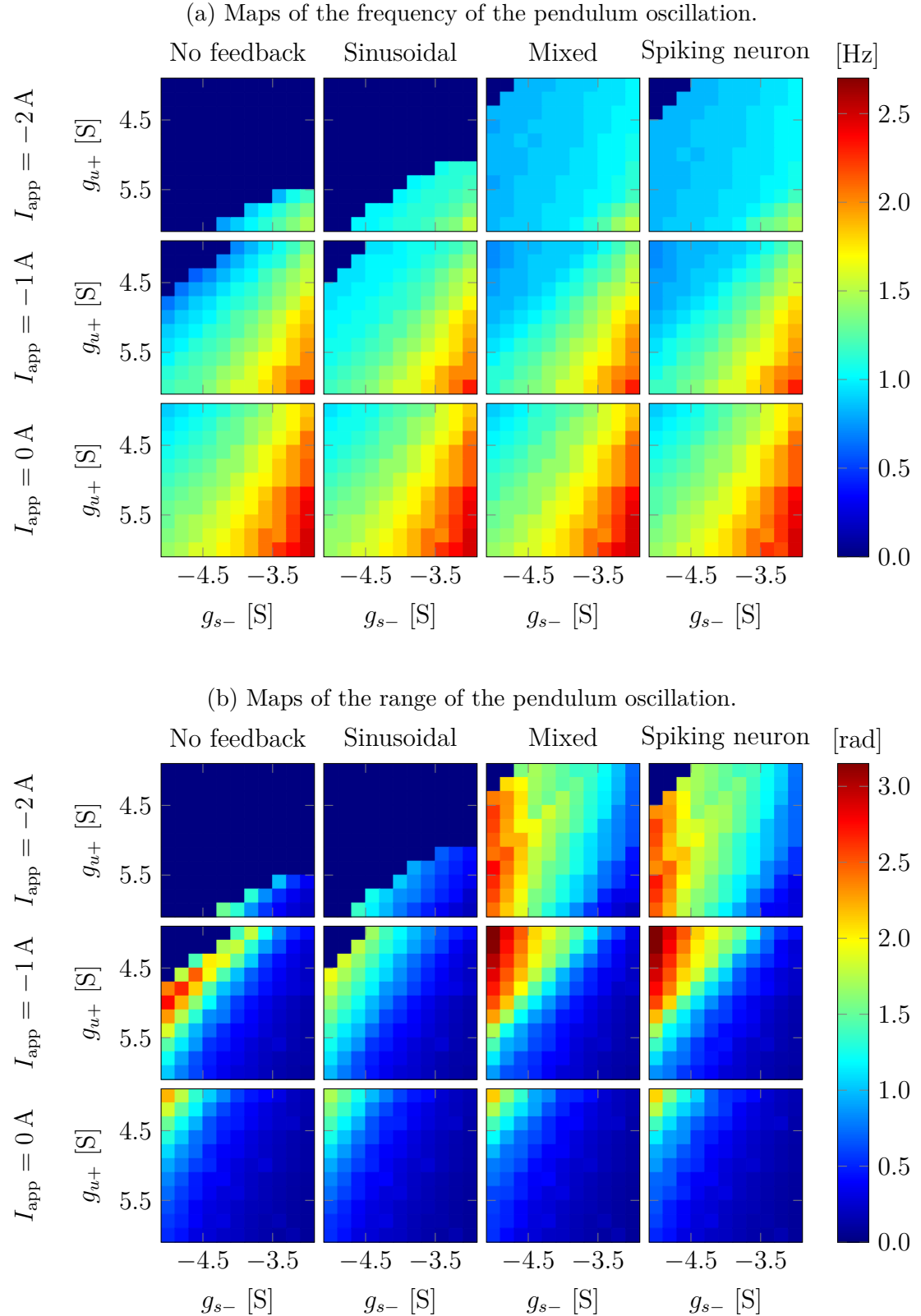


Figure 4.9: Single-neuron controller-pendulum system behavior with $\tau_{\max} = 10 \text{ N m V}^{-1}$ and $K_{\text{feed}} = 1$ or $g_{\text{syn}} = 1 \text{ S}$.

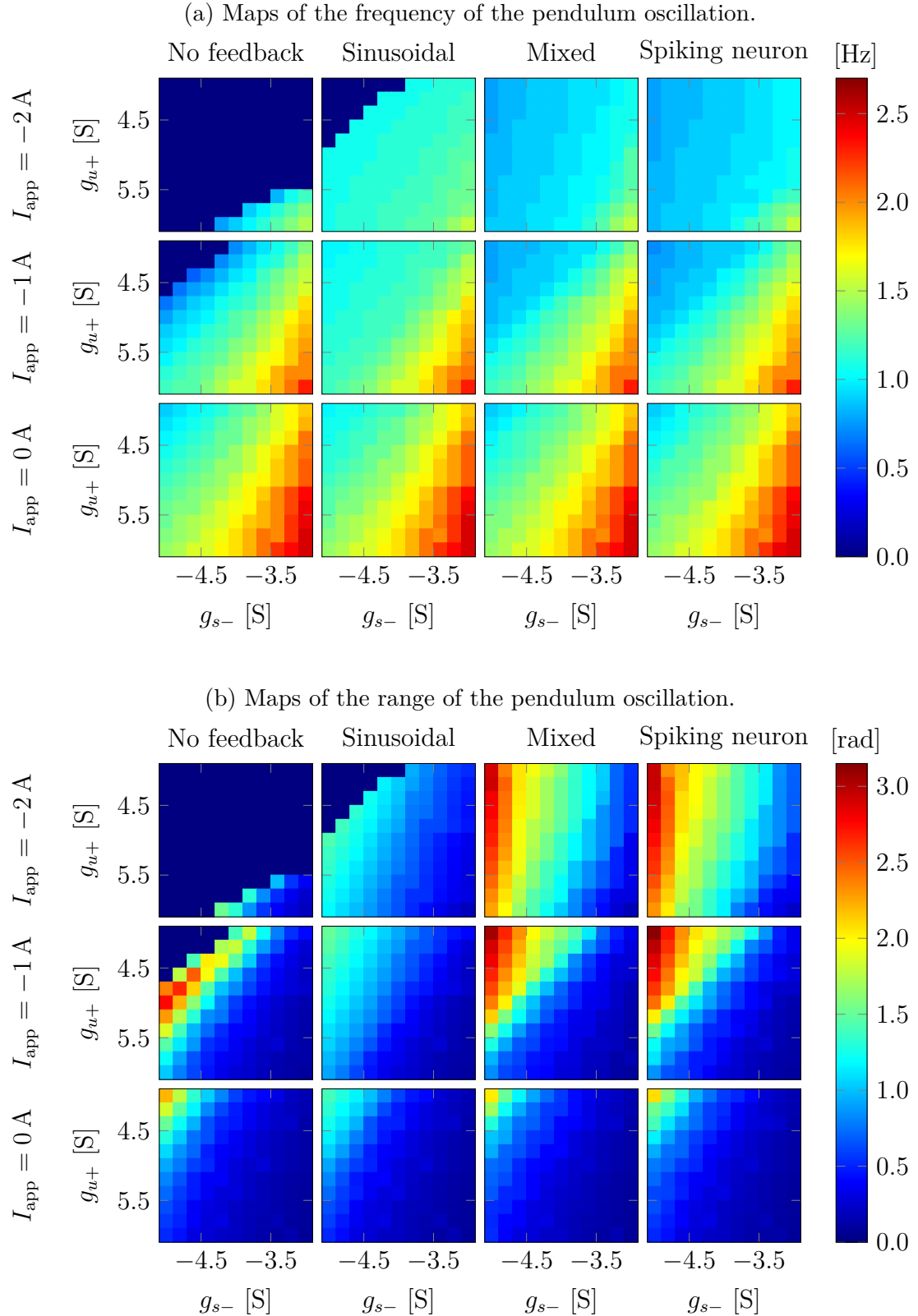


Figure 4.10: Single-neuron controller-pendulum system behavior with $\tau_{\max} = 10 \text{ N m V}^{-1}$ and $K_{\text{feed}} = 5$ or $g_{\text{syn}} = 3 \text{ S}$.

quency and the oscillation frequency is only possible if the bursting is modulated by feedback.

Finally, for most of the analysis, the mixed and neuronal feedbacks were grouped together and showed identical performances. However, they are not the same, and in specific cases, they display different behaviors. The seventh and eighth rows in figure 4.11 display this difference. The parameters were taken from figure 4.7 where the low current behavior seemed quite different. Indeed, the traces confirm that they are. The mixed feedback seems to be stuck in a behavior similar to that of the first row but with far smaller oscillation due to the lower gain on the torque. This appears clearly with the variation in the amplitude of each oscillation and the seemingly constant bursting of the neuron. Conversely, neuron feedback can generate far larger and more regular oscillations despite being subjected to the same parameters. This difference can be explained easily when considering the equations that forms the feedback. This boils down to the fact that mixed feedback is continuous, whereas neuron feedback is event-based. This may seem a bit strange because the mixed feedback, when declared in section 4.2.2 was described as generating pulses. However, looking back at the equations governing the feedback reveals that it only holds true if the angular velocity is high and then equation (4.4) is zero, except at the peak of the oscillation where the speed is close to zero. In the case where the torque is low, the system may become stuck in a pattern of tiny oscillations that, due to the limited torque and range, do not have the velocity to get out of the bump. Thus, mixed feedback can be abstracted as equation (4.3) plus one, which is feedback based only on position. In the neuronal case, the behavior is different. Even if the input to the spiking neuron is similar to the mixed feedback, passing this input into a spiking neuron transforms this continuous feedback into events. If the neuronal feedback is placed in the same position as the mixed feedback, it spikes at a relatively low frequency, leading to a more stable activation, allowing it to exit the position and generate larger oscillations.

4.3.2 Robustness of the sensorimotor loop

In a real controller, it is nearly impossible to achieve the exact theoretical parameters. Therefore, it is important to analyze the behavior of the controller when the parameters deviate from the ideal values. In the previous section, good parameters were found to be around $I_{app} = -2 \text{ A}$, $g_{s-} = -4 \text{ S}$ and $g_{u+} = 5 \text{ S}$.

The classical way of performing such an analysis is simply to use Monte Carlo by sampling the parameters from a certain distribution centered around the ideal values and plotting the distributions of the relevant output value to visualize the influence of these changing parameters on the control. Before doing this, the robustness can already be assessed in figures 4.7 to 4.10 by looking at the change in values around the chosen parameters. Since $\tau_{\max} = 10 \text{ N m V}^{-1}$ and $K_{\text{feed}} = 5$ or $g_{\text{syn}} = 3 \text{ S}$ gave the best controller results, those parameters will be used and thus only figure 4.10 is relevant. The maps of frequency and oscillation in that figure show that there is relative stability around the good parameters, at least in the g_{s-} and g_{u+} dimensions.

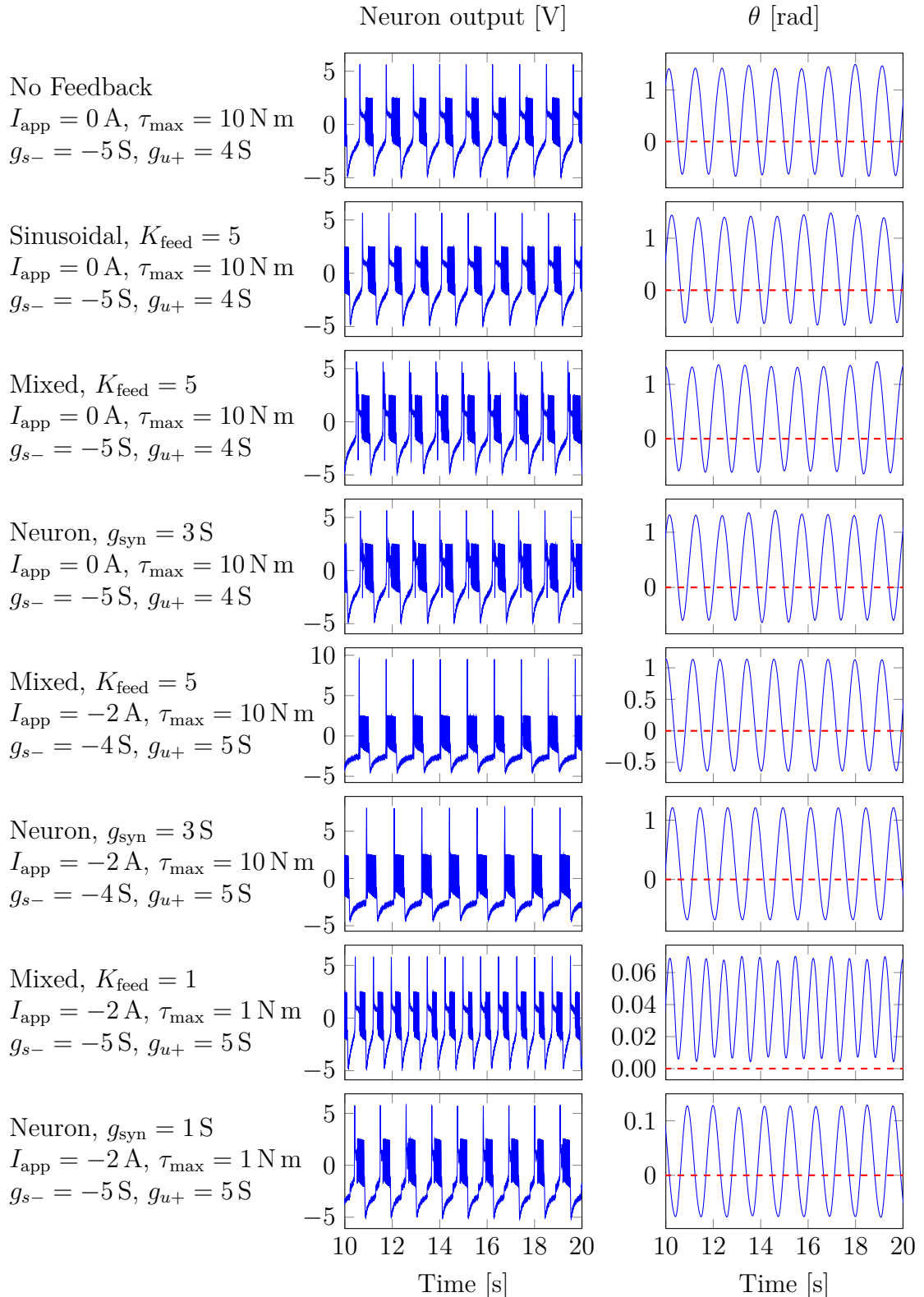


Figure 4.11: Temporal behavior of a single-neuron controller-pendulum system under different parameters and with different feedback.

Here, relative stability means that the gradients of the frequency and amplitude maps are relatively low in amplitude and that there are no large discontinuities.

To have a point of comparison and further prove the point of the previous chapter, the fragile bursting displayed in figures 3.5 and 3.6 is chosen to compare the good parameters with a set of poor parameters. To represent this behavior the fragile bursting has the parameters $I_{app} = 0 \text{ A}$, $g_{s-} = -0.1 \text{ S}$ and $g_{u+} = 4 \text{ S}$. $I_{app} = 0 \text{ A}$ was chosen to place the fragile neuron in a similar situation to the robust neuron, i.e., before natural bursting.

With all that, figure 4.12 displays the histograms resulting from the Monte Carlo simulations on the robust and fragile neuron coupled with all feedback previously defined.

The first observation that can be made by looking at the distribution of in figure 4.12a is that the robust neuron is very precise and can maintain oscillation at the same frequency, except for the mixed feedback, which displays two very close frequencies. On the other hand, the fragile neuron is much worse because the dominant frequency is spread over a large range of frequencies. Especially in cases with no feedback and sinusoidal feedback. However, the mixed feedback is again different from the others, with a behavior very similar to that of the robust neuron, except at a slightly higher frequency.

Looking at the amplitude of oscillation in figure 4.12b gives a clearer picture of what is happening. The amplitudes of oscillations of the robust neuron are far larger than those of the fragile neuron. In fact, apart from the mixed feedback, the range of oscillation of the fragile neuron is nearly zero, proving that it is ineffective at generating oscillation. It is also interesting to note that the range of the robust neuron with no feedback is perfectly zero, which is normal because the bursting neuron is inactivated. However, this is not the case for the fragile neuron, which again shows that, as presented in figure 3.6, the fragile neuron is very sensible to noise.

Figure 4.13 is a zoom in on the behavior of the robust neuron. This figure highlights what was previously observed. The principal oscillation frequencies are shown to be very stable. Sinusoidal and spiking neuron feedbacks lead to a single frequency, whereas mixed feedback leads to two separate frequencies, with no distribution in the frequency range. Now looking at the range of oscillation, while all feedback span a similar range of around 0.1 rad the sinusoidal feedback seems to spread more than the other two feedback. The other feedbacks have a large narrow peak and then a small wider peak with a range without oscillation between. This shows a more precise control of the mixed and spiking feedback. Yet, this second smaller is strange given the single frequency found. This behavior could have been explained in the case of mixed feedback because it exhibits two separate frequencies; however, the number of simulations in the second peak of higher amplitude is higher than the number of simulations in the smallest frequency; therefore, this cannot explain the entire peak. This behavior arises from the fact that the dominant frequency is the frequency with the highest power; thus, it can be quite stable even if the oscillation changes slightly.

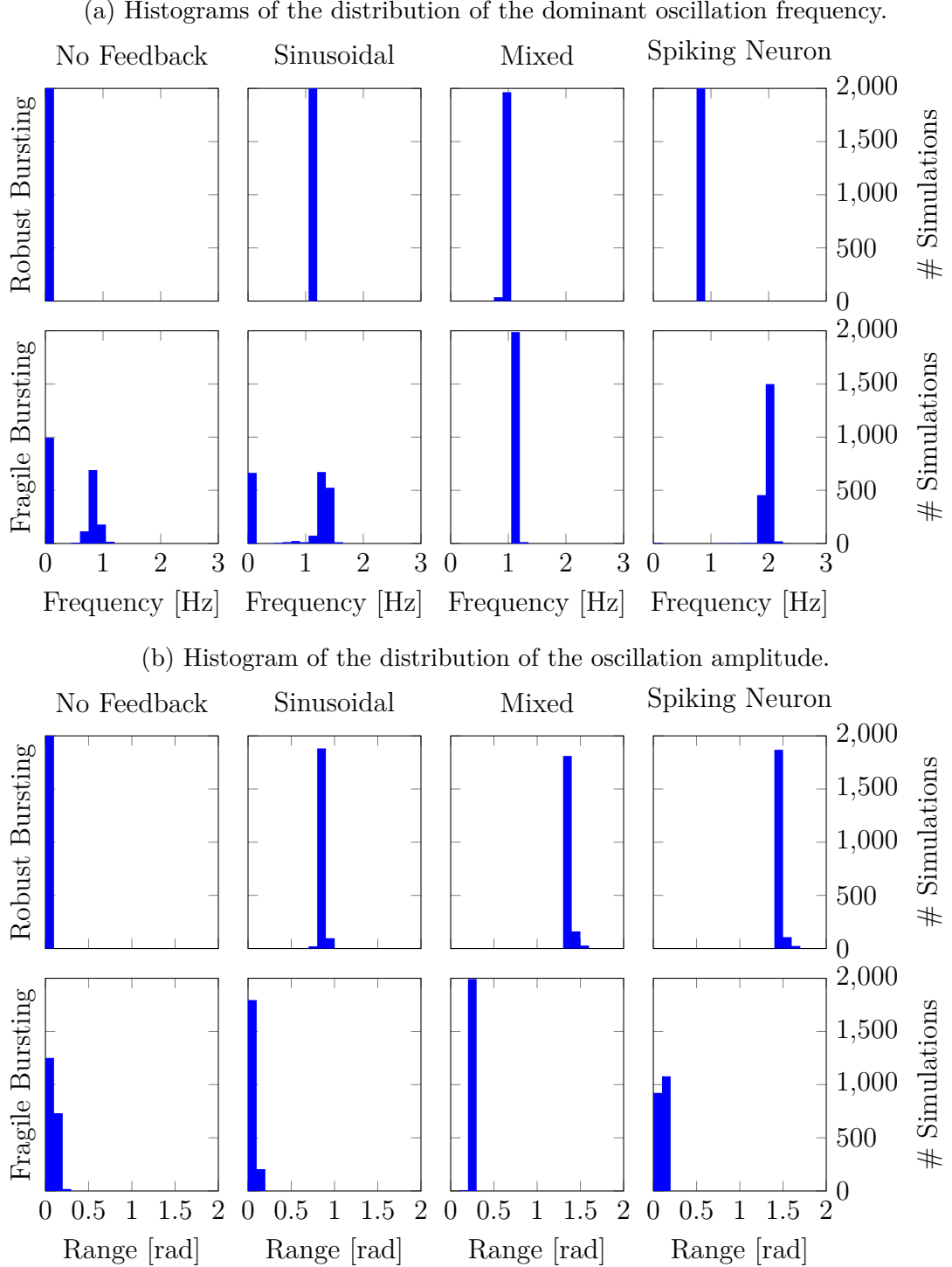


Figure 4.12: Comparison of the robustness of all feedback on the single-neuron controller-pendulum system using Monte Carlo analysis. The parameters of robust bursting were sampled from $I_{app} \sim \mathcal{N}(-2, 0.05^2)$ A, $g_{s-} \sim \mathcal{N}(-4, 0.03^2)$ S and $g_{u+} \sim \mathcal{N}(5, 0.05^2)$ S. The parameters of fragile bursting were sampled from $I_{app} \sim \mathcal{N}(0, 0.05^2)$ A, $g_{s-} \sim \mathcal{N}(-0.1, 0.03^2)$ S and $g_{u+} \sim \mathcal{N}(4, 0.05^2)$ S. Both neurons used $g_{f-} = -2$ S, $g_{s+} = 6$ S, $\tau_{max} = 10$ N m V $^{-1}$ and $K_{feed} = 5$ or $g_{syn} = 3$ S.

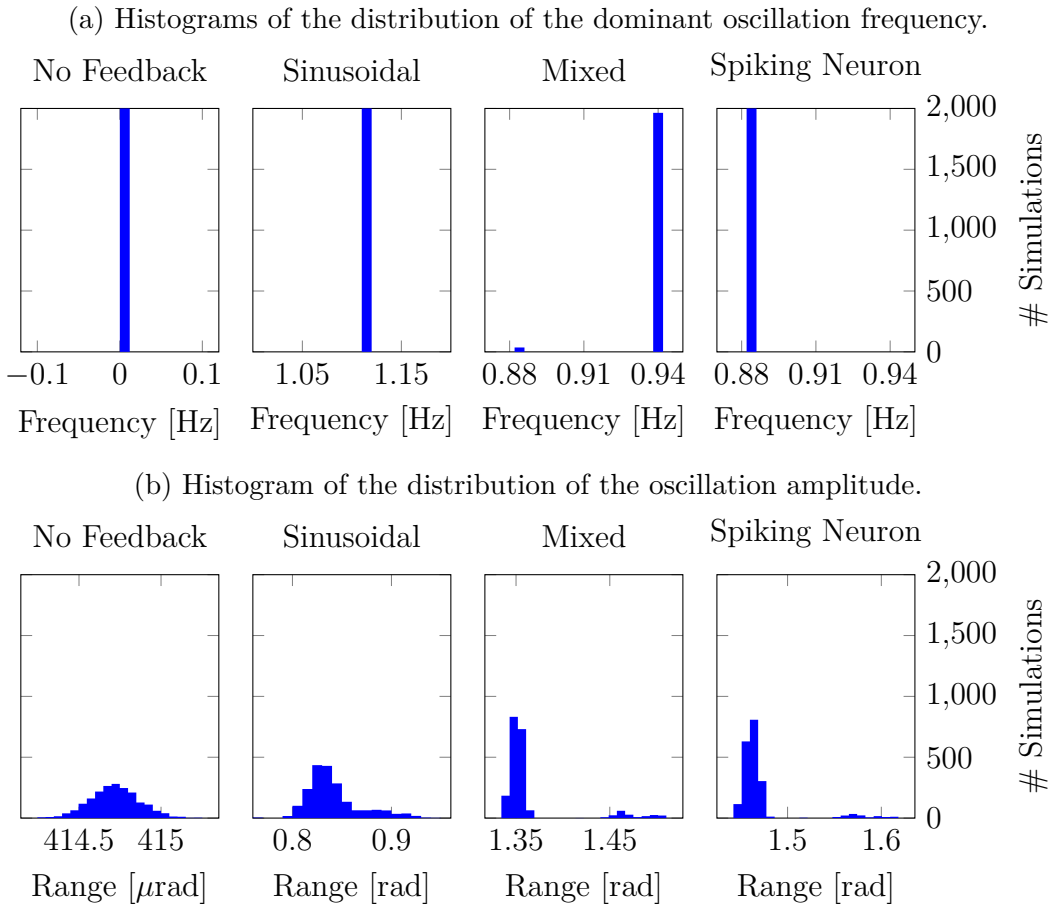


Figure 4.13: Comparison of the robustness of all feedback on the single-neuron controller–pendulum system using Monte Carlo analysis. The bursting parameters were sampled from $I_{\text{app}} \sim \mathcal{N}(-2, 0.05^2)$ A, $g_{s-} \sim \mathcal{N}(-4, 0.03^2)$ S and $g_{u+} \sim \mathcal{N}(5, 0.05^2)$ S. The bursting also used $g_{f-} = -2$ S, $g_{s+} = 6$ S, $\tau_{\max} = 10$ N m V $^{-1}$ and $K_{\text{feed}} = 5$ or $g_{\text{syn}} = 3$ S.

4.4 Two neuron "push-pull" controller

The next step in the controller design is to make it symmetrical by adding a new bursting neuron and its associated feedback block. In addition, to enforce the alternating activation of bursting neurons, inhibitory synapses connect both neurons. This turns the two neurons into a half-center oscillator. This is done to avoid simultaneous activation of the neurons because it would be suboptimal to push in both rotational directions at the same time.

The feedback to the new bursting neuron will be tailored to mirror the feedback to the first neuron so that the new neuron activates during the other half of the rotation plane.

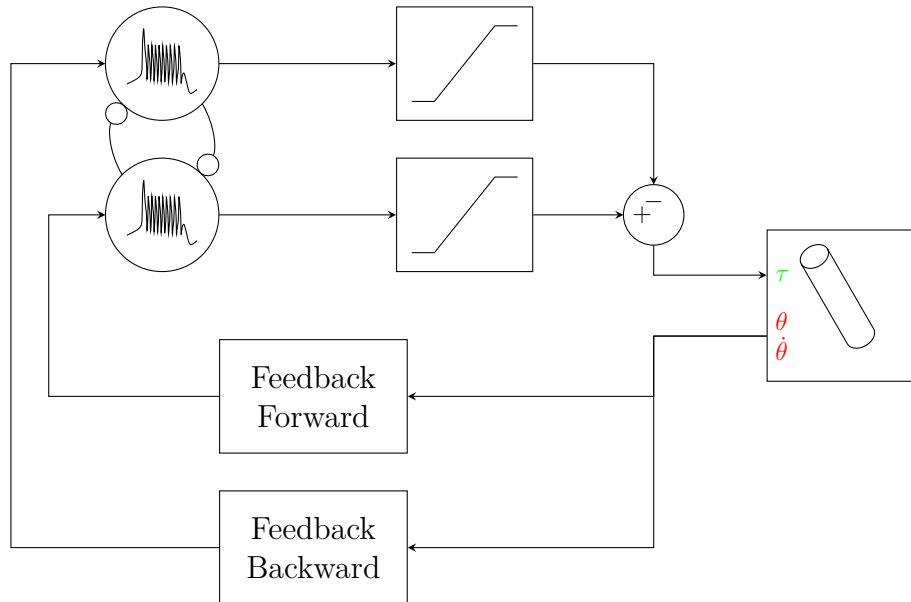


Figure 4.14: Diagram of the sensorimotor loop for the two-neuron push-pull controller. The saturation block limits are 0 V to 1 V. The adding block also contains an internal output gain τ_{\max} . Inhibitory synapses link both bursting neurons.

Synapses have the same conductance because the system should be symmetrical. The common conductance is $g_{\text{syn}} = -1 \text{ S}$.

Figure 4.15 displays a realization of this controller. This shows that the addition of a neuron balances the oscillations. In addition, the neurons burst in perfect opposition, demonstrating HCO behavior. The large and regular oscillations indicate that the controller is well attuned to the mechanical system.

4.4.1 Performance of the sensorimotor loop

Similar to the tests for the single-neuron controller, the performance of this new controller can be accessed by its ability to generate a stable oscillation of large amplitude. Similarly, to study the proposed controller, the parameters of the bursting neuron g_{s-} , g_{u+} and I_{app} and the parameters of the strength of the feedback K_{feed}

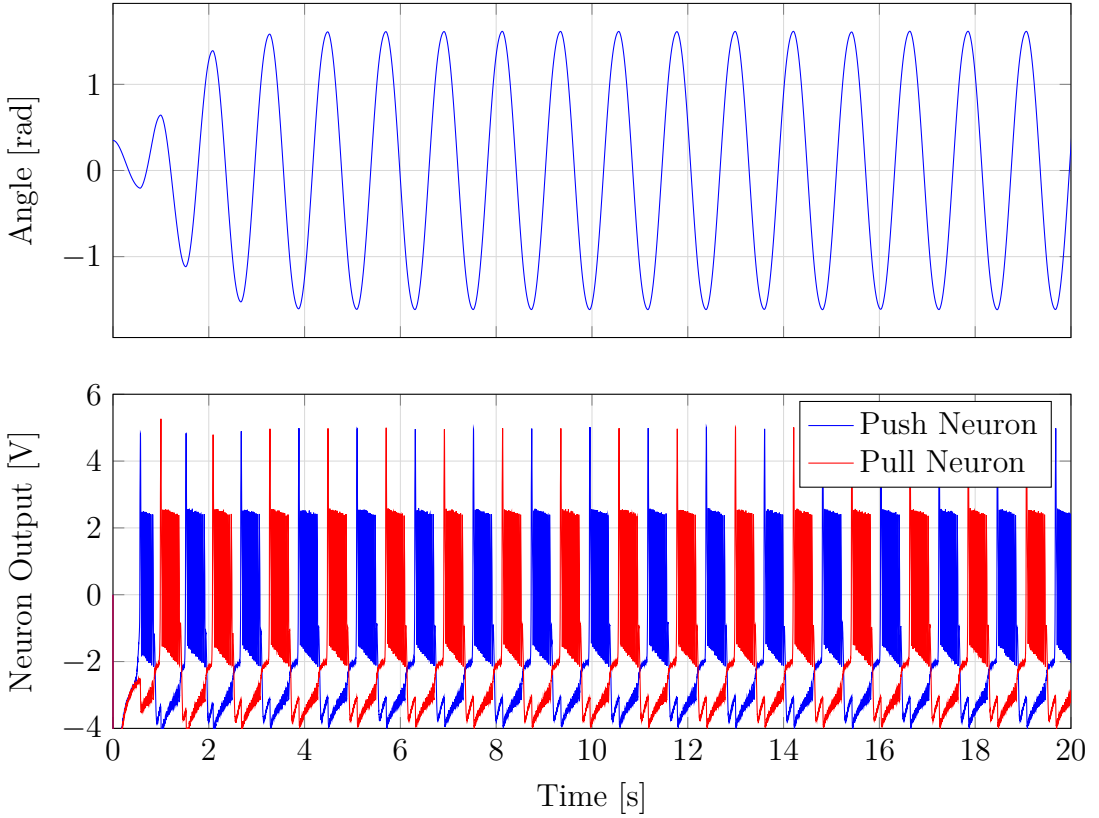


Figure 4.15: Simulation of a well-parameterized two-neurons push-pull controller–pendulum system. Using mixed feedback with $\tau_{\max} = 10 \text{ N m V}^{-1}$ and $K_{\text{feed}} = 1$.

or g_{syn} are varied. In addition, two different output gain $\tau_{\max} = 1$ and $\tau_{\max} = 10$ are studied to determine the appropriate force to effectively control the system.

Figures 4.16 to 4.19 display the behavior of the double neuron system in the same manner as figures 4.7 to 4.10 that were used for the single neuron controller.

The first thing that is flagrant in this situation is that sinusoidal feedback always leads to a far lower amplitude of oscillation compared with mixed or spiking neuron feedback. Except for $\tau_{\max} = 1$ and $K_{\text{feed}} = 5$ where figure 4.17 shows that the mixed feedback seems to fail. These lower oscillations are mostly due to the feedback being directly linked to the angle, leading to an activation that is too early and is not able to reach large amplitudes. Indeed in figures 4.16 and 4.17 while the lower amplitude is still visible, the amplitude displayed is far better because the lower maximum torque restricts the possible oscillation range.

Now, analyzing the amplitude part of the results clearly shows that the gain of adding another control neuron allows far greater amplitude to be reached. Figure 4.10 showed a maximum amplitude around π while figure 4.17 reaches 2π which is a full circle, which is impressive.

Interestingly, the CPG connection allows the system without feedback to generate sizable oscillations. This is linked to the natural oscillatory nature of the con-

nection (see figure 3.13). The controller lacking sensory feedback, these oscillations are naturally not attuned to the frequency of the pendulum and should generate very chaotic movement. Yet, this displays quite well the usefulness of the CPG, it intrinsically captures the necessary order of the actuation of this system.

As observed in the single-neuron controller, it seems that in figure 4.19 the maps of the range of oscillation validate the correlation between the value of g_{s-} that was seen in figures 3.7 and 3.8. However, it is less pronounced than in the case of a single-neuron controller, and the parameter g_{u+} seems to now play a role. Figure 3.14 shows that increasing g_{u+} increase the natural bursting frequency of the CPG, and ideally, this frequency should be close to or lower than the natural oscillation frequency of the pendulum. This poses a problem because oscillations of higher amplitude require a lower frequency.

Similar to the single-neuron controller, the analysis of the maps points toward a controller using mixed or spiking neuron feedback with low I_{app} , high τ_{max} and K_{feed} or g_{syn} as the best controller. It is the best in the sense that it can generate control of the oscillation in a reliable manner, and changing g_{s-} and g_{u+} allows to choose a desired amplitude of oscillation.

The analysis of the map has also led to the discovery of some interesting regions or phenomena. Figure 4.20 represent the temporal behavior of the controller in some of the most relevant regions.

The first of these regions is the region in figure 4.19b at $I_{app} = 0$ A where the controller without feedback is able to generate large oscillations and the controller using different feedbacks seems to exhibit a similar behavior, except for the controller using sinusoidal feedback. This is a region similar to another that was studied for the single-neuron controller in figure 4.11.

This region is explored in the first four rows. The first row displays the behavior of the controller without feedback. The neuron output clearly shows the CPG nature of the connection between the bursting neurons by the clear sequence of activation of the neurons. In addition, this trace explains how this controller can generate large oscillations without feedback. The bursting displays a plateau behavior that causes large oscillations because this behavior gives a large amount of momentum to the pendulum to move in one direction because the torque is applied constantly. This gives a large oscillation, but the plot of the angle shows that it does not sync well with the frequency of the pendulum and leads to some variance in the amplitude of the oscillation. The third and fourth rows show that the mixed and spiking neuron feedback have very similar behavior to the controller with no feedback. This was already seen in the case of the single-neuron controller, where increasing I_{app} reduces the feedback influence. However, the second row displaying the controller with sinusoidal feedback challenges this conclusion. This shows that with the same parameters the sinusoidal feedback generates smaller amplitudes and faster oscillations. This is due to the continuous nature of the feedback, which constantly pushes the neuron to act when the amplitude is sufficiently large. This implies two things. First, this changes the previously made conclusion, it seems that high I_{app} only reduce the effect of event-based feedback. Then, this shows that sinusoidal feedback

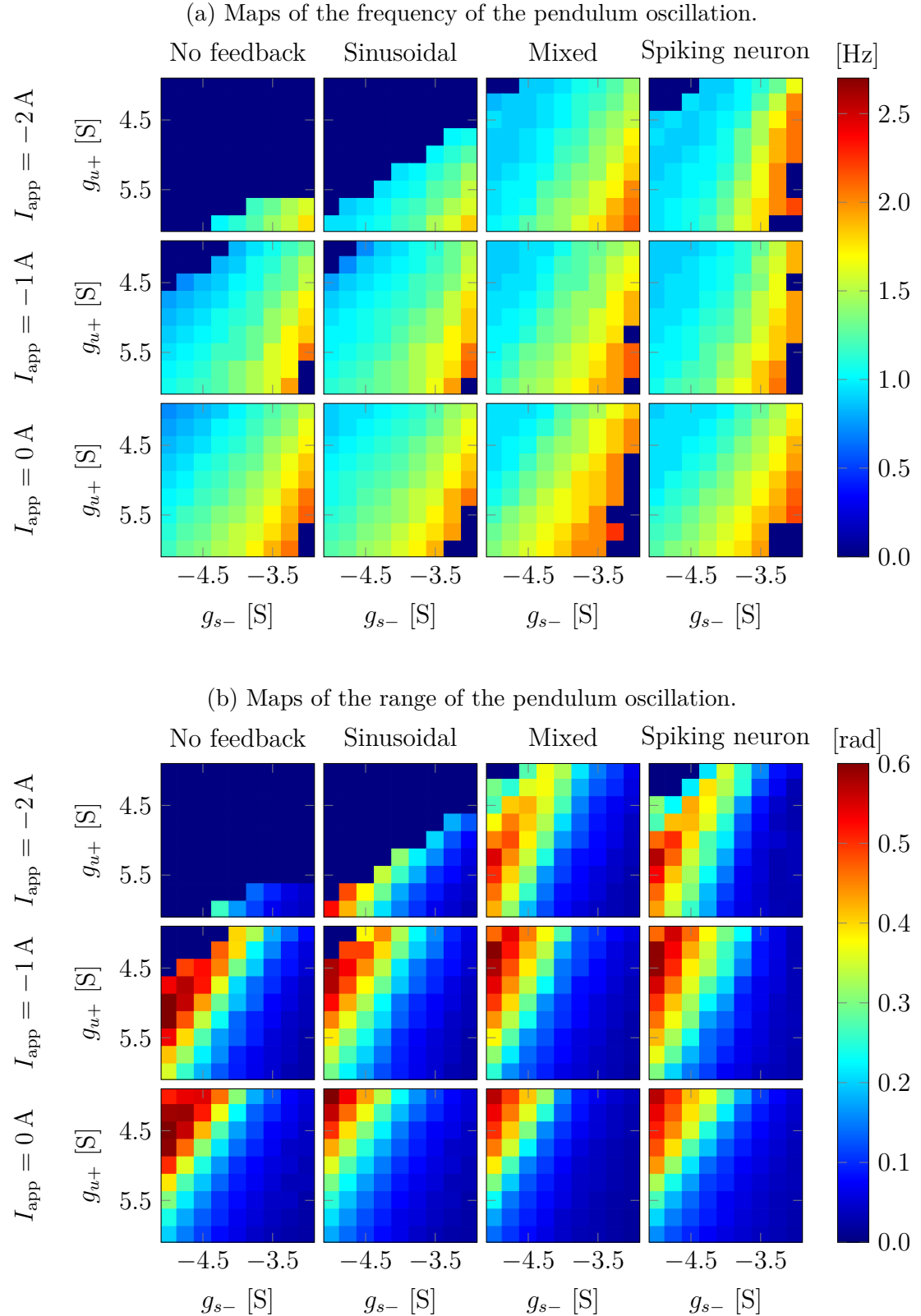


Figure 4.16: Double-neuron controller–pendulum system behavior with $\tau_{\max} = 1 \text{ N m V}^{-1}$ and $K_{\text{feed}} = 1$ or $g_{\text{syn}} = 1 \text{ S}$.

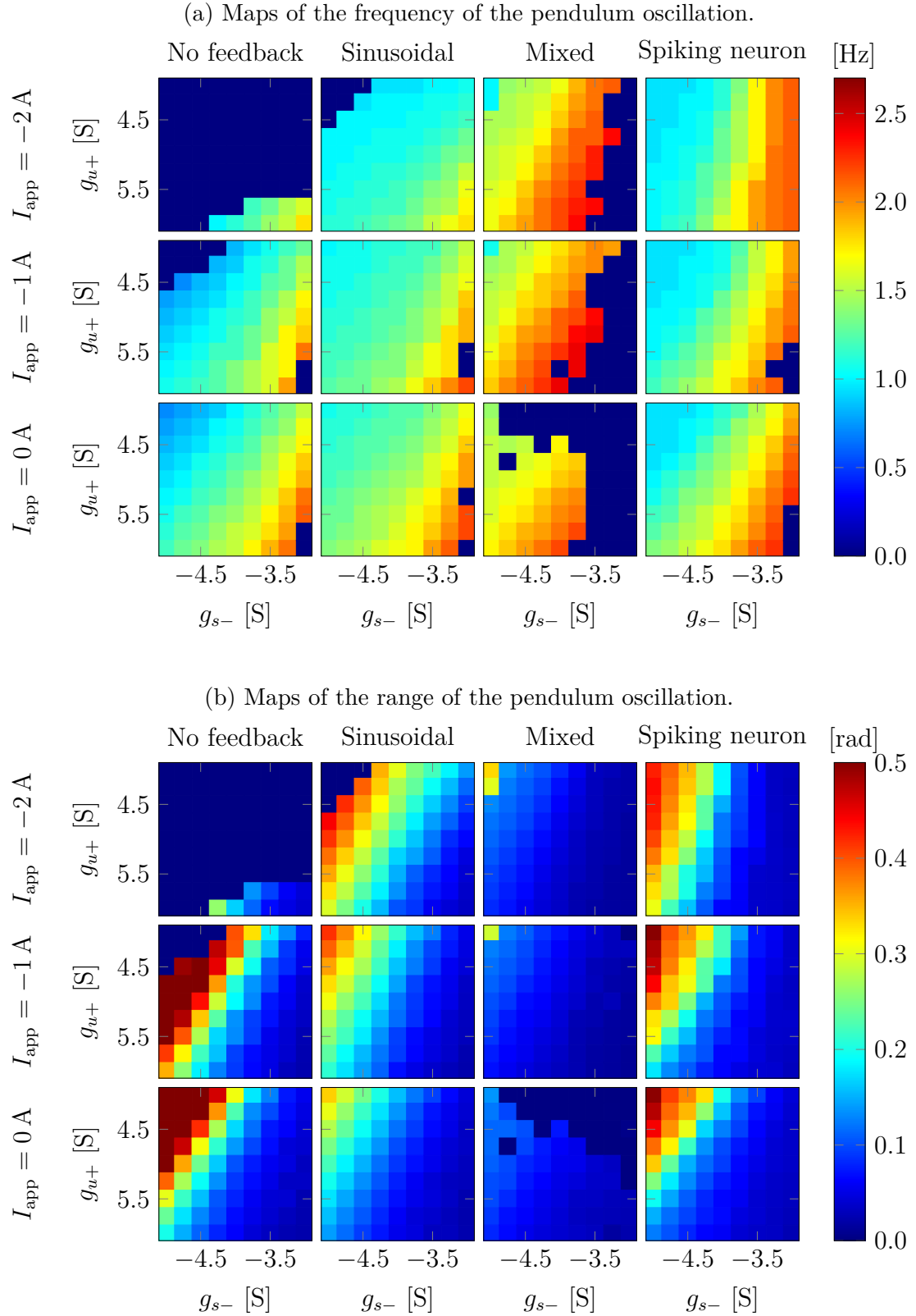


Figure 4.17: Double-neuron controller–pendulum system behavior with $\tau_{\max} = 1 \text{ N m V}^{-1}$ and $K_{\text{feed}} = 5$ or $g_{\text{syn}} = 3 \text{ S}$.

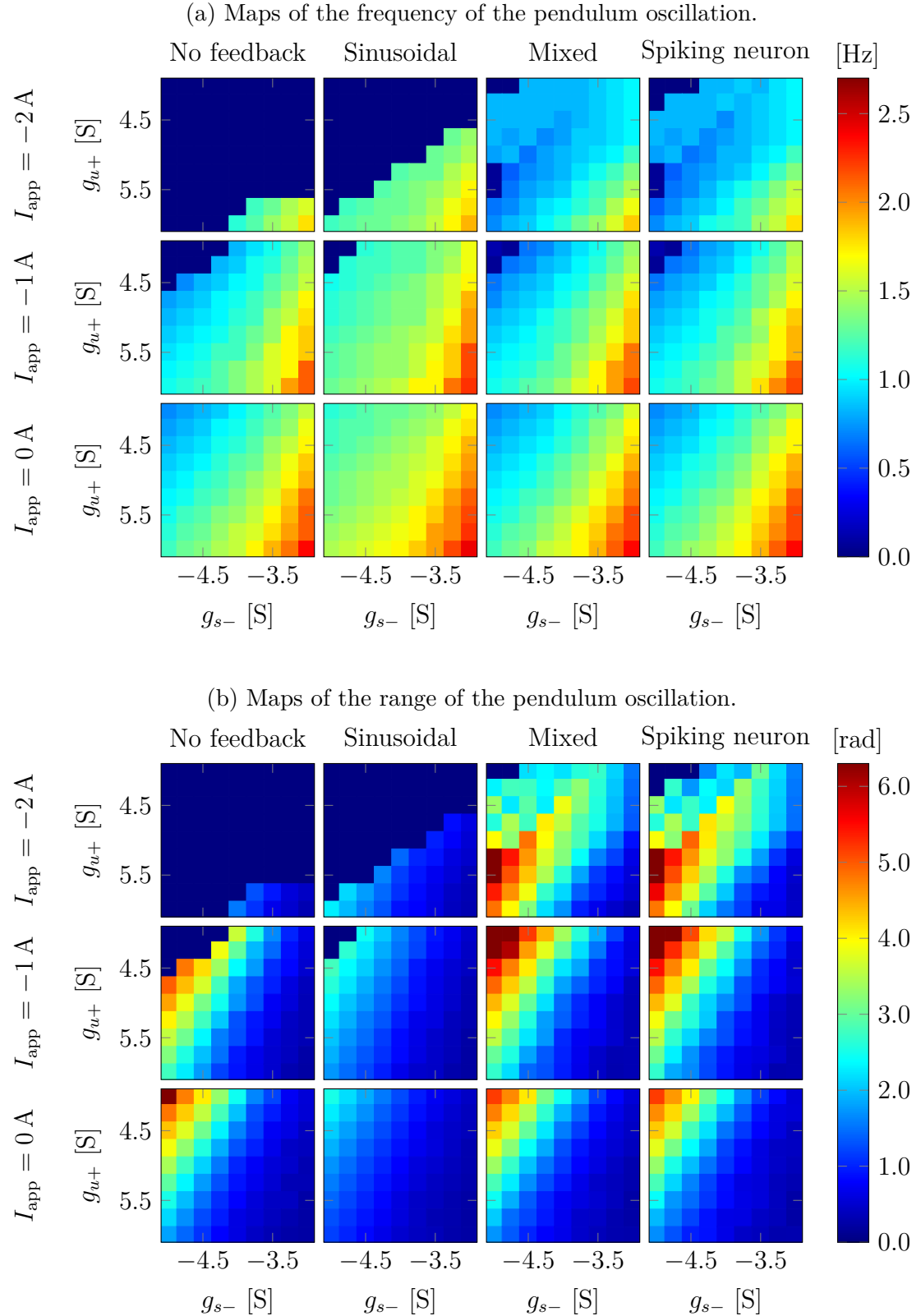


Figure 4.18: Double-neuron controller–pendulum system behavior with $\tau_{\max} = 10 \text{ N m V}^{-1}$ and $K_{\text{feed}} = 1$ or $g_{\text{syn}} = 1 \text{ S}$.

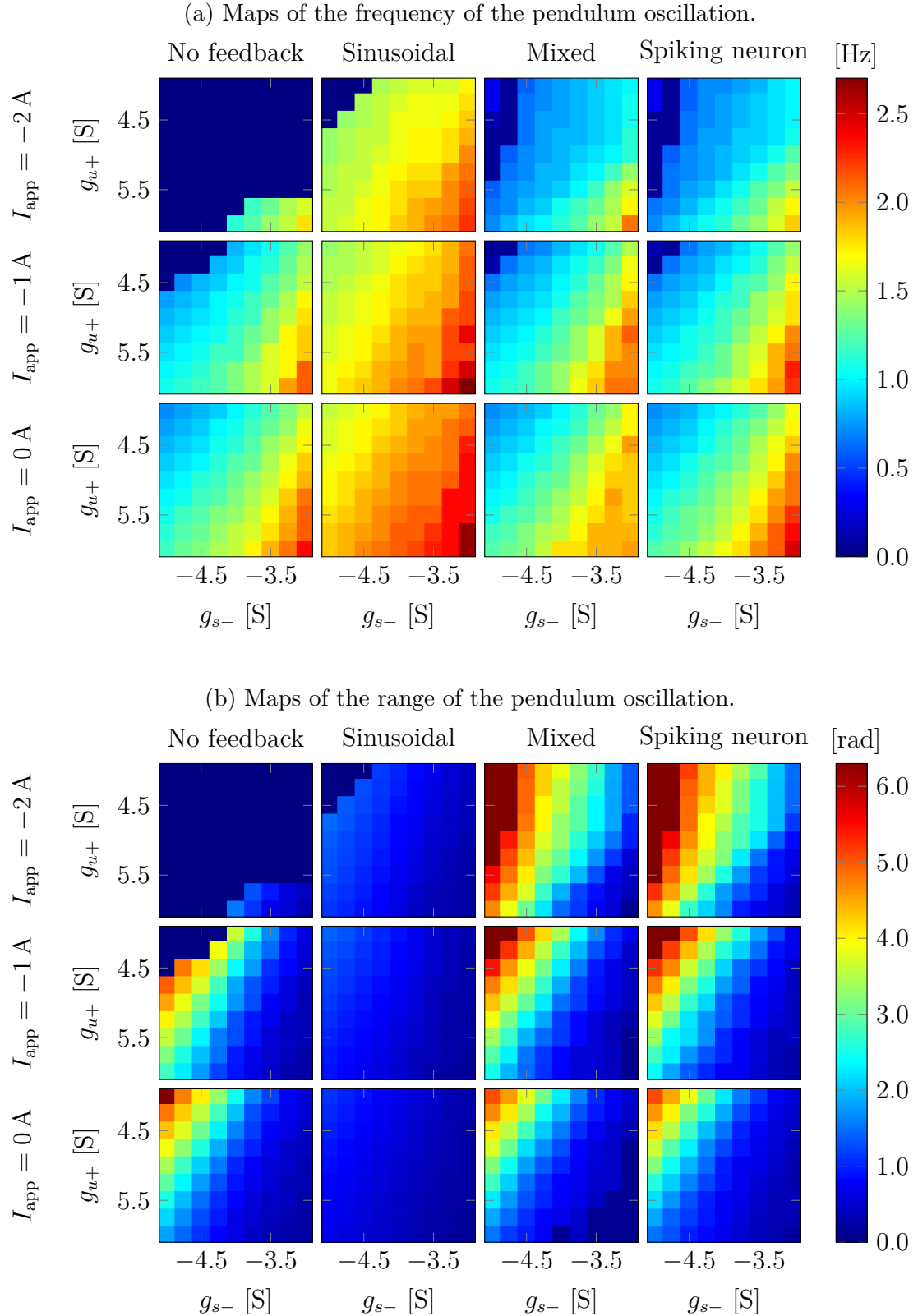


Figure 4.19: Double-neuron controller-pendulum system behavior with $\tau_{\max} = 10 \text{ N m V}^{-1}$ and $K_{\text{feed}} = 5$ or $g_{\text{syn}} = 3 \text{ S}$.

leads to a decision on a soft desired amplitude depending on the parameter K_{feed} chosen. Oscillations too large are not possible because they would excite the neuron so much that it would depolarize completely, and oscillation too low will not trigger the feedback and leads to either no oscillation if the CPG needs the feedback to burst or bad oscillation if it does not.

The fifth and sixth rows show the behavior of the mixed and spiking neuron controller with parameters taken from figure 4.19 where both feedbacks showed good performance. The spiking pattern and oscillation behaviors of both feedbacks are nearly identical, and there is only a slight temporal shift between them. The oscillations generated by both are very regular and show no variance in their amplitude. This again shows that event-based feedback coupled with low I_{app} create a very efficient controller.

The seventh and eighth rows resolve the strange behavior of the mixed feedback controller seen in figure 4.17 were the behavior of the mixed and spiking neuron controller differs despite being very similar in figures 4.16, 4.18 and 4.19. With the same parameter, the spiking neuron controller generates acceptable oscillations using bursting, even though they suffer from some variance in amplitude. However, the mixed controller generates far lower amplitude oscillation and is not bursting anymore, it just displays plateau potentials. This behavior was already observed in the single-neuron controller and has the same cause. To summarize the explanation seen in section 4.3.1 on page 40, the mixed feedback defined in section 4.2.2 loses its event-based nature when generating small oscillations and becomes continuous, thus losing performance. In comparison, the spiking neuron feedback, despite using a similar function, circumvents this issue by feeding it to a spiking neuron, which guarantees the event-based nature of the sensory feedback to the bursting neuron.

4.4.2 Robustness of the sensorimotor loop

Again, it is impossible to create a physical controller with the same parameters as the theoretical controller. Thus, evaluating the performance of the controller under small changes in the theoretical parameters allows the assessment of real-world performance. Similar to the single-neuron controller, the ideal parameters of the controller are around $I_{\text{app}} = -2 \text{ A}$, $g_{s-} = -4 \text{ S}$ and $g_{u+} = 5 \text{ S}$.

The robustness of the controller can already be assessed partially by figure 4.19 by observing that small variations of g_{s-} and g_{u+} around their ideal values only lead to small changes in the dominant frequency and amplitude.

To complete and confirm this analysis, the Monte Carlo method was applied to generate the distribution of the dominant frequency and the amplitude of oscillation when I_{app} , g_{s-} and g_{u+} are drawn from random distributions around the ideal values.

In addition, mirroring the analysis used for the single-neuron controller, another set of parameters for the bursting neuron was chosen for comparison with the bursting defined above. To further prove the point made in the previous chapter, the fragile bursting displayed in figures 3.5 and 3.6 will be the point of comparison. This neuron has the ideal parameters $I_{\text{app}} = 0 \text{ A}$, $g_{s-} = -0.1 \text{ S}$ and $g_{u+} = 4 \text{ S}$.

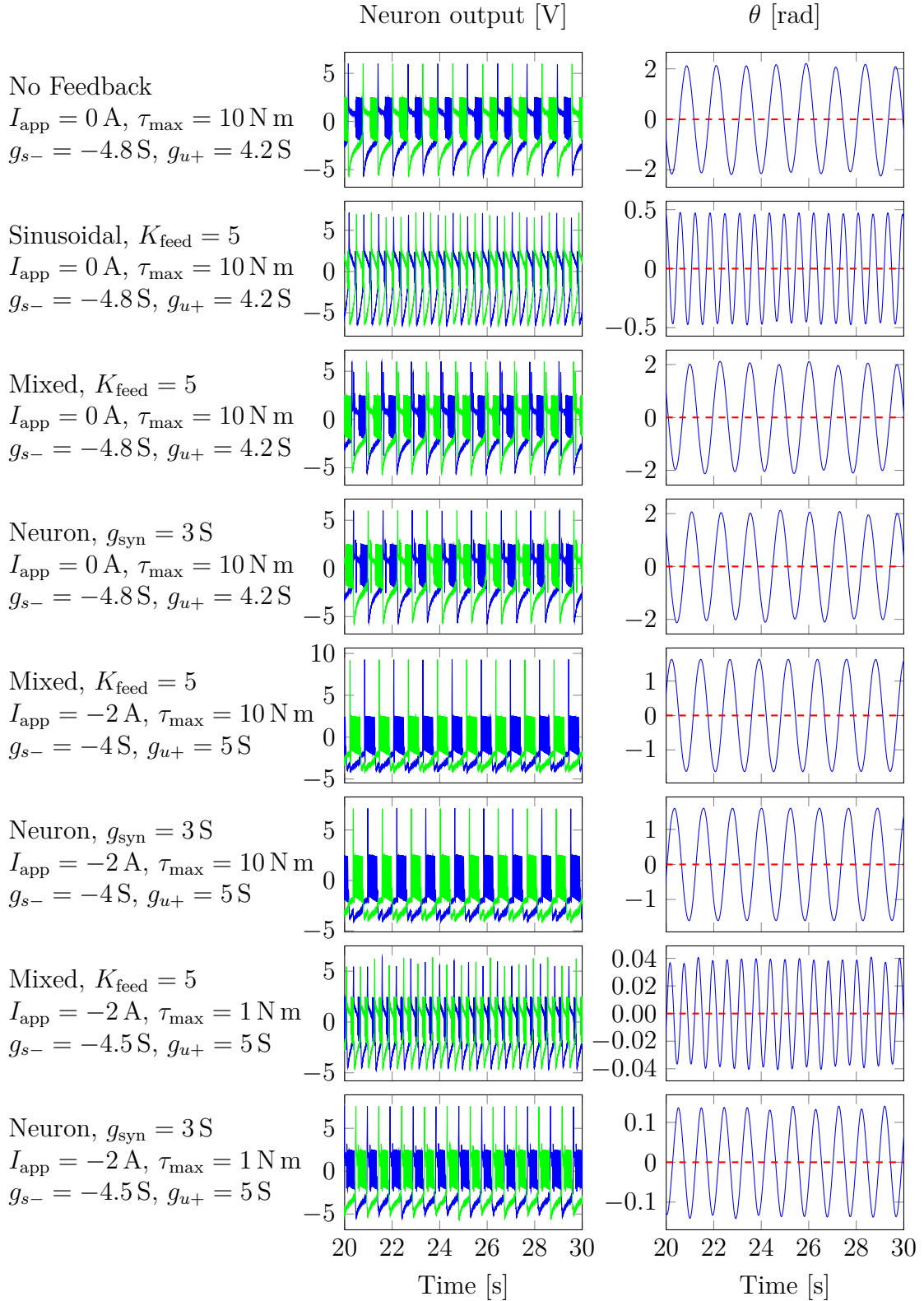


Figure 4.20: Temporal behavior of the double-neuron controller-pendulum system under different parameters and with different feedback. In the neuron output graphs, the blue and green traces represent the output of each neuron.

Figure 4.21 displays the results of the Monte Carlo simulation analysis. The first thing that is apparent, especially in figure 4.21b, is that the fragile bursting is unable to control the pendulum. The range of oscillation is always 0. No feedback can make it control the system even slightly. This is different from the behavior in the case of the single-neuron controller where figure 4.12b showed that at least the mixed feedback was able to allow the fragile bursting to somewhat control the pendulum. Note that in the case of the spiking neuron, some oscillations were generated since figure 4.21a shows a distribution of frequencies. However, the range of oscillations all being grouped to zero shows that these oscillations are too poor to be useful. This clearly demonstrates the fragile nature of this bursting, as the connection in a simple HCO pattern completely destroys the control capabilities of the neuron.

Now, looking at the distribution of the frequencies of the robust bursting in figure 4.21a it seems that for all feedback types, the dominant frequency of oscillation is very precise. However, the distribution of the amplitude of oscillation in figure 4.21b shows that the sinusoidal feedback has nearly no variation in amplitude, whereas mixed and spiking neuron feedback do. However, the oscillations of the mixed and spiking neuron controllers are also far larger than those of the sinusoidal controller. This shows that there is a certain trade-off between the size and variability of the oscillation amplitude.

To investigate more closely the distributions of robust bursting, figure 4.22 displays a zoom on the different distributions. This figure reveals multiple interesting behaviors that were not previously visible.

Figure 4.22a shows that the distribution of the dominant frequency of the spiking neuron controller has two peaks, whereas the other controllers only have one. This was not visible in figure 4.21 where they were both merged. This is interesting because the single neuron controller figure 4.13 displayed the same distribution but for the mixed controller. This reinforces the fact that these two types of feedback are quite similar and, in most cases, lead to similar performances.

Now looking at figure 4.22b shows that the distributions of the oscillation amplitude are more in line with the behavior of the single neuron controller displayed in figure 4.13. Both figures show that the sinusoidal controller has a distribution centered around a single peak, whereas the mixed and spiking neuron controllers show a distribution with two peaks separated by a space with no simulation displaying that amplitude.

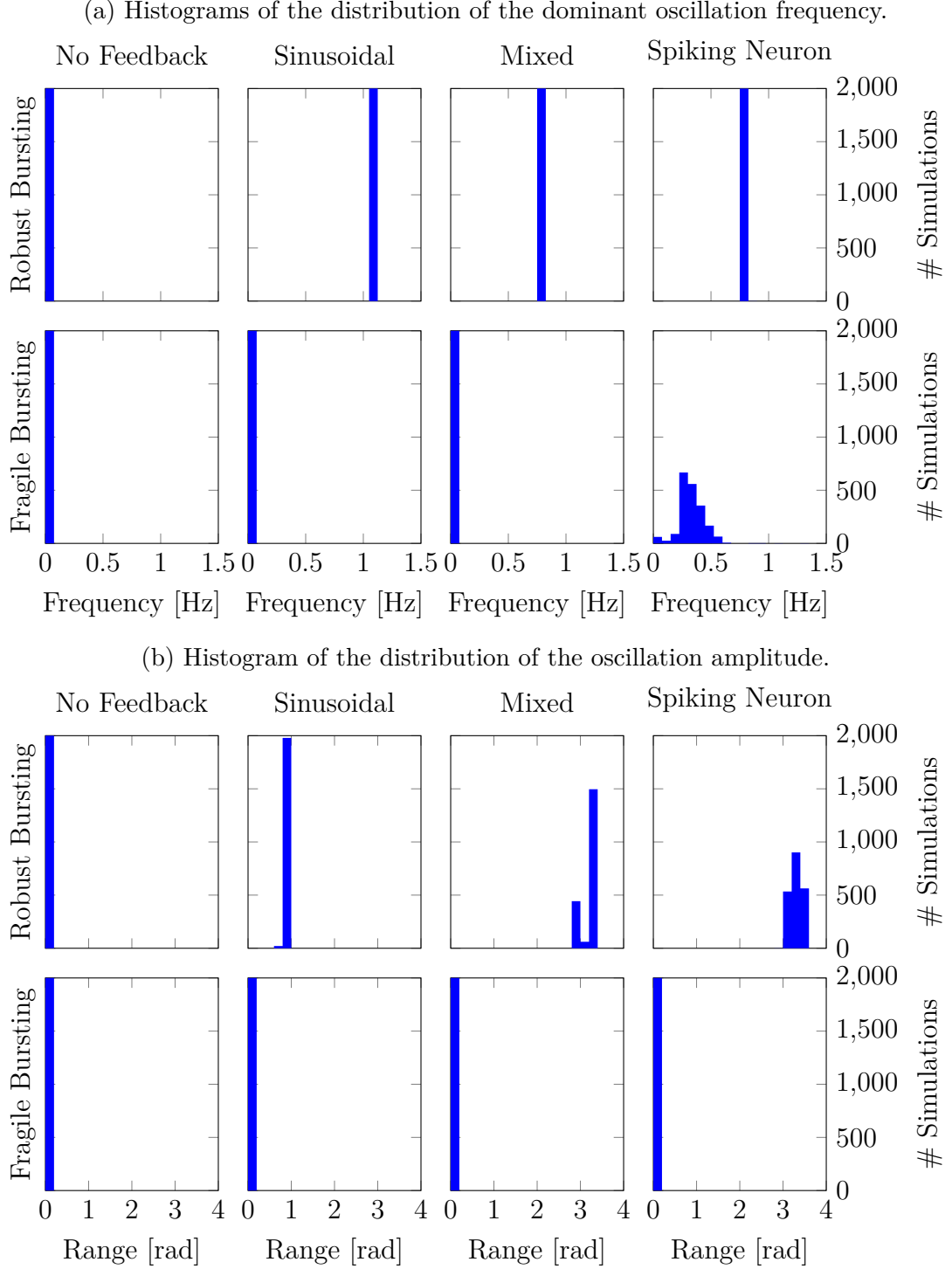


Figure 4.21: Comparison of the robustness of all feedback on the double-neuron controller–pendulum system using Monte Carlo analysis. The parameters of robust bursting were sampled from $I_{app} \sim \mathcal{N}(-2, 0.05^2)$ A, $g_{s-} \sim \mathcal{N}(-4, 0.03^2)$ S and $g_{u+} \sim \mathcal{N}(5, 0.05^2)$ S. The parameters of fragile bursting were sampled from $I_{app} \sim \mathcal{N}(0, 0.05^2)$ A, $g_{s-} \sim \mathcal{N}(-0.1, 0.03^2)$ S and $g_{u+} \sim \mathcal{N}(4, 0.05^2)$ S. Both neurons used $g_{f-} = -2$ S, $g_{s+} = 6$ S, $\tau_{max} = 10$ N m V $^{-1}$ and $K_{feed} = 5$ or $g_{syn} = 3$ S.

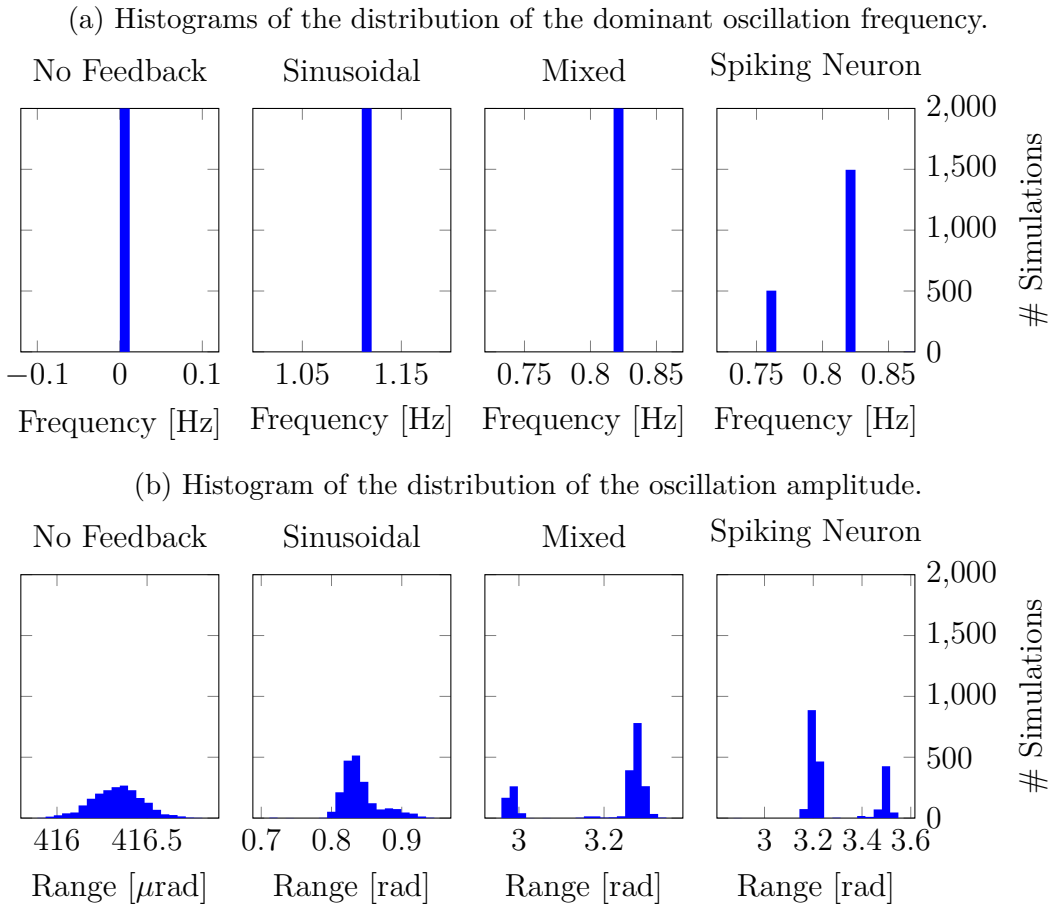


Figure 4.22: Comparison of the robustness of all feedback on the double-neuron controller–pendulum system using Monte Carlo analysis. The bursting parameters were sampled from $I_{\text{app}} \sim \mathcal{N}(-2, 0.05^2)$ A, $g_{s-} \sim \mathcal{N}(-4, 0.03^2)$ S and $g_{u+} \sim \mathcal{N}(5, 0.05^2)$ S. The bursting also used $g_{f-} = -2$ S, $g_{s+} = 6$ S, $\tau_{\max} = 10$ N m V $^{-1}$ and $K_{\text{feed}} = 5$ or $g_{\text{syn}} = 3$ S.

Chapter 5

Neuromodulation for adaptive amplitude control

The previous chapter explored the design of the controller to create a strongly connected sensorimotor system. However, the chapter never addressed or proposed any control strategy to allow the oscillation to reach a desired amplitude. This chapter introduces neuromodulation into the controller to automatically modify neuron parameters to reach a target amplitude.

5.1 Design of the controller

The goal is to generate a symmetric motion of the pendulum. Since section 4.4 defines a symmetric controller, it is natural to add neuromodulation to it. Chapter 4 established that $\tau_{\max} = 10 \text{ N m V}^{-1}$ was capable of reaching any amplitude. To control the bursting neurons the mixed feedback was chosen because it offered excellent performance in most situations and was less complex and computationally intensive than spiking neuron feedback. Because it proved to have better performance, the output gain $K_{\text{feed}} = 5$ is also used.

To control the amplitude of oscillation, the parameter g_{s-} was chosen since section 3.3.1 established that this parameter is linked to the power transmitted by a burst and figure 4.19 confirms that it correlates well with the oscillation frequency using mixed feedback.

Figure 5.1 displays the diagram of the model. This diagram shows the addition of two spiking neurons to figure 4.14. Their outputs are passed through saturation to produce a non-zero output only when spiking. The outputs of these neurons are then merged and fed through an integrator which is followed by a low-pass filter. Finally, the output of this filter provides the parameter g_{s-} .

The low-pass filter has a time constant of $\tau_m = 0.1 \text{ s}$ and the spiking neuron uses the following parameters.

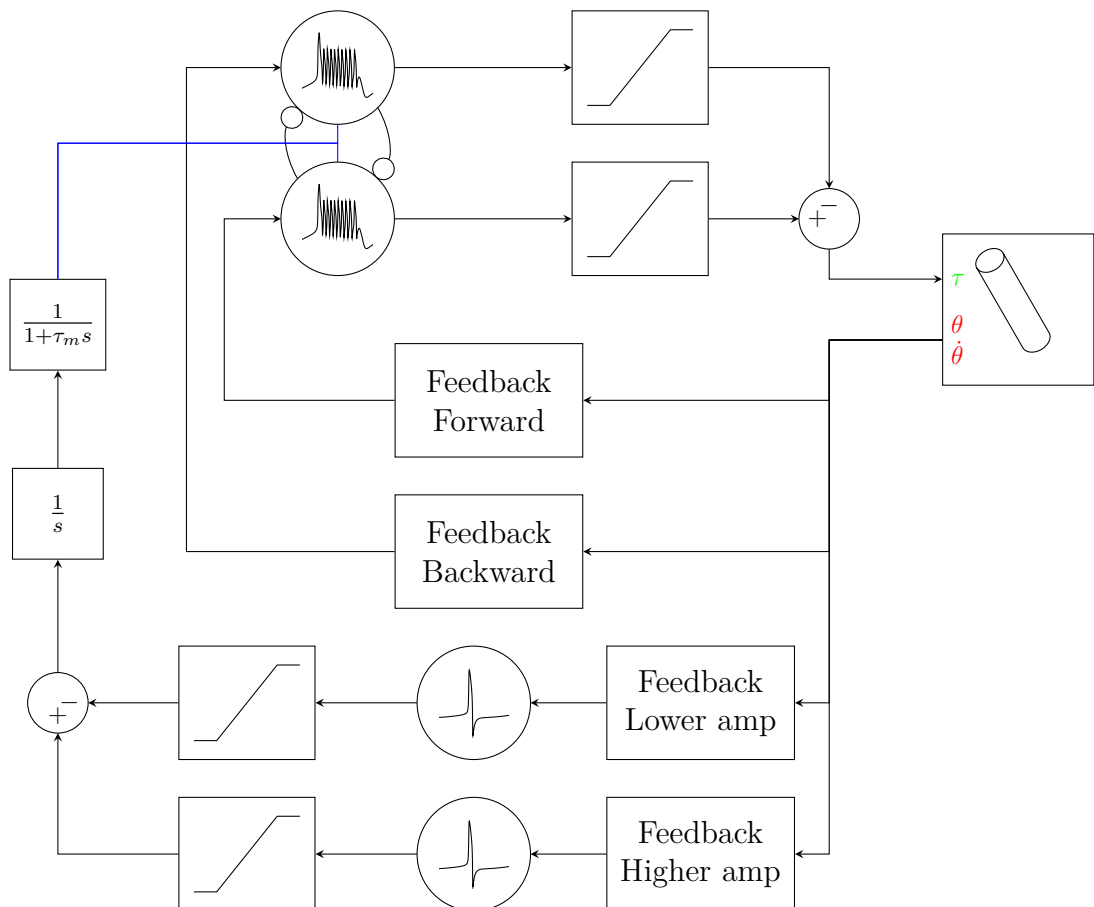


Figure 5.1: Diagram of the control loop of the controller with neuromodulation. The adder blocks also contain internal output gains θ_{\max} and $d g_s -$. Inhibitory synapses link the bursting neurons. Blue lines represent parameters and not input/output values.

$$\begin{array}{c|cc} g_{f-} & -2 \text{ S} & g_{u+} & 1 \text{ S} \\ g_{s+} & 4 \text{ S} & I_{\text{app}} & -0.5 \text{ A} \\ g_{s-} & -1 \text{ S} & & \end{array}$$

The idea of this architecture is to have the spiking increase or decrease the value of g_{s-} by steps through the integrator, and the low-pass filter is only there to smooth the value of the parameter and avoid weird neuronal behaviors due to steps in the parameters.

The feedback fed to the spiking neurons differs from the feedback fed to the bursting neurons. Figure 5.2 displays this new feedback architecture. This can be understood as a check of the amplitude at the peak of the oscillation. The goal is that one neuron will spike if the amplitude is too low and the other will spike if it is too high, leading to a change in the value of g_{s-} according to the expected result of this change looking at figures 3.7 and 3.8.

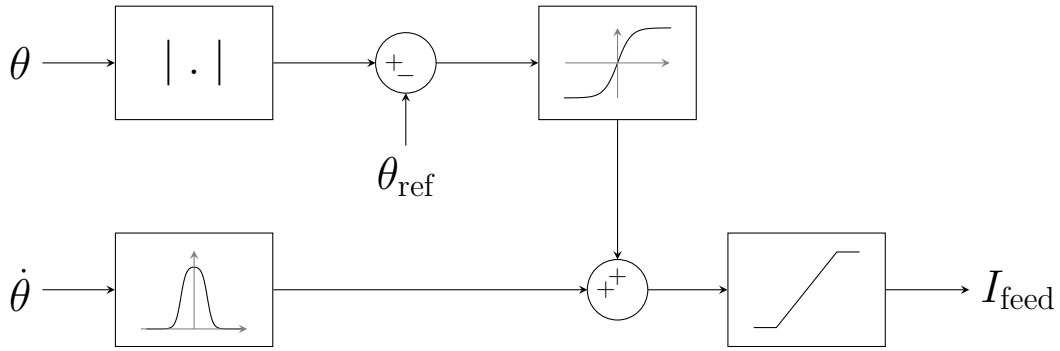


Figure 5.2: Diagram of the neuromodulation feedback.

$$I_\theta = \tanh(g_\theta (\alpha_{\text{side}} (|\theta| - \theta_{\text{ref}}) - d_{\text{buff}})) \quad (5.1)$$

$$I_{\dot{\theta}} = \frac{\tanh(g_{\dot{\theta}} (\dot{\theta} + d_{\text{bump}})) - \tanh(g_{\dot{\theta}} (\dot{\theta} - d_{\text{bump}}))}{2} - 1 \quad (5.2)$$

$$I_{\text{feed}} = K_{\text{feed}} \min(\max(0, I_\theta + I_{\dot{\theta}}), 1) \quad (5.3)$$

with $\alpha_{\text{side}} \in \{-1, 1\}$, $\theta \in [-\pi; \pi]$, $\theta_{\text{ref}} \in [0; \pi]$, g_θ and $d_{\text{buff}} \in \mathbb{R}$ and $g_{\dot{\theta}}$ and $d_{\text{bump}} > 0$.

α_{side} is a parameter relative to where the spiking neuron should be active. 1 signifies activation when the oscillation is above the desired angle and -1 indicates activation when it is below the desired angle. g_θ and $g_{\dot{\theta}}$ are parameter that define the sharpness of the transition of their respective tanh. d_{buff} is a term that offsets I_θ to create a buffer zone around the desired angle in which the neuron does not spike. d_{bump} defines the width of the bump around $\dot{\theta} = 0$. K_{feed} is the output gain of the feedback.

The exact value of those parameters as they are used is given below.

$$\begin{array}{c|cc} g_\theta & 40 \text{ A rad}^{-1} & g_{\dot{\theta}} & 20 \text{ A s rad}^{-1} \\ K_{\text{feed}} & 2 & d_{\text{bump}} & 0.1 \text{ rad s}^{-1} \end{array}$$

This feedback is similar to the mixed feedback defined in section 4.2.2 except that the sinus is replaced by the absolute value and the term θ_{ref} is added. This feedback creates a spike-like event when $\dot{\theta}$ is small and $\theta < \theta_{\text{ref}}$ or $\theta > \theta_{\text{ref}}$ depending on α_{side} .

To better understand the behavior of the system figures 5.3 and 5.4 represent the behavior of the system when the target requires a g_{s-} above or below the starting g_{s-} . The CPG with the sensory feedback controls the oscillation to keep it going at a rather set amplitude, and the value of g_{s-} is slowly tuned to reduce or increase the energy contained in a burst and shape the oscillation to the desired amplitude. These graphs also perfectly illustrate the behavior exhibited in section 3.3.1. The amplitude of the oscillation decreases in a step-like manner. These steps are caused by the disappearance of a spike in the burst, leading to less power being transmitted from the motor neuron.

5.2 Controller performance

This controller is designed to change the g_{s-} parameter in order to reach a certain desired amplitude θ_{ref} . A perfect controller would be able to make the oscillation amplitude reach a value very close to the target quickly and without oscillation around the target. This naturally leads to two very different criteria when measuring the performance of a specific set of parameters.

The first criterion, which can be called the static criterion, is the error between the desired amplitude and the amplitude reached at the steady state. If the steady state consists of an oscillation of multiple amplitudes, the mean at that steady state would be the ideal measure.

The second criterion, which can be called the dynamic criterion, concerns itself with the speed at which the controller can reach the desired amplitude. It can be measured in two ways. An easy way is to measure the time at which the amplitude crosses the desired amplitude. However, because the controller can undershoot the target, as seen in figure 5.3, another way to define it is as the time of the last change in the value of g_{s-} . As a good compromise, the relevant value will be the minimum between these two times.

To realize all analyses consistently, all tests include a stabilization period of 30 s where the target angle was $\theta_{\text{ref}} = \frac{\pi}{4} \text{ rad}$.

Figures 5.5 to 5.7 contain the data that will be useful for understanding the behavior of the neuromodulated controller. Figure 5.5 displays the evolution of metrics as a function of the desired angle θ_{ref} . Figure 5.6 displays the evolution of these metrics as a function of the neuromodulation gain dg_{s-} . Figure 5.7 contains the evolution of the amplitude mean and standard deviation as functions of the buffer zone d_{buff} .

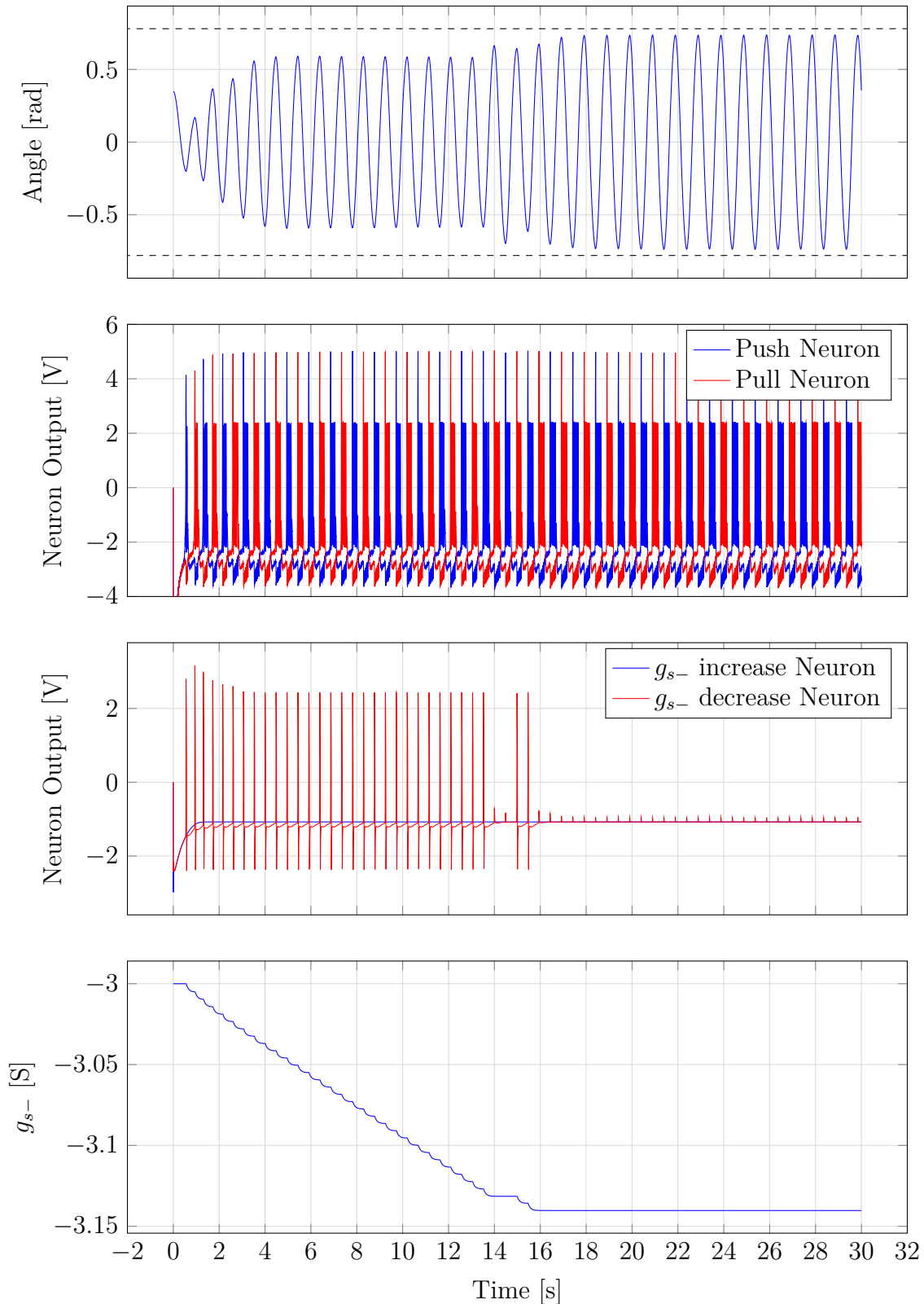


Figure 5.3: Oscillation of the neuromodulated controller–pendulum system when the initial steady-state oscillation amplitude is smaller than desired.

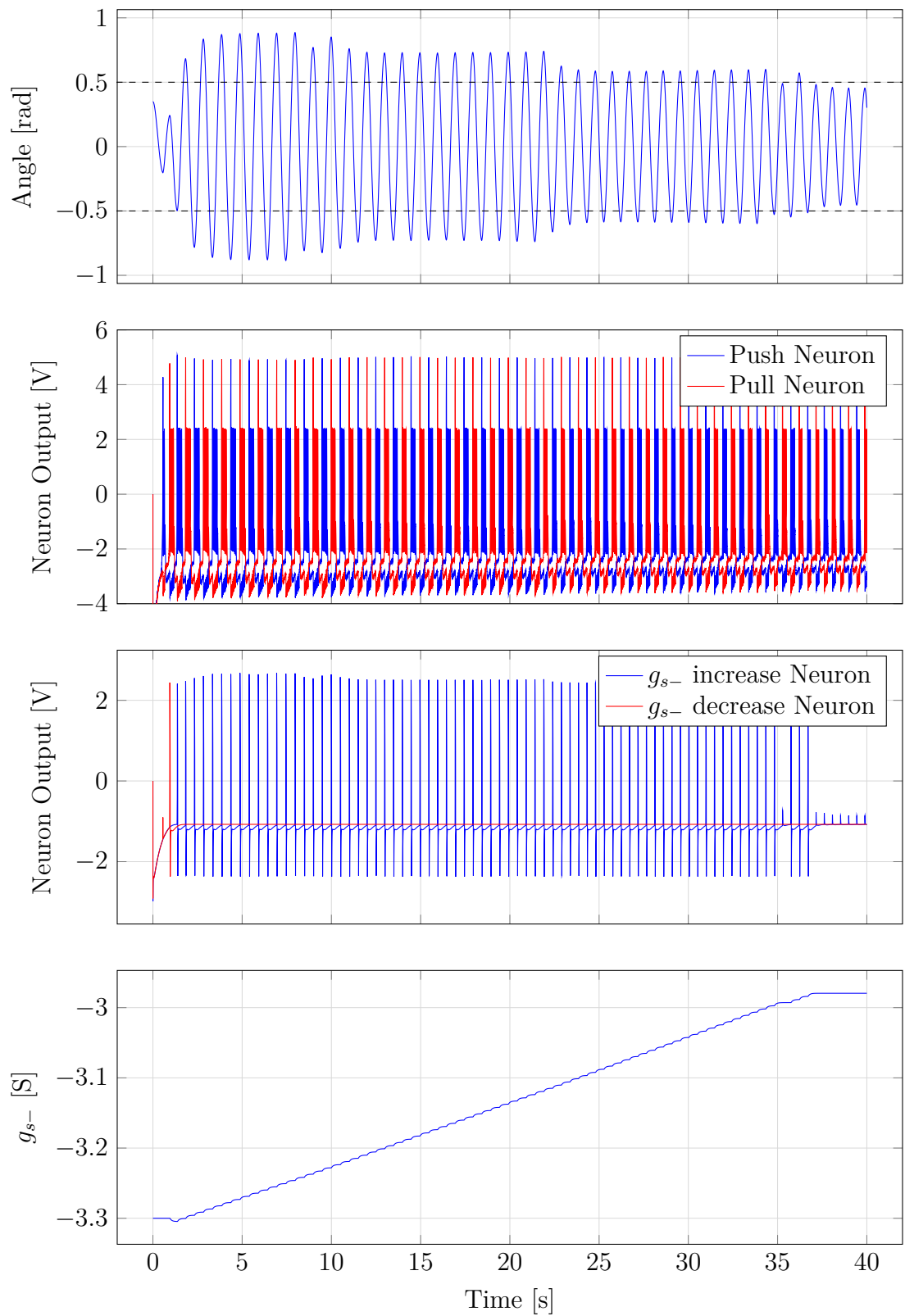


Figure 5.4: Oscillation of the neuromodulated controller-pendulum system when the initial steady-state oscillation amplitude is higher than desired.

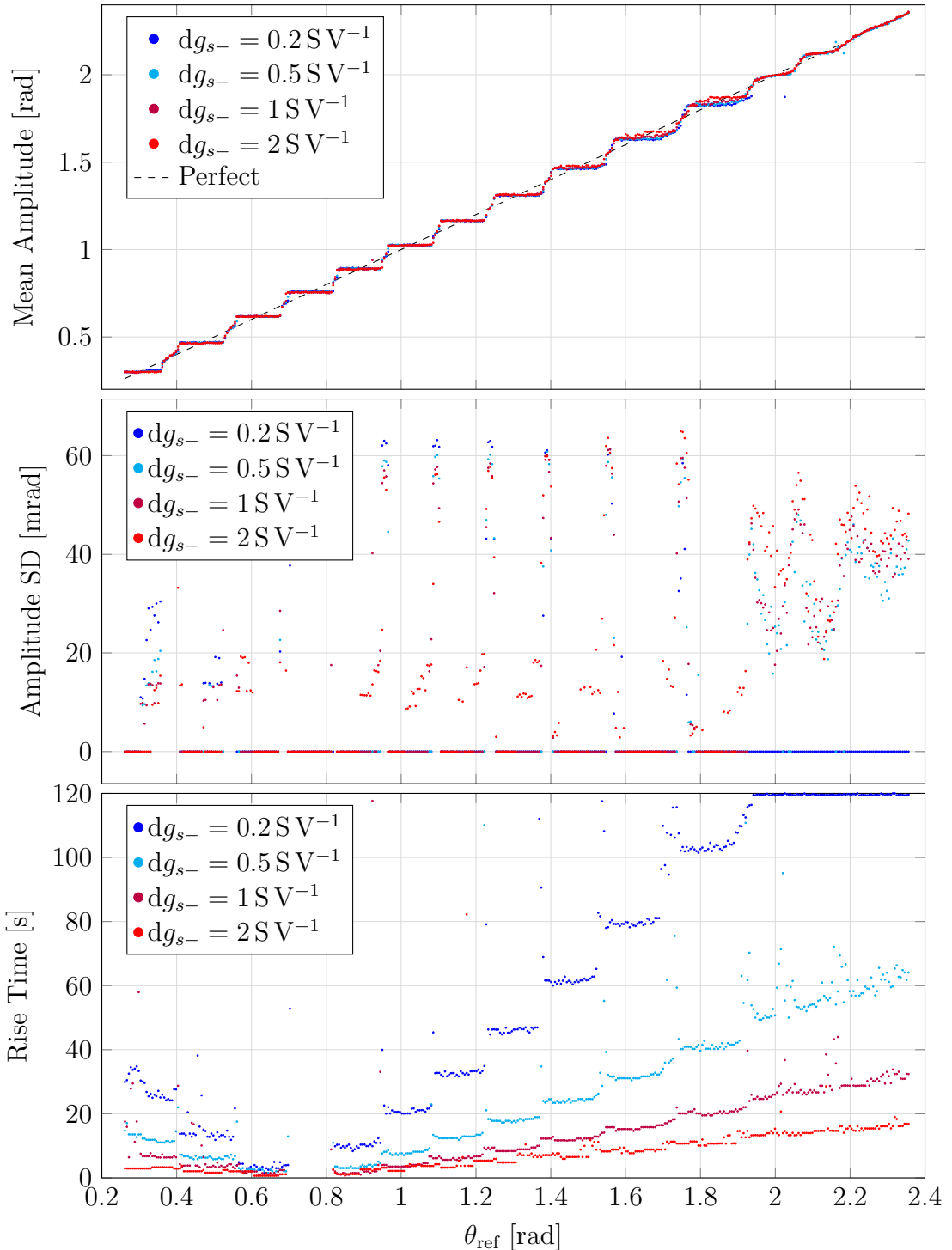


Figure 5.5: Evolution of performance metrics of the neuromodulated controller–pendulum system as a function of θ_{ref} at multiple neuromorphic gains $d g_{s-}$. With $d_{\text{buff}} = \frac{p_i}{60} \text{ rad}$.

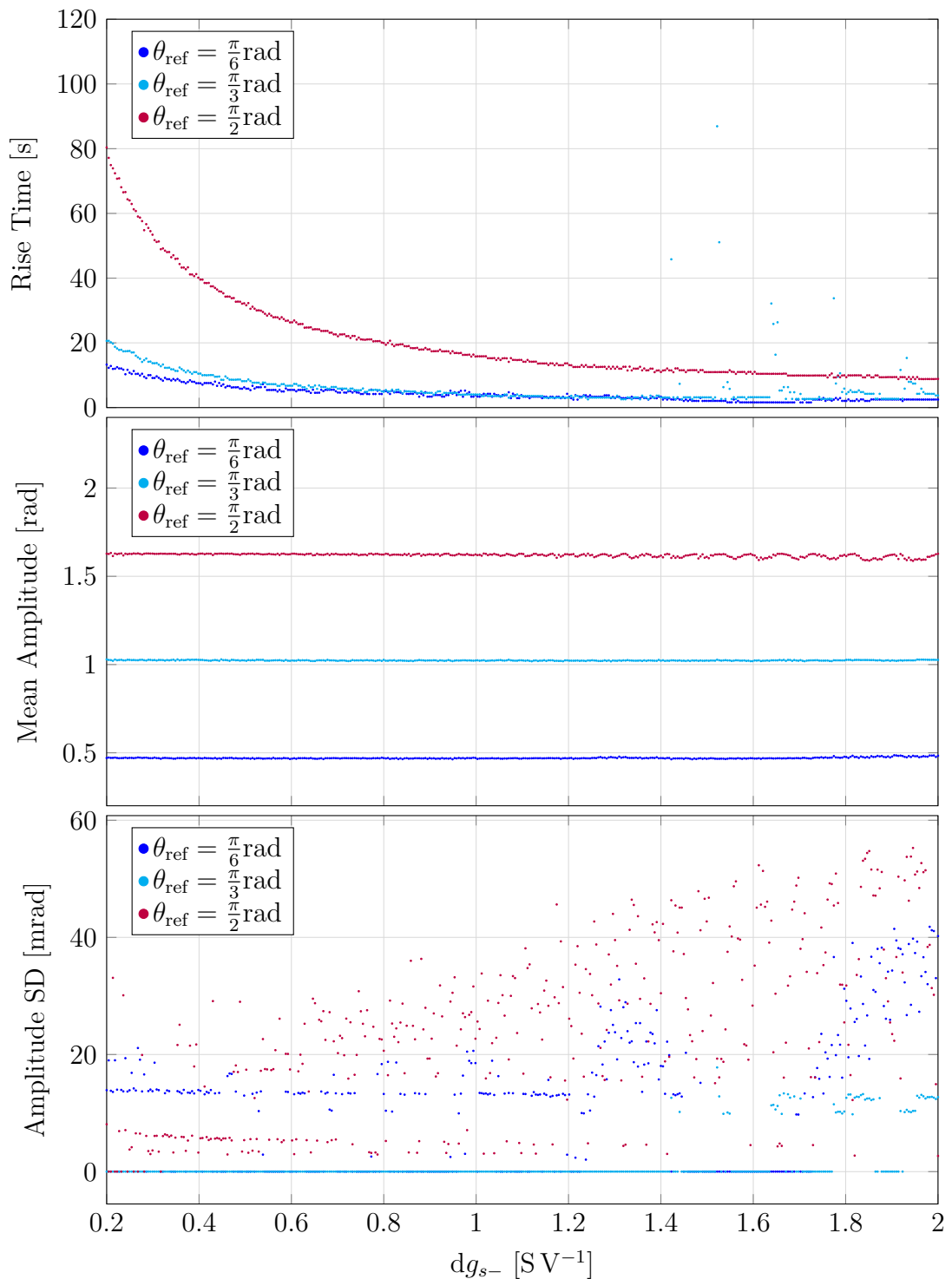


Figure 5.6: Evolution of performance metrics of the neuromodulated controller–pendulum system as a function of dg_{s-} at multiple desired amplitude θ_{ref} . With $d_{\text{buff}} = \frac{pi}{60}$ rad.

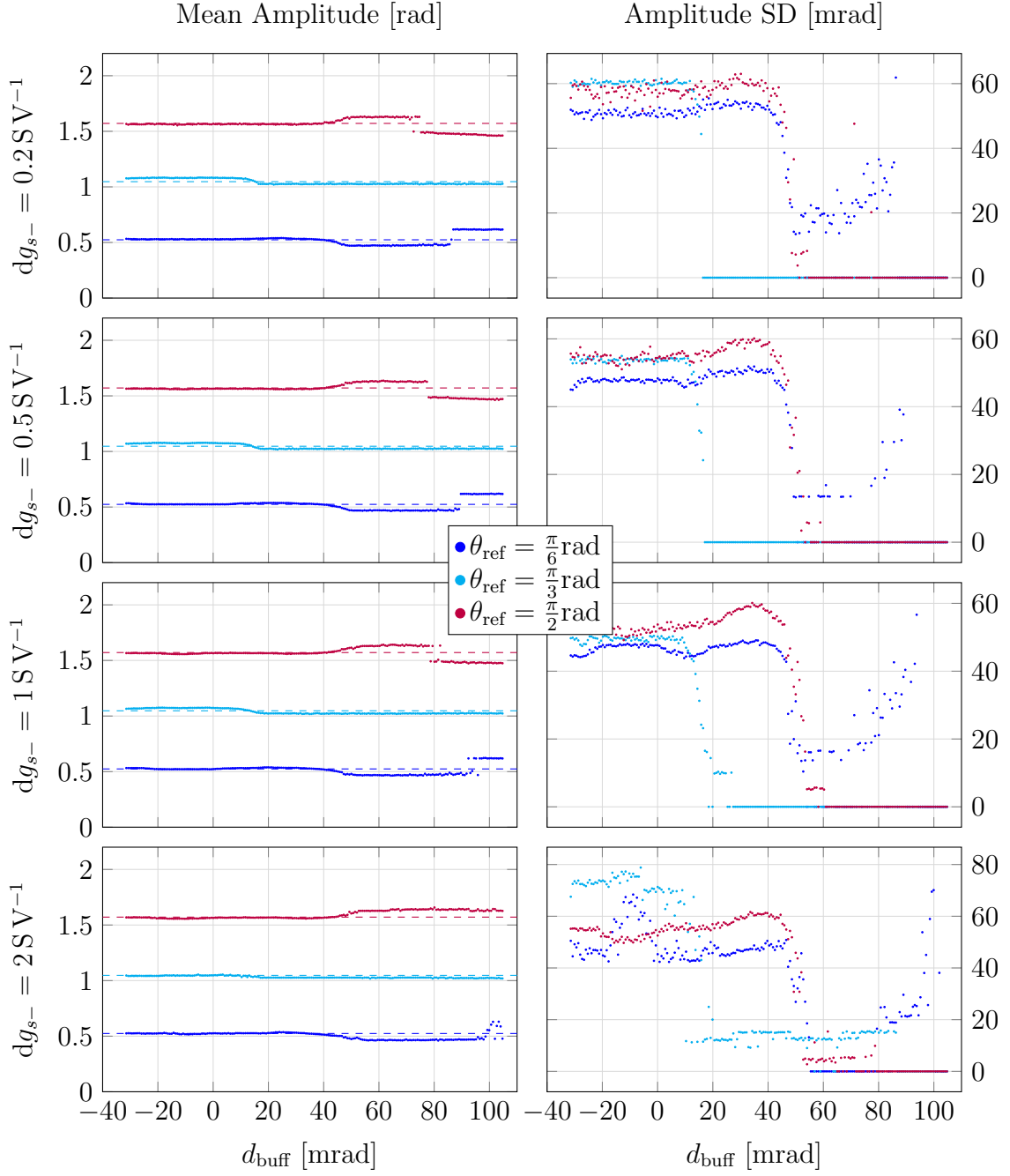


Figure 5.7: Evolution of performance metrics of the neuromodulated controller–pendulum system as a function of d_{buff} at multiple neuromorphic gains dg_{s-} and desired amplitude θ_{ref} . The rise time is not included.

5.2.1 Static

As defined above, the static performance of the controller is linked to its ability to get close to the desired amplitude.

Figure 5.5 contains the evolution of two useful metrics as a function of the desired angle θ_{ref} . The mean amplitude and standard deviation of the amplitude.

The first graph of this figure is the most important. For most of the graph, the effective amplitude as a function of the desired amplitude follows a step-like pattern. This is due to the effect seen in figures 3.7 and 3.8 which creates steps in the amount of energy a single burst can transmit.

However, this graph raises the question of how slopes can exist between these steps and at the end of the graph where the system is able to follow the target very well. The second graph, which displays the standard deviation of the amplitude of the oscillations after reaching steady states, answers this question. This shows that these behaviors only occur when there is a variation in the amplitude. Thus, they are created by fluctuations in the oscillation amplitude around the desired amplitude θ_{ref} . The behavior when high θ_{ref} particularly is quite impressive. A simple modulation control that was designed to reach a steady state when denied this possible state can precisely follow the target amplitude in the mean. This shows the adaptability of such a control scheme to operate in non-ideal circumstances.

Figure 5.7 gives another view of the reach of the desired amplitude. This shows that the value that determines whether the system stabilizes or not is the value of d_{buff} . This is logical because the value defines the buffer zone around the desired amplitude. The graphs of the amplitude standard deviation clearly show that for low d_{buff} the system never reaches equilibrium, but the graph of the amplitude means shows that it manages to follow the desired amplitude in the mean. An interesting behavior is observed when looking at the trace of $\theta_{\text{ref}} = \frac{\pi}{2}\text{rad}$ for $dg_{s-} = 0.2\text{ SV}^{-1}$. For this trace, the amplitude first stabilizes at some values; however, as d_{buff} increases, it jumps to a new value. The new value is worse than the first value because it is farther away from the desired amplitude. The explanation for this behavior is simple. When d_{buff} is large enough, multiple levels of amplitude do not trigger neuromodulation. Thus, the system will stabilize at the amplitude closest to its starting position. Since the simulation was made starting from an amplitude of $\theta = \frac{\pi}{4}\text{rad}$ the lowest level admissible for $\theta_{\text{ref}} = \frac{\pi}{2}\text{rad}$ is reached and not the higher one that exhibits better performance. This is because being below $\frac{\pi}{2}\text{rad}$ is closer to $\frac{\pi}{4}\text{rad}$.

Figure 5.6 also gives us other useful information. In particular, the graph of the mean amplitude displays an interesting behavior. As the neuromodulation gain dg_{s-} increases the mean amplitude becomes less stable. This is particularly visible for $\theta_{\text{ref}} = \frac{\pi}{2}\text{rad}$ where at higher θ_{ref} the amplitude oscillates around the reference. The graph of the standard deviation of the amplitude shows that the deviation increases with dg_{s-} . This means that as dg_{s-} increases the range of fluctuations in amplitude increases. This leads to oscillation in the mean, possibly because the simulation time is limited to 120 second and a greater range of fluctuation means a longer cycle of amplitudes.

5.2.2 Dynamic

As defined previously, the dynamic performance of the controller is defined by the speed at which the controller approaches the desired amplitude.

Figure 5.6 first graph is very interesting for discussing dynamic performances. It displays the evolution of the rise time as a function of the neuromodulation gain dg_{s-} . Since dg_{s-} controls the amount to which a spike changes the value of g_{s-} , it is natural that it will be linked to the rise time. The graph clearly shows that higher dg_{s-} lead to lower rise times. However, the gains diminish because they follow a decreasing exponential law. Indeed, theoretically doubling dg_{s-} should result in halving the rise time because the speed at which g_{s-} is moved doubles; thus, the ideal g_{s-} should be reached twice as fast. This is verified nicely on the graph for $\theta_{ref} = \frac{\pi}{2}$ radian since at the start when $dg_{s-} = 0.2 \text{ SV}^{-1}$ the rise time is around 80 s and doubling dg_{s-} to 0.4 SV^{-1} decreases the rise time to around 40 s. This is also observed for dg_{s-} set to 0.8 SV^{-1} with a rise time of around 20 s and 1.6 SV^{-1} with a rise time of around 10 s. However, this law has a limit, as shown in the graphs for $\theta_{ref} = \frac{\pi}{3}$ radian and $\theta_{ref} = \frac{\pi}{6}$ radian since they both converge to a similar value. This implies a certain minimum rise time.

In Figure 5.5, the graph of the rise time as a function of θ_{ref} is quite interesting. Similar to what was observed in the static performance analysis, the rise time seems to progress in steps that progress at the same rate as the steps of the mean amplitude. This is logical because the rise time can be understood as the time taken to find a g_{s-} that generates acceptable oscillations. However, because the change in the power of a burst as a function of g_{s-} moves in a stepwise manner. The desired g_{s-} also moves in steps. This means that two θ_{ref} that need a similar g_{s-} will have the same rise time because they require the same underlying g_{s-} .

Finally, although not explicitly shown, computing figure 5.6 proved that the value d_{buff} has little effect on the rise time. Only when very high can it allow the system to stabilize at an amplitude closer to the starting amplitude, leading to a lower rise time. However, it is not reliable nor a desirable way of accelerating convergence.

5.2.3 Static-Dynamic performance Trade-off

The analysis of the static and dynamic performance revealed a large trade-off between the two.

This can be seen in figures 5.5 and 5.6 where higher rise times lead to better static performances, whereas lower rise times lead to poor static performances. This is visible especially in figure 5.6 where the decrease in rise time in the first graph leads to fluctuations in the mean value in the second graph and a higher standard deviation.

This trade-off is primarily embodied by the value of dg_{s-} . As stated before, increasing this value leads to better dynamic performance because a single spike will change the value of g_{s-} more. However, it comes at the cost of static performance because increasing the number of steps a spike makes in g_{s-} can lead to fluctuation

around the desired state, which skips over the good value of g_{s-} . It also takes some time for the system to settle to the new steady state when g_{s-} changes.

On the other hand, a smaller dg_{s-} leads to a much slower change of g_{s-} thus avoiding skipping the good value, but it increases the time it takes to reach this good value.

From figure 5.6, a good range of values is $dg_{s-} \in [0.5; 1] \text{ SV}^{-1}$. Below this range, the slower movement is not justified by any static performance gain, whereas higher than that is subject to fluctuations and does not have large gains in rise time.

Also, figure 5.7 shows that the value of d_{buff} creates another trade-off. A large value facilitates system convergence because it allows more leeway in the error between the current and desired amplitudes. However, a value that is too large will result in the system not stabilizing at the amplitude level closest to the desired amplitude. This means that the performance of the controller is negatively affected by a large d_{buff} . Conversely, lower values of d_{buff} make it impossible for the system to stabilize because no amplitude level is close enough to not activate the sensory neurons. Figure 5.7 indicates that $d_{\text{buff}} \in [50, 70] \text{ mrad}$ is a good range to ensure convergence and not stabilize too far from the desired amplitude. Therefore, the value $\frac{\pi}{60} \text{ rad} = 52.36 \text{ mrad}$ that was used until now is a good trade-off.

Figure 5.8 displays a system using the $dg_{s-} = 0.5 \text{ SV}^{-1}$ as a good compromise. This shows that it can mostly follow the desired shape of oscillation with a certain time shift. Another nice thing is that the desired oscillation goes from $\frac{\pi}{6} \text{ rad}$ to $\frac{2\pi}{3} \text{ rad}$. This proves that neuromodulation is very effective in controlling the amplitude of the oscillation of the pendulum because it can span a large range of amplitudes.

5.3 Robustness analysis

Having shown the capabilities of the controller, the next step is to determine how sensitive it is to changes in the parameters. Figure 5.9 presents the distribution of the different metrics when the parameters of the motor and sensory neurons are drawn from Gaussian distributions.

The most important value is the tracking of the mean oscillation amplitude because controlling this value is the goal of neuromodulation. Fortunately, the figure shows that the average amplitude always stays close to the desired amplitude. In addition, the spread of amplitude does not seem to correlate with either the neuromorphic gains dg_{s-} nor the desired amplitude θ_{ref} . Furthermore looking at the standard deviation of the amplitude shows that the amplitude of oscillation converges for at least 75 % of the simulations. This shows that the value of amplitude are not means that do not represent the behavior fully but sustained amplitudes.

On another note, looking at the rise time again shows the very clear relationship it has with dg_{s-} . This is seen very well with $\theta_{\text{ref}} = \frac{\pi}{2} \text{ rad}$ where doubling dg_{s-} divides the convergence time by two.

Overall, this analysis shows that the controller design described in this chapter is quite resilient to variations. This proves that its structure is sound and that the

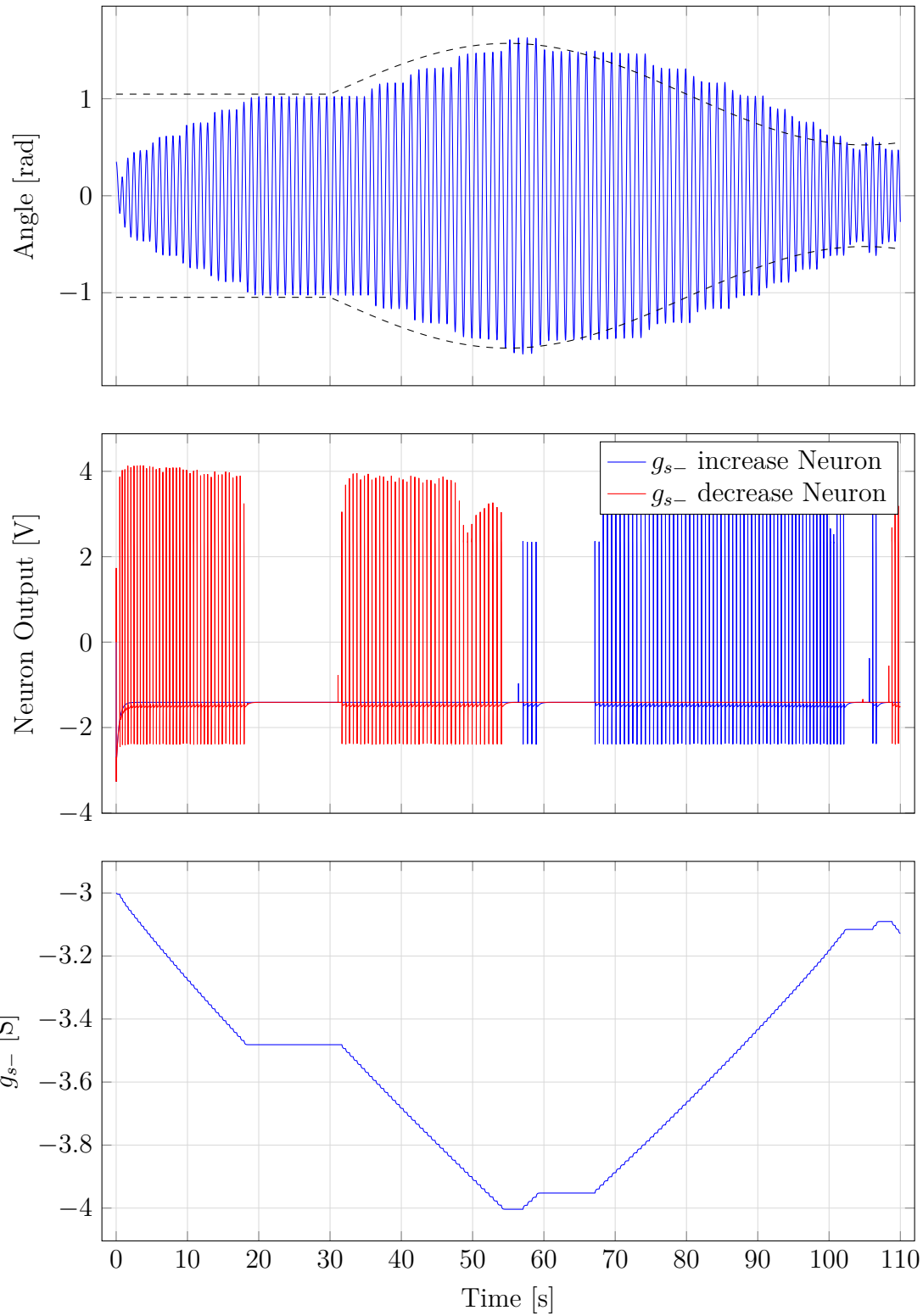


Figure 5.8: Behavior of the neuromodulated controller–pendulum system with $dg_{s-} = 0.5 \text{ SV}^{-1}$ and $d_{\text{buff}} = \frac{\pi}{60} \text{ rad}$ when subject to a varying desired amplitude θ_{ref} .

performances discussed earlier are not flukes.

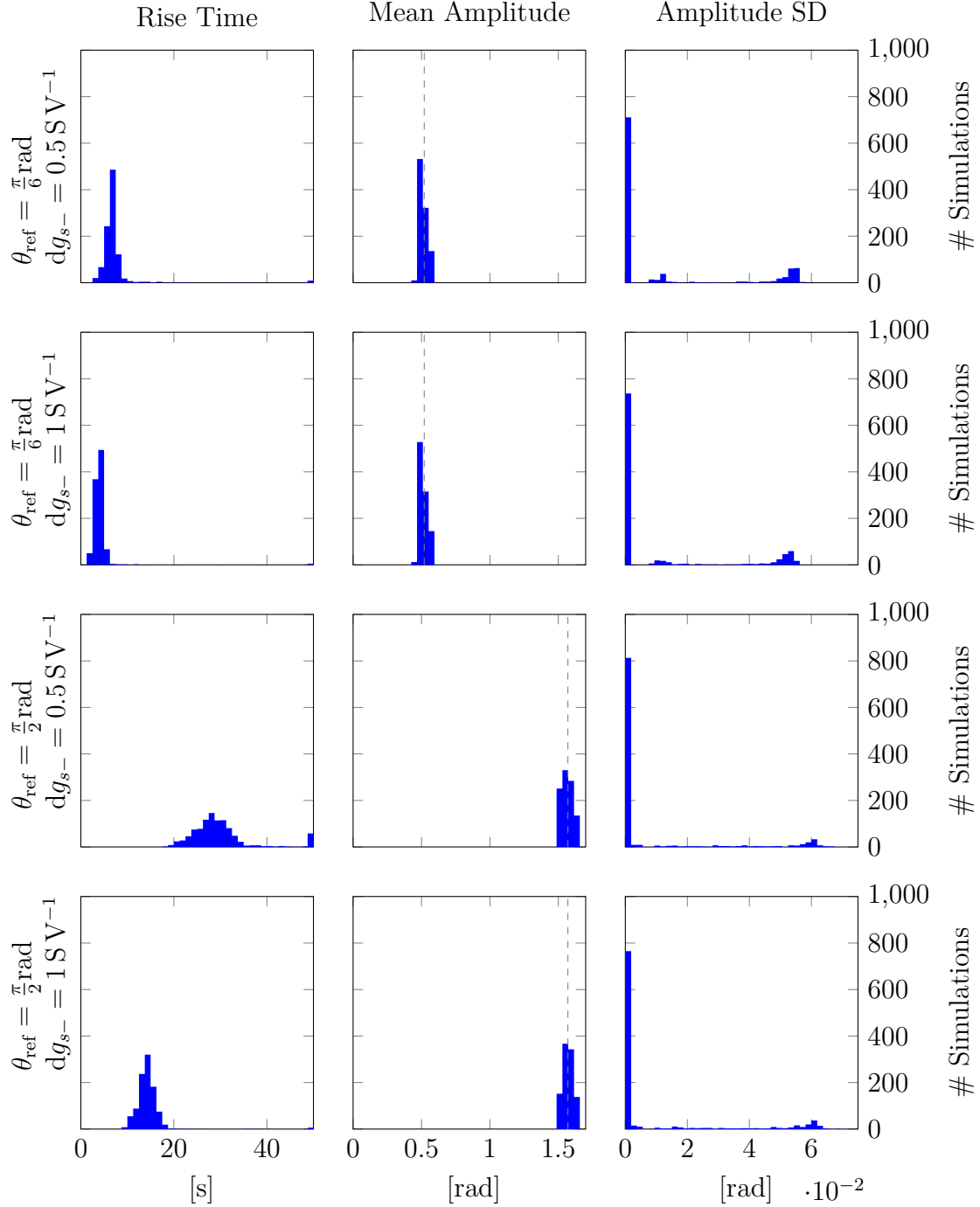


Figure 5.9: Monte Carlo analysis of the robustness of the neuromodulated controller–pendulum system to changes in the parameters of neurons. The parameters of the motor and sensing neurons as well as the parameters of the neuromodulated feedback were drawn from $\mathcal{N}(\mu, 0.03^2)$ A with μ the normal value of the parameter. All simulations started from a stable equilibrium around $\theta = \frac{\pi}{4}$ rad and used $d_{\text{buff}} = \frac{\pi}{60}$ rad.

Chapter 6

Simple interconnection of controller-pendulum systems

The previous chapters discussed the design of a controller for a single pendulum system. However, control systems are rarely used in isolation but often need to be synchronized. Thus, a point of interest is to determine whether it is possible to interconnect multiple controller-pendulum systems to generate specific spatiotemporal patterns. The neuromorphic approach of the controller should facilitate this goal because interconnecting controllers only involves creating synapses between certain neurons. This chapter will serve as a proof of feasibility and will only explore a single interconnection scheme of two pendulums.

6.1 Nature of the interconnection

The goal of this chapter is to manage the interconnection of multiple controllers. To prove the feasibility of this concept, the simplest interconnection is chosen. The system will be composed of two interconnected controllers, and the goal is to achieve phase opposition between the pendulums. This is similar to an HCO in a purely neuronal network.

The only way to interconnect neurons defined to this point is through synapses. This type of connection is sufficient to interconnect multiple controllers and achieve the desired spatiotemporal pattern. To generate this pattern, the easiest approach is to use the HCO structure between the corresponding motor neurons in both controllers. This pushes the neurons to work in opposition, thus achieving the desired pattern. Figure 6.1 represents the use of synapses proposed to reach the phase opposition between pendulums. It clearly shows the interconnection between the corresponding motor neurons in the controllers. In addition, the control of a pendulum remains mostly local, and the state of one pendulum does not directly affect the motor neurons of the other controller. The link between the pendulums is realized only at the neuronal level.

The realization of the opposition will be harder than in an HCO because each controller is strongly linked with its pendulum, which has inertia. This means that

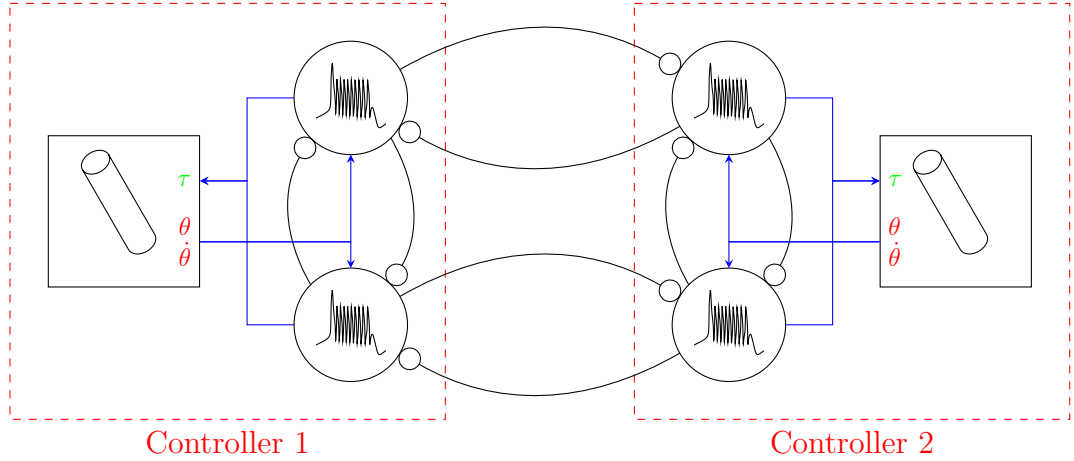


Figure 6.1: Diagram of the interconnection of the controllers. For simplicity and generality, only the motor neurons and mechanical system are represented for each controller-pendulum system.

the system may settle near perfect opposition but never achieve it because the control of the oscillation will become far more prevalent than the effect of the synapses.

The addition of new synapses leads to a change in the conductance defined in chapter 4. For intra-controller synapses g_{syn} becomes equal to -0.8 S and for inter-controller synapses $g_{\text{syn}} = -0.2 \text{ S}$. This results in similar behavior if the pendulums are in phase opposition.

6.2 Non-neuromodulated system

The first step in testing the interconnection model is to find if it works when the controllers have static dynamics. Thus, the model defined at the end of chapter 4 is reused. The goal is to simulate two copies of the controller-pendulum system in the configuration of figure 6.1 to generate the desired spatiotemporal pattern with the pendulums.

Simulations of this test can be found in figure 6.2. The figure shows that the interconnection successfully generates the pattern. The zoom indicates that the difference with a perfect opposition of phase is very small because the plot of the angles cross very close to 0. The pattern seems to have taken 15 s to 20 s to establish itself. At first, the oscillations of both pendulums were in phase because both started with the same initial conditions. The separation of the oscillation occurred gradually. This is a good result because it indicates that the local control of the pendulum outweighed the realization of the pattern. Interestingly enough around 15 s the interaction between the controllers seemed to generate the highest perturbations, and then abruptly, the quasi-steady state is established.

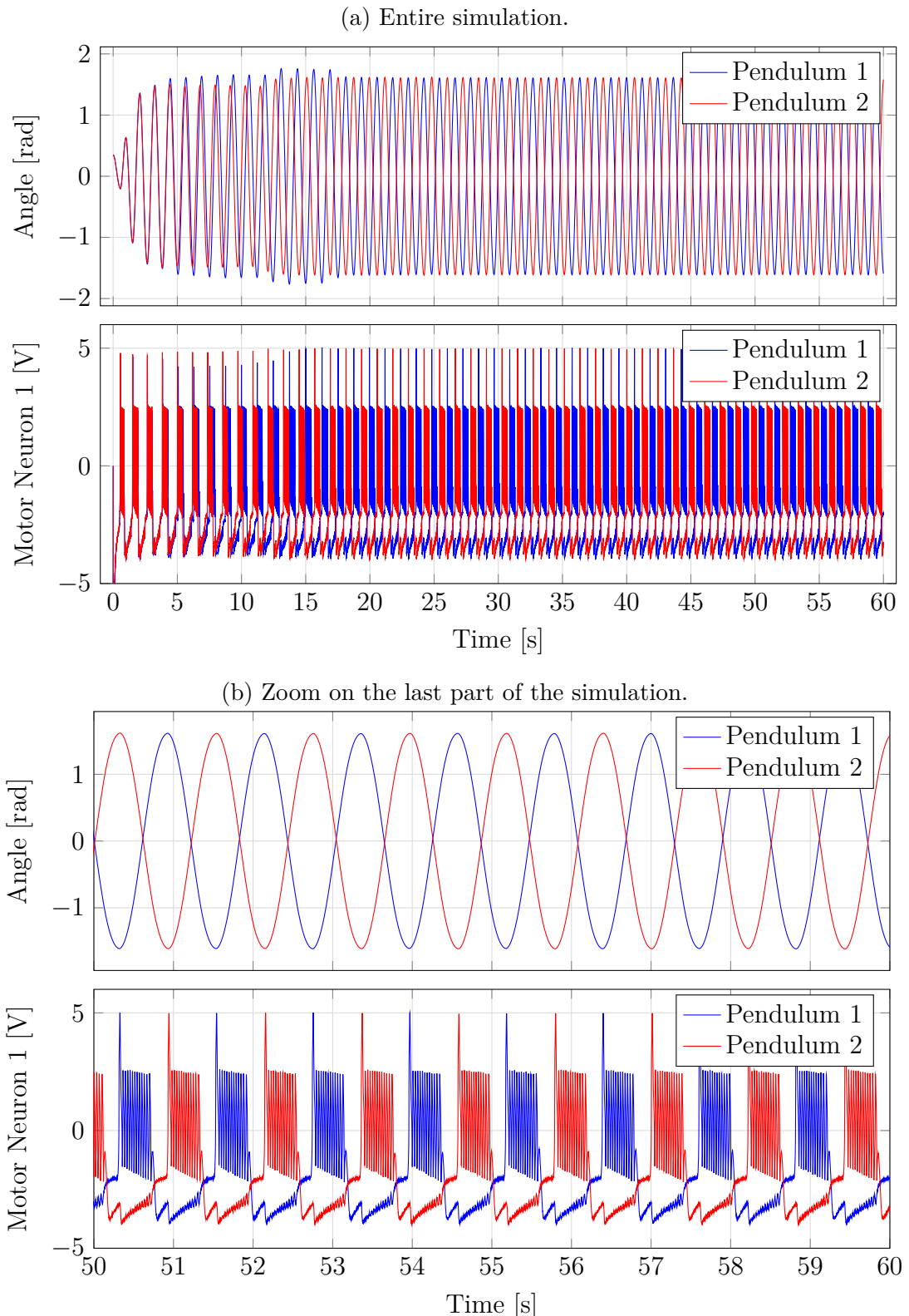


Figure 6.2: Simulation of interconnection using a controller without neuromodulation.

6.3 Independently neuromodulated system

The previous section shows that interconnecting controllers is possible for controllers with static parameters. The next step is to reintroduce neuromodulation to allow amplitude control. Because the oscillation frequency depends on the amplitude, the target amplitude should be the same for both controllers. Otherwise, opposing two signals with different frequencies is impossible to achieve well. The challenge lies in the mismatch between the values of g_{s-} for both controllers. To avoid conflict between disturbances linked to the realization of the opposition of phase and neuromodulation, the value of the neuromorphic gain $d g_{s-}$ is lowered to $d g_{s-} = 0.1 \text{ S V}^{-1}$. This limits the speed of neuromodulation and allows time for the network to stabilize.

Figure 6.3 contains the simulation of the interconnected neuromodulated controller. It is clear that the system manages to find a steady state in which the values of g_{s-} for both controllers remain very close. Looking at the zoom at the end of the simulation, the phase opposition of the pendulum is clearly realized but seems less perfect than in the not neuromodulated case. However, the smaller value of g_{s-} in this cases likely plays a role in the difference in behavior. A smaller burst length may render opposition more difficult. Finally, independent neuromodulation setting g_{s-} to different values for each controller may also prevent perfect opposition due to a break in symmetry.

Looking at the entire simulation, it is interesting to see that phase opposition is present during neuromodulation. This shows that the desired spatiotemporal relationship is compatible with the amplitude control.

6.4 Globally neuromodulated system

The previous section showed that coupling controllers with neuromodulation was somewhat more difficult. This may be due to neuromodulation breaking the symmetry between the controllers. Indeed, the motor neurons of both controllers end up with different g_{s-} values leading to a potentially more difficult control.

It then becomes quite interesting to observe the effect of restoring this symmetry by forcing a global g_{s-} value. To achieve this, the outputs of the four sensory neurons are fed to the same integrator, and the resulting g_{s-} is applied to the four motor neurons. This amounts to the same neuromodulation loop but on a global scale. Obviously, keeping the independent g_{s-} would be better because pooling them destroys the capacity of local control. Nevertheless, possible improvements in performance from this change must be studied.

Figure 6.4 displays the simulation of the system with global neuromodulation. Compared with local neuromodulation, the first difference is the rise time of g_{s-} which is faster because the integrator combines the changes of two sets of sensory neurons. Looking at the zoom at the end of the simulation, it appears that pooling the g_{s-} did not improve the opposition. This indicates that this imperfection lies deeper in the model rather than being caused by a slight break in symmetry. There

is a lone jump in g_{s-} near the end, but it is probably due to a random fluctuation.

The simulation points toward the pooling of g_{s-} being unnecessary. This is nice because it means that forfeiting the local control does not yield significant performance improvements. This agrees with neuromorphic principles.

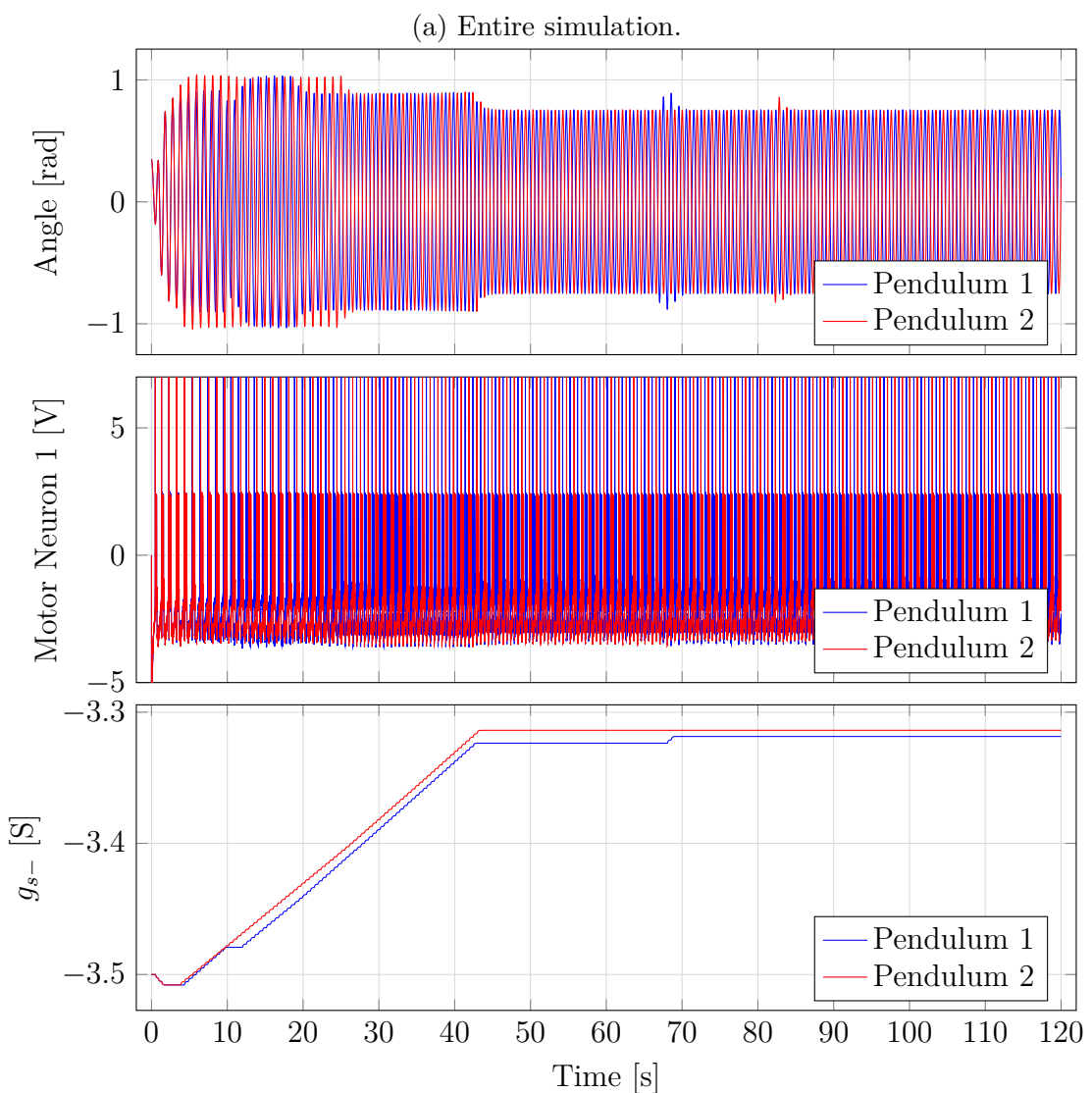


Figure 6.3: Simulation of interconnection using a controller with local neuromodulation.

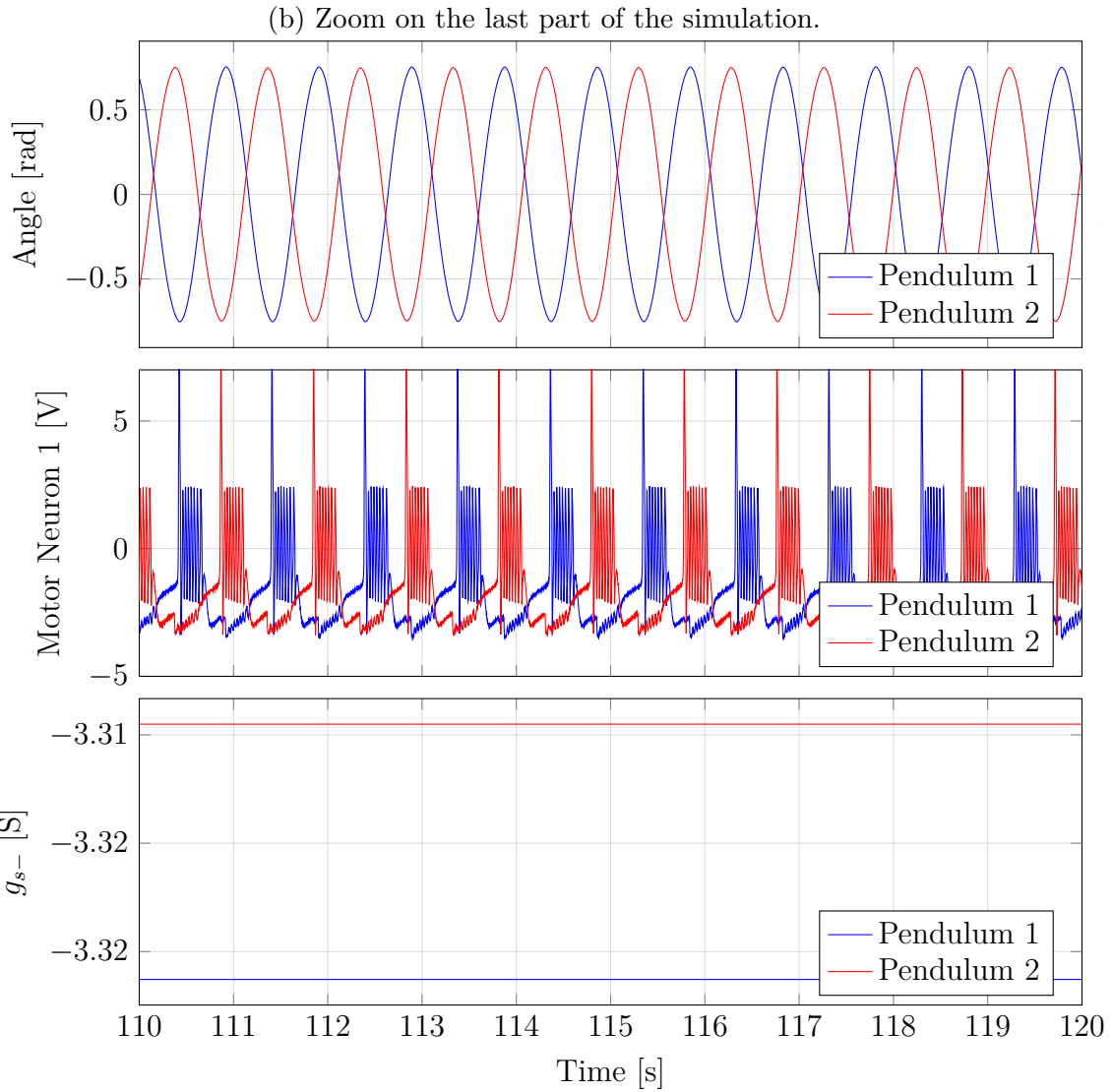


Figure 6.3: Simulation of the interconnection using a controller with local neuromodulation. (cont.)

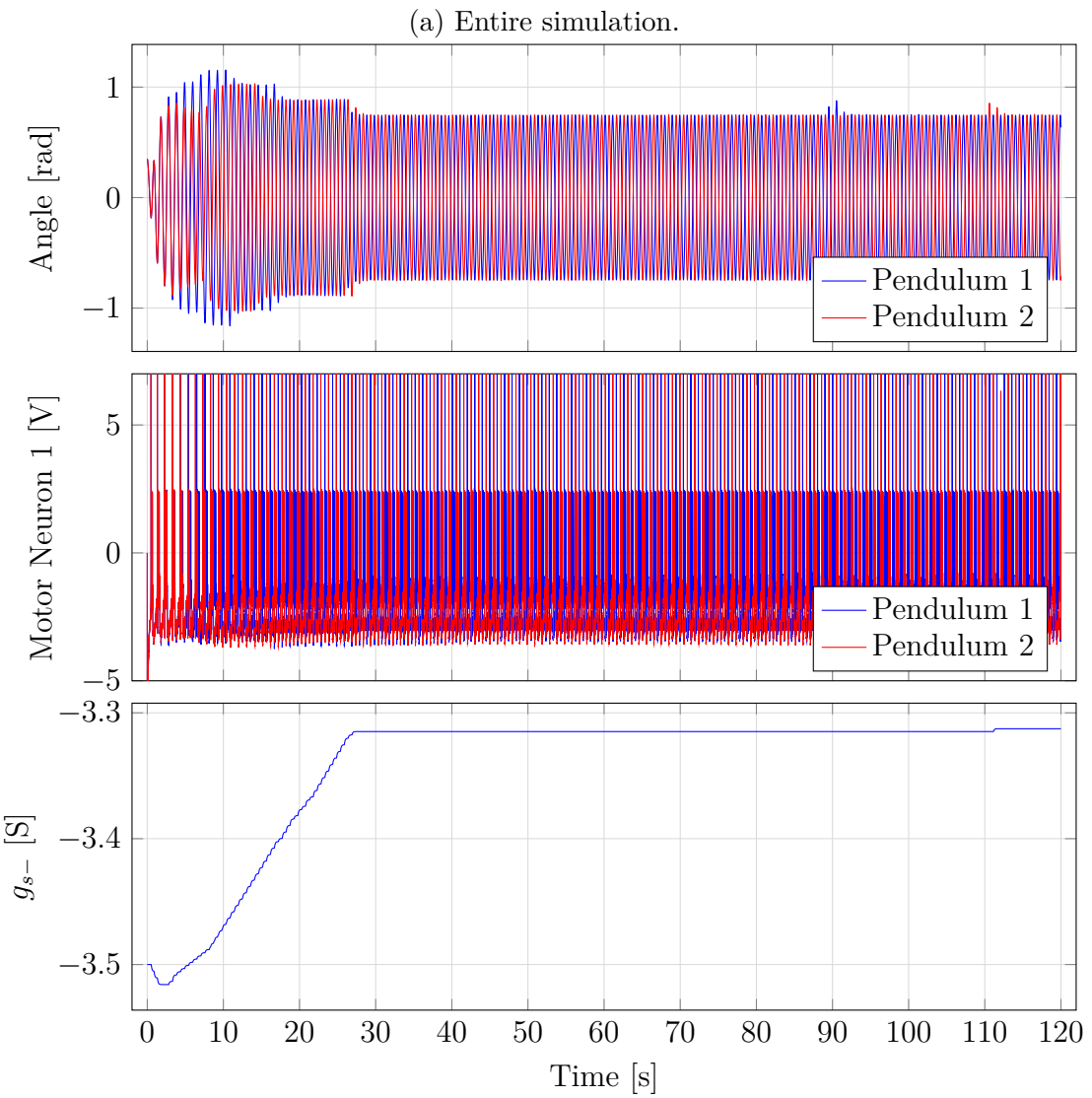


Figure 6.4: Simulation of the interconnection using a controller with global neuro-modulation.

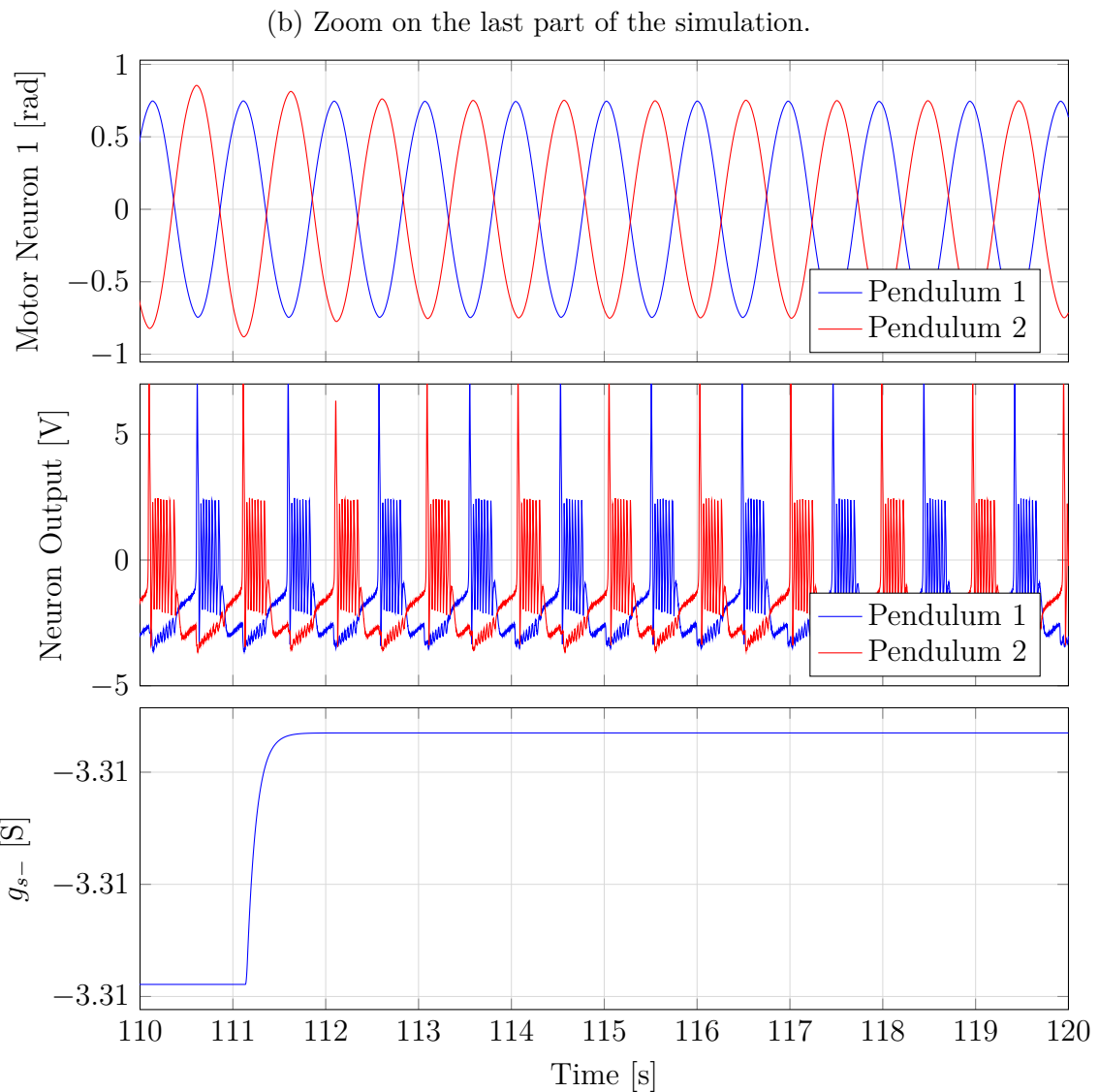


Figure 6.4: Simulation of interconnection using a controller with global neuromodulation. (cont.)

Chapter 7

Conclusion

Coming from biology, this thesis proposes a controller that can control a pendulum to generate oscillations at a given amplitude. This work began with the definition of a neuronal model capable of performing the most common neuronal behaviors, i.e., spiking and bursting. The analysis of this model highlighted the distinct effect of certain parameters on certain metrics. Building on this understanding of neuronal behavior, a single-neuron controller was built and tested using multiple sensory feedback and showed great performance. The model was modified to add a second motor neuron, and both neurons were connected to form a half-center oscillator capable of symmetrical oscillation. Finally, the model was extended once again to add neuromodulation of the parameters of the neuron to control the oscillation amplitude. This led to an analysis to find a good compromise between the speed of the control and its precision.

The final controller was tested and showed that it could follow a dynamic target amplitude relatively quickly. Yet, the controller shines in its way of changing the amplitude, it never requires forcing the pendulum to swing lower by activating earlier. Rather, it organically changes the amplitude by modulating the energy transmitted while keeping the actuation near the optimal timing. In addition to this, a proof of the possibility of interconnection was made in the design of a simple network of pendulums to achieve a given spatiotemporal pattern.

This controller is an interesting addition to the field of control. Its reliance on excitable systems distinguishes it from classical controllers. This design approach has already shown that it can be easily scaled or synchronized. More than its performances, what is impressive is that the controller achieved those performances without excessive tuning. This shows the stability of the controller with respect to the perturbation of the different parameters.

The use of CPG in control is an emerging field, and much research is being conducted around the world. Works of Suzuki et al. [35], Saputra et al. [27], Dzeladini et al. [9], Akkawutvanich et al. [1] have investigated the use of CPGs to create controllers for biped locomotion. Luo et al. [22] showed that using a CPG controller, they managed to improve the ability of a quadruped robot to withstand impact from the side. Others have designed animal-like robots that use CPG for motor

control. Wu and Ma [37] have managed to design a robotic snake while Xie et al. [38], Jiayong Chen [18] have both focused on designing fishes that are able to swim.

However, the work done here has only opened the door to neuromorphic control, and many questions are waiting to be answered.

The performance of the controller was discussed only compared with itself and some natural control criteria. It would be natural to compare this controller with more classical approaches such as a PID. This would help set both control schemes apart and identify their weaknesses and strengths. In essence, this analysis would show the usefulness of this controller over existing controllers.

Another interesting addition to this work would be to extend the interconnection of multiple pendulum controllers to generate other more complicated gait or spatiotemporal patterns. Another step would be to try to switch dynamically between them smoothly to avoid unnatural and abrupt transitions. This would show that the model can be used in the real world in situations that require multiple modes of control.

In addition, the controller proposed here relies heavily on strong sensory feedback. An interesting challenge would be to use weak feedback but try to use neuromodulation to adapt the natural frequency of the half-center oscillator to match the frequency of the pendulum. Keeping the already existing neuromodulation for amplitude control in this system would make this feat more challenging.

Effective and energy-efficient control schemes are in demand to reduce consumption without compromising quality. The field of neuromorphic engineering aims to provide these benefits by taking inspiration from the most efficient data processing devices known, biological systems. This study takes a step toward fully neuromorphic design by using a completely analog controller that receives direct sensory feedback and can generate direct motor actions.

Bibliography

- [1] C. Akkawutvanich, F. I. Knudsen, A. F. Riis, J. C. Larsen, and P. Manoonpong. Adaptive parallel reflex- and decoupled cpg-based control for complex bipedal locomotion. *Robotics and Autonomous Systems*, 134:103663, 2020.
- [2] H. I. Ali, A. F. Hasan, and H. M. Jassim. Optimal h2pid controller design for human swing leg system using cultural algorithm. *Journal of Engineering Science and Technology*, 15(4):2270–2288, 2020.
- [3] U. Bässler and A. Büschges. Pattern generation for stick insect walking movements—multisensory control of a locomotor program. *Brain research reviews*, 27(1):65–88, 1998.
- [4] A. Cangelosi, J. Bongard, M. H. Fischer, and S. Nolfi. Embodied intelligence. In J. Kacprzyk and W. Pedrycz, editors, *Springer Handbook of Computational Intelligence*, pages 697–714. Springer Berlin Heidelberg, Berlin, Heidelberg, 2015.
- [5] H. Cheng, J. Xiao, Y. Long, and T. Zhang. Wind pendulum modeling based-on improved pid algorithm. In *2016 IEEE 11th Conference on Industrial Electronics and Applications (ICIEA)*, pages 2288–2293, 2016.
- [6] C. C. Chung and J. Hauser. Nonlinear control of a swinging pendulum. *Automatica*, 31(6):851–862, 1995. ISSN 0005-1098.
- [7] M. De Couck. Neuron. In M. D. Gellman and J. R. Turner, editors, *Encyclopedia of Behavioral Medicine*, pages 1325–1326. Springer New York, New York, NY, 2013.
- [8] G. Drion, A. Franci, and R. Sepulchre. Cellular switches orchestrate rhythmic circuits. *Biological Cybernetics*, 113, 04 2019.
- [9] F. Dzeladini, J. Van Den Kieboom, and A. Ijspeert. The contribution of a central pattern generator in a reflex-based neuromuscular model. *Frontiers in human neuroscience*, 8:371, 2014.
- [10] A. Franci, G. Drion, and R. Sepulchre. Robust and tunable bursting requires slow positive feedback. *Journal of Neurophysiology*, 119(3):1222–1234, 2018.
- [11] S. Grillner. Biological pattern generation: The cellular and computational logic of networks in motion. *Neuron*, 52(5):751–766, 2006.

- [12] P. Guertin. Central pattern generator for locomotion: Anatomical, physiological, and pathophysiological considerations. *Frontiers in Neurology*, 3, 2013.
- [13] P. A. Guertin. The mammalian central pattern generator for locomotion. *Brain Research Reviews*, 62(1):45–56, 2009.
- [14] A. Hodgkin, A. Huxley, and B. Katz. Ionic currents underlying activity in the giant axon of the squid. *Arch. Sci. Physiol.*, 3:129–150, 1949.
- [15] A. L. Hodgkin and A. F. Huxley. A quantitative description of membrane current and its application to conduction and excitation in nerve. *The Journal of physiology*, 117(4):500, 1952.
- [16] A. J. Ijspeert. Central pattern generators for locomotion control in animals and robots: A review. *Neural Networks*, 21(4):642–653, 2008.
- [17] A. Isidori and C. Byrnes. Output regulation of nonlinear systems. *IEEE Transactions on Automatic Control*, 35(2):131–140, 1990. doi: 10.1109/9.45168.
- [18] C. W. F. X. R. D. Y. Z. Jiayong Chen, Bo Yin. Bioinspired closed-loop cpg-based control of a robot fish for obstacle avoidance and direction tracking. *Journal of Bionic Engineering*, 18(1):171, 2021.
- [19] Z. Li, C. Zhu, Y.-L. Gao, Z.-K. Wang, and J. Wang. Alphago policy network: A dcnn accelerator on fpga. *IEEE Access*, 8:203039–203047, 2020.
- [20] H. Lodish, A. Berk, P. Matsudaira, C. A. Kaiser, M. Krieger, M. P. Scott, L. Zipursky, and J. Darnell. *Molecular Cell Biology*. WH Freeman and Company and Sumanas, Media Connected, 4th edition, 1999.
- [21] Q. Lu, X. Wang, and J. Tian. A new biological central pattern generator model and its relationship with the motor units. *Cognitive Neurodynamics*, 16 (1):135–147, 2022.
- [22] Q.-S. Luo, C. Zhou, Y. Jia, J. Gao, and F.-Z. Liu. Cpg-based control scheme for quadruped robot to withstand the lateral impact. *Beijing Ligong Daxue Xuebao/Transaction of Beijing Institute of Technology*, 35:384–390, 04 2015.
- [23] E. Marder. Neuromodulation of neuronal circuits: Back to the future. *Neuron*, 76(1):1–11, 2012.
- [24] E. Marder and D. Bucher. Central pattern generators and the control of rhythmic movements. *Current Biology*, 11(23):R986–R996, 2001.
- [25] E. Miranda and J. Suñé. Memristors for neuromorphic circuits and artificial intelligence applications. *Materials*, 13(4), 2020.
- [26] C. P. Santos, N. Alves, and J. C. Moreno. Biped locomotion control through a biomimetic cpg-based controller. *Journal of Intelligent & Robotic Systems*, 85: 47–70, 2017.

- [27] A. A. Saputra, J. Botzheim, A. J. Ijspeert, and N. Kubota. Combining reflexes and external sensory information in a neuromusculoskeletal model to control a quadruped robot. *IEEE Transactions on Cybernetics*, 52(8):7981–7994, 2022.
- [28] A. C. Schneider and C. Smarandache-Wellmann. Unmasking hidden changes in intrinsic properties in neurons that coordinate oscillatory networks. *bioRxiv*, 2022.
- [29] R. Sepulchre, G. Drion, and A. Franci. Excitable behaviors. In R. Tempo, S. Yurkovich, and P. Misra, editors, *Emerging Applications of Control and Systems Theory: A Festschrift in Honor of Mathukumalli Vidyasagar*, pages 269–280. Springer International Publishing, Cham, 2018.
- [30] A. A. Sharp, F. K. Skinner, and E. Marder. Mechanisms of oscillation in dynamic clamp constructed two-cell half-center circuits. *Journal of Neurophysiology*, 76(2):867–883, 1996.
- [31] D. Silver, A. Huang, C. J. Maddison, A. Guez, L. Sifre, G. Van Den Driessche, J. Schrittwieser, I. Antonoglou, V. Panneershelvam, M. Lanctot, et al. Mastering the game of go with deep neural networks and tree search. *nature*, 529 (7587):484–489, 2016.
- [32] D. Silver, J. Schrittwieser, K. Simonyan, I. Antonoglou, A. Huang, A. Guez, T. Hubert, L. Baker, M. Lai, A. Bolton, et al. Mastering the game of go without human knowledge. *nature*, 550(7676):354–359, 2017.
- [33] D. Silver, T. Hubert, J. Schrittwieser, I. Antonoglou, M. Lai, A. Guez, M. Lanctot, L. Sifre, D. Kumaran, T. Graepel, T. Lillicrap, K. Simonyan, and D. Hassabis. A general reinforcement learning algorithm that masters chess, shogi, and go through self-play. *Science*, 362(6419):1140–1144, 2018.
- [34] V. A. Straub. Central pattern generator. In M. D. Binder, N. Hirokawa, and U. Windhorst, editors, *Encyclopedia of Neuroscience*, pages 650–654. Springer Berlin Heidelberg, Berlin, Heidelberg, 2009.
- [35] H. Suzuki, J. H. Lee, and S. Okamoto. Development of semi-passive biped walking robot embedded with cpg-based locomotion control. In *2017 14th International Conference on Ubiquitous Robots and Ambient Intelligence (URAI)*, pages 75–78. IEEE, 2017.
- [36] B. Vazifehkhah Ghaffari, M. Kouhnnavard, and S. Elbasiouny. Mixed-mode oscillations in pyramidal neurons under antiepileptic drug conditions. *PLoS One*, 12(6):e0178244, 2017.
- [37] X. Wu and S. Ma. Cpg-based control of serpentine locomotion of a snake-like robot. *Mechatronics*, 20(2):326–334, 2010. ISSN 0957-4158.

- [38] F. Xie, Y. Zhong, R. Du, and Z. Li. Central pattern generator (cpg) control of a biomimetic robot fish for multimodal swimming. *Journal of Bionic Engineering*, 16:222–234, 03 2019.
- [39] H. Yu, H. Gao, and Z. Deng. Enhancing adaptability with local reactive behaviors for hexapod walking robot via sensory feedback integrated central pattern generator. *Robotics and Autonomous Systems*, 124:103401, 2020.

Appendix A

Signal Analysis Algorithms

This appendix contains pseudocodes of the algorithms used to compute the different metrics used throughout this thesis. All of them are custom algorithms designed specifically for the thesis and implemented in Matlab.

The algorithms described directly show the analysis of the signal. However, for all of them, the beginning of the vectors is cut from a certain time value to avoid analyzing transient effects. This was not included in the algorithms because it is a preprocessing step and not part of the logic. The index of the vectors starts at 1.

A.1 Neuronal signal analysis

Algorithm 1 is used to extract information from a neuronal trace. It can handle and classify all major neuronal behaviors (silence, spiking and bursting) and even make some inner distinctions (hyperpolarized or depolarized silence and normal or plateau bursting). The algorithm works by first classifying the behavior and then extracting the desired information by leveraging some assumptions about the behavior. The main idea is to segment the signal into positive and negative components. By counting the total number of pieces, the algorithm can distinguish whether the neuron is silent or not. If it is not silent, it analyzes the distribution of the length of the negative pieces to determine whether the neuron is bursting or spiking. Finally, if it is bursting, it analyzes the positive pieces to determine whether the bursting is normal or has a plateau. Not all paths of execution define all possible return values. To avoid any problem, it is assumed that the return values are initialized to NaN before execution.

A.2 Oscillation analysis

Algorithm 2 is used to analyze the oscillation of the pendulum. It extracts the dominant frequency to characterize the oscillation frequency and the amplitude of the oscillation to quantify its quality. This is the simplest algorithm of the list.

Algorithm 1 Neuronal Signal Analysis

Require: Vectors t and V of length L

```

1: Compute all times when  $V$  goes from negative to positive and store in  $c_{\text{up}}$ 
2: Compute all times when  $V$  goes from positive to negative and store in  $c_{\text{down}}$ 
3: if length of  $c_{\text{up}}$  or  $c_{\text{down}} < 3$  then                                 $\triangleright$  Silent Neuron
4:   if mean of  $V < 0$  then
5:     Type  $\leftarrow$  "hyperpolarized"
6:   else
7:     Type  $\leftarrow$  "depolarized"
8:   end if
9: else
10:   Compute lengths of positive periods from  $c_{\text{up}}$  and  $c_{\text{down}}$  and store in  $\lambda_+$ 
11:   Compute lengths of negative periods from  $c_{\text{up}}$  and  $c_{\text{down}}$  and store in  $\lambda_-$ 
12:   Cluster  $\lambda_+$  in two groups and compute their mean value in  $\mu_{+\downarrow}$  and  $\mu_{+\uparrow}$ 
13:   Cluster  $\lambda_-$  in two groups and compute their mean value in  $\mu_{-\downarrow}$  and  $\mu_{-\uparrow}$ 
14:   if  $\mu_{-\uparrow} > 4\mu_{-\downarrow}$  then                                          $\triangleright$  Bursting
15:     Compute indexes of the elements of  $\lambda_-$  in the  $\uparrow$  cluster and store in  $b_{\text{gap}}$ 
16:     Remove partial burst from start and end of  $V$ 
17:     if  $\mu_{+\uparrow} > 4\mu_{+\downarrow}$  then                                      $\triangleright$  Plateau Bursting
18:       Type  $\leftarrow$  "plateau"
19:        $p_{\text{len}} \leftarrow \mu_{+\uparrow}$ 
20:     else
21:       Type  $\leftarrow$  "bursting"
22:     end if
23:     Remove first element of  $\lambda_+$  if length of  $\lambda_+$  is higher than length of  $\lambda_-$ 
24:      $i_0 \leftarrow b_{\text{gap}}[1] + 1$             $\triangleright$  Get index of the start of the first full burst
25:      $i_{\text{max}} \leftarrow \min(\text{len}(\lambda_-), (\lambda_+))$ 
26:     Create vectors  $b_{\text{cycle}}$ ,  $b_{\text{size}}$ ,  $b_{\text{duty}}$ , spikes and  $s_{\text{cycle}}$ 
27:      $n \leftarrow 0$ 
28:      $c_t \leftarrow 0$ 
29:     tmp  $\leftarrow \lambda_+[i_0 - 1]$ 
30:     for all  $i \in \{i_0, \dots, i_{\text{max}}\}$  do
31:        $n \leftarrow n + 1$ 
32:       if  $i \in b_{\text{gap}}$  then
33:          $b_{\text{cycle}} \leftarrow b_{\text{cycle}} ++ [c_t + \text{tmp} + \lambda_-[i]] \$$ 
34:          $b_{\text{size}} \leftarrow b_{\text{size}} ++ [c_t + \text{tmp}]$ 
35:          $b_{\text{duty}} \leftarrow b_{\text{duty}} ++ [(c_t + \text{tmp}) / (c_t + \text{tmp} + \lambda_-[i])]$ 
36:         spikes  $\leftarrow \text{spikes} ++ [n]$ 
37:          $s_{\text{cycle}} \leftarrow s_{\text{cycle}} ++ [c_t / (n - 1)]$ 
38:          $n \leftarrow 0$ 
39:          $c_t \leftarrow 0$ 
40:         tmp  $\leftarrow \lambda_+[i]$ 
41:       else
42:          $c_t \leftarrow \lambda_-[i] + \lambda_+[i]$ 
43:       end if

```

Algorithm 1 Neuronal Signal Analysis (cont.)

```
44:   end for
45:    $f_{\text{inter}} \leftarrow$  inverse of mean of  $b_{\text{cycle}}$ 
46:    $b_{\text{len}} \leftarrow$  mean of  $b_{\text{size}}$ 
47:    $D \leftarrow$  mean of  $b_{\text{duty}}$ 
48:    $n_{\text{spikes}} \leftarrow$  mean of spikes
49:    $f_{\text{intra}} \leftarrow$  inverse of mean of  $s_{\text{cycle}}$ 
50: else                                 $\triangleright$  Spiking
51:   Type  $\leftarrow$  "spiking"
52:   Remove first element of  $\lambda_-$  if length of  $\lambda_-$  is higher than length of  $\lambda_+$ 
53:   Remove partial spike from start and end of  $V$ 
54:    $i_{\text{max}} \leftarrow \min(\text{len}(\lambda_-), (\lambda_+))$ 
55:    $\lambda_{\text{tot}} \leftarrow \lambda_- [1 : i_{\text{max}}] + \lambda_+ [1 : i_{\text{max}}]$ 
56:    $f_{\text{intra}} \leftarrow$  inverse of mean of  $\lambda_{\text{tot}}$ 
57:    $D \leftarrow$  mean of  $\lambda_+ / \lambda_{\text{tot}}$ 
58: end if
59: end if
60:  $V \leftarrow \min(V, 0)$ 
61:  $P \leftarrow$  mean of  $V$ 
62: return Type,  $P$ ,  $n_{\text{spikes}}$ ,  $D$ ,  $f_{\text{intra}}$ ,  $f_{\text{inter}}$ ,  $b_{\text{len}}$ ,  $p_{\text{len}}$ 
```

Algorithm 2 Oscillation Analysis

Require: Vectors t and θ of length L

- 1: Compute FFT of θ and store in f_{vec}
 - 2: Find the frequency of the maximum value of f_{vec} and store in f
 - 3: $R \leftarrow \max(\theta) - \min(\theta)$ \triangleright Range of oscillation
 - 4: **return** f , R
-

A.3 Modulation analysis

For this part the algorithm should start after a period of stabilization with a different θ_{ref} to guarantee good results. Algorithm 3 is used to analyze the modulation of g_{s-} . It computes three values, the time when the modulation stabilizes or the rise time, and the mean and standard deviation of the amplitude of the oscillations after stabilization. The three values indicate that there are two possibilities for stabilization. Either the modulation stops and the system falls into a constant amplitude or the modulation never stops and the system oscillates constantly around the desired amplitude. The algorithm handles both cases. Finally, there exists another less important possibility, the final time of the simulation is too small and the system has not yet reached the steady state. This should be seen as a degenerate case, and its treatment is not important.

Algorithm 3 Modulation Analysis

Require: Vectors t , θ , $\dot{\theta}$, v_d and v_u of length L

- 1: Compute when v_d last changes sign and store it in t_d
- 2: Compute when v_u last changes sign and store it in t_u
- 3: $t_n \leftarrow \max(t_d, t_u)$ \triangleright Contains the time of the last change in the g_{s-} parameter
- 4: **for all** $i \in \{2, \dots, L\}$ **do** \triangleright Compute value and time of the peaks in amplitude
- 5: **if** $\text{sign}(\dot{\theta}[i-1]) \neq \text{sign}(\dot{\theta}[i])$ **then**
- 6: Compute t_{int} , the linear approximation of the time where $\dot{\theta} = 0$
- 7: Compute θ_{int} , the linear approximation of the value of θ at t_{int}
- 8: Append t_{int} to t_{vec}
- 9: Append $|\theta_{\text{int}}|$ to θ_{vec}
- 10: **end if**
- 11: **end for**
- 12: Compute when θ_{int} first crosses the desired amplitude and store it in t_{amp}
- 13: **if** $t_{\text{amp}} < t_n$ **then** \triangleright Amplitude is oscillating
- 14: $t_{\text{rise}} \leftarrow t_{\text{amp}}$
- 15: $\mu_A \leftarrow \text{mean of } \theta_{\text{vec}} \text{ where } t_{\text{vec}} \geq t_{\text{amp}}$
- 16: $\sigma_A \leftarrow \text{SD of } \theta_{\text{vec}} \text{ where } t_{\text{vec}} \geq t_{\text{amp}}$
- 17: **else** \triangleright Amplitude is stable
- 18: $t_{\text{rise}} \leftarrow t_n$
- 19: $\mu_A \leftarrow \text{mean of } \theta_{\text{vec}} \text{ where } t_{\text{vec}} \geq t_n$
- 20: $\sigma_A \leftarrow 0$
- 21: **end if**
- 22: **return** $t_{\text{rise}}, \mu_A, \sigma_A$
